FLT PET IMAGING IN COLORECTAL CANCER

By

Eliot Thomas McKinley

Dissertation

Submitted to the Faculty of the

Graduate School of Vanderbilt University

In partial fulfillment of the requirements

For the degree of

DOCTOR OF PHILOSOPHY

In

Biomedical Engineering

May, 2013

Nashville, TN

Approved:

H. Charles Manning, Ph.D.

Robert J. Coffey, M.D.

John C. Gore, Ph.D.

Melissa C. Skala, Ph.D.

M. Kay Washington, M.D., Ph.D.

I've been dropping the new science and kicking the new knowledge

- The Beastie Boys, “Sounds of Science”

ACKNOWLEDGMENTS

Without the help and support of a number of people the work presented here would not have been possible. Firstly, my advisor, Charles Manning, for sharing his wealth of knowledge with me and always being there to help with any problem that would arise. My fellow members of the Manning lab and VUIIS have been invaluable to the completion of this dissertation, including but not limited to Nathan Mutic, Saffet Guleryuz, Ping Zhao, Allie Fu, Matt Hight, Dewei Tang, Jason Buck, Adam Smith, YY Cheung, Samir Saleh, Imam Uddin, JP Xie, Noor Tantawy, Clare Osborne, George Wilson, and Nancy Hagans. Additionally I would like to thank the co-authors of the manuscripts that largely make up this dissertation, including many of the above, as well as Dan Ayers, Frank Revetta, Bob Coffey, Kay Washington, and Ron Walker.

Without the support of teachers, family, and friends I would have never have made it to grad school, let alone finally finished. In 4th grade my teacher Mark Bach and class scientist Phil Sticksel taught me that science is cool and influenced my decision to become a scientist. In high school I was lucky to have great science and math teachers including Mike Arends, Penny Bostic, Sarah Vandermeer, and Brady Brady. In undergrad, David Wilson gave me a chance to do research before I knew what I was doing. I'd like to thank all my fellow grad students for commiserating and seeing them graduate always gave me hope. I'd specifically like to thank Dean Paras for teaching me the best way to eat a Chipotle burrito and being so generous with his Christmas Ale, everyone misses

you and I'll always remember you. To my parents, Tom and Jill, thanks for always being there for me and providing pretty much an ideal childhood. To Huong, who would of thought that 9 years ago that when I damned you for seeing Beulah's final show we would still be together. Thank you for rescuing my best buddy Geoffrey, from the Barboursville Toys R Us Parking lot, and then bringing Boo Bear, Kiwi and Peanut into my life. Even though I will now (presumably) have a doctorate to match yours, you are and will forever be oftentimes right.

TABLE OF CONTENTS

Page

LIST OF TABLES

Table Page

LIST OF FIGURES

Figure Page

CHAPTER 1

INTRODUCTION

Current imaging criteria for evaluating therapeutic response are based upon anatomical information according to Response Evaluation Criteria in Solid Tumors (RECIST) guidelines (1). These criteria, which are solely based on a reduction in tumor size, do not take advantage of cellular and molecular information now available through contemporary imaging methodology. Importantly, since relevant cellular and molecular changes may precede changes in size and may occur within hours of initial treatment, RECIST criteria and conventional imaging methods are frequently inadequate for assessing early tumor response. These limitations, coupled with the increasing clinical relevance of employing complex, molecularly targeted therapeutic regimens to treat cancer, highlight a critical need to accelerate the translation of novel imaging approaches that are capable of reporting cellular and molecular responses of tumor cells to therapy. Presently, a major impediment to the clinical translation of novel imaging methodology is a lack of understanding of how targeted therapy can affect uptake of molecular probes and a lack appropriate validation studies conducted within relevant biological contexts.

This dissertation seeks to elucidate molecular determinants that affect 3'-deoxy-3'[^{18}F]-fluorothymidine ([^{18}F]-FLT) PET imaging as a biomarker of response to targeted therapeutics in colorectal cancer (CRC). Numerous

targeted therapeutics are designed to reduce tumor cell proliferation, and imaging methods capable of directly measuring proliferation hold great promise as predictive clinical biomarkers. The widely used PET tracer 2-deoxy-2-[^{18}F] fluoro-D-glucose ([^{18}F]-FDG) is an important tool for cancer diagnosis and staging, yet tissue uptake broadly reflects a host of metabolic processes, highlighting an unmet clinical need for imaging methods that more directly measure proliferation. As an alternative, the PET tracer [^{18}F]-FLT, has shown promise as a biomarker of proliferation in oncology. However, a key impediment to broad clinical acceptance of [^{18}F]-FLT PET continues to be a lack of appropriate validation studies conducted within biologically focused and clinically relevant contexts. Additionally, it remains poorly understood how the molecular events that underlie cancer – e.g., activation of oncogenes and loss of tumor suppressor genes - affect [^{18}F]-FLT uptake in tumors.

CHAPTER 2

BACKGROUND

2.1 Overview of Molecular Imaging Modalities

Since the discovery of X-Rays by Wilhelm Conrad Röntgen in 1895 (2), medical imaging has become a powerful clinical tool in the diagnosis and treatment of disease. Planar X-Ray, Computed Tomography (CT), Magnetic Resonance Imaging (MRI), and ultrasound imaging have become ubiquitous in the clinical setting. However, these modalities have, until recently, been limited anatomical studies, *i.e.* imaging of structure rather than biological function. Molecular imaging, “the visualization, characterization and measurement of biological processes at the molecular and cellular levels in humans and other living systems” (3) has recently emerged as a clinical and research tool to interrogate functional biological processes. Molecular imaging can be utilized in the detection, diagnosis and prognosis of disease, as well as to aid in the determination of treatment response.

The most important component of molecular imaging is the molecular imaging agent itself, which is composed of two basic parts, the targeting moiety and the signaling moiety (4). The targeting moiety directs the probe to the biological target of interest. A number of types of targeting moieties are currently in use including antibodies, proteins, peptides, and small molecules. The signaling moiety provides a means for detection of the molecular imaging probe

by an imaging system. Signaling moieties include radionuclides, fluorophores, hyperpolarized molecules, nanoparticles, microbubbles and even endogenous substances.

The ability to label a targeting moiety with many types of signaling moieties allows molecular imaging to occur across a number of imaging modalities (5). The most common clinical molecular imaging modalities are Positron Emission Tomography (PET) and Single Photon Emitted Computer Tomography (SPECT), which utilize radionuclides as signaling moieties. PET imaging with positron emitting radionuclides such as ^{11}C, ^{18}F, ^{64}Cu, and ^{68}Ga allows imaging resolutions on the order of millimeters with very high sensitivity in both clinical and preclinical settings. SPECT imaging utilizes radionuclides that exhibit a single photon decay including ^{99m}Tc, ^{123}I, ^{111}In, and ^{177}Lu. SPECT has somewhat lower sensitivity compared to PET and has lower resolution in the clinical setting, but can have higher resolution in pre-clinical imaging due to specialized hardware for small animal imaging. Fluorescence imaging with fluorescent dyes, proteins, or quantum dots can have both high sensitivity and resolution when used superficially. However, it can quickly lose both when tissue is present between the fluorophore and the detector due to scattering and absorbance of the incident and fluorescent photons, as well as the presence of autofluorescence in the tissue. In practice, fluorescence imaging is mainly limited to pre-clinical imaging due to depth of detection issues. However fluorescence can be effectively utilized in superficial or topical applications in humans such as during colonoscopy. Bioluminescent imaging (BLI), a purely preclinical imaging

Modality	Signal	Clinical	Sensitivity*	Resolution Clinical; Pre-Clinical
PET	^{11}C, ^{18}F, ^{64}Cu, ^{68}Ga	Yes	1	~4 mm; ~2 mm
SPECT	^{99m}Tc, ^{123}I, ^{111}In, ^{177}Lu	Yes	10^{-1}-10^{-2}	6-8 mm; 1-2 mm
Fluorescence	Fluorescent proteins, fluorochromes, quantum dots	Potential	10^{-2}-1†	N/A; 1-3 mm
BLI	Light	No	1-10^{2} †	N/A; 1-10 mm
MRI	Gadolinium, SPIO, USPIO, ^{19}F	Potential	10^{-5}	1 mm; 80-100 μm
MRS	Endogenous compounds, hyperpolarized ^{13}C	Yes	< 10^{-5}	~1mm; < 1mm
Ultrasound	Microbubbles	Potential	> 10^{-5}	300-500 μm; 50 μm
* Relative to PET, † Depth-dependent, N/A Not Applicable Adapted from (4, 5)				

Table 2.1. Overview of molecular imaging modalities.

modality, utilizes reporter genes typically expressing luciferase, which cleaves injected luciferin leading to the release of light. BLI can have very high sensitivity due to the lack of naturally occurring light sources, but has roughly millimeter resolution due to scattering and absorbance of light while traveling though tissue. MRI, while typically used for anatomical imaging, may be used as a molecular imaging modality. Signaling moieties containing metals that effect either the T_1 or T_2 relaxation times of hydrogen such as Gadolinium or superparamagnetic iron oxide particles, or imaging ^{19}F rather than hydrogen have been developed. However, each exhibit very low sensitivity compared to PET. Additionally, Magnetic Resonance Spectroscopy (MRS) may be utilized to assay naturally

occurring molecules or to detect exogenous molecules that induce chemical shift, however, MRS is very low sensitivity with low resolution compared to MRI. Finally, ultrasound imaging can be used as a molecular imaging modality by the use of targeted microbubbles. Tiny gas-containing bubbles on the order of microns in diameter are injected into the blood stream and can hone to various intravascular targets. Real time imaging ability makes ultrasound attractive for molecular imaging. However, as well as relatively high resolution in pre-clinical settings, however the sensitivity is low compared to PET, limited to intravascular targets, and has not been extensively studied as a molecular imaging modality in a clinical setting. A comparison of the performance and characteristics of these imaging modalities can be found in **Table 2.1**. Due to the unique properties of PET imaging, it has become the main molecular imaging modality utilized in translational research.

2.2 Basics of PET imaging

PET has become a powerful clinical and research tool in oncology, neurosciences, cardiology, and pharmacology in both small animals and humans. PET detects paired gamma rays that are produced following the annihilation of the positron emitted from a positron emitting nuclide interacting with an electron (6). Two 511 keV γ-rays are emitted at almost 180º and are detected by a ring of scintillators (**Fig. 2.1**). Detection of two scintillation events within a short time window on opposite sides of the detector ring defines a line of response within which the positron annihilation is assumed to have taken place. Based upon the

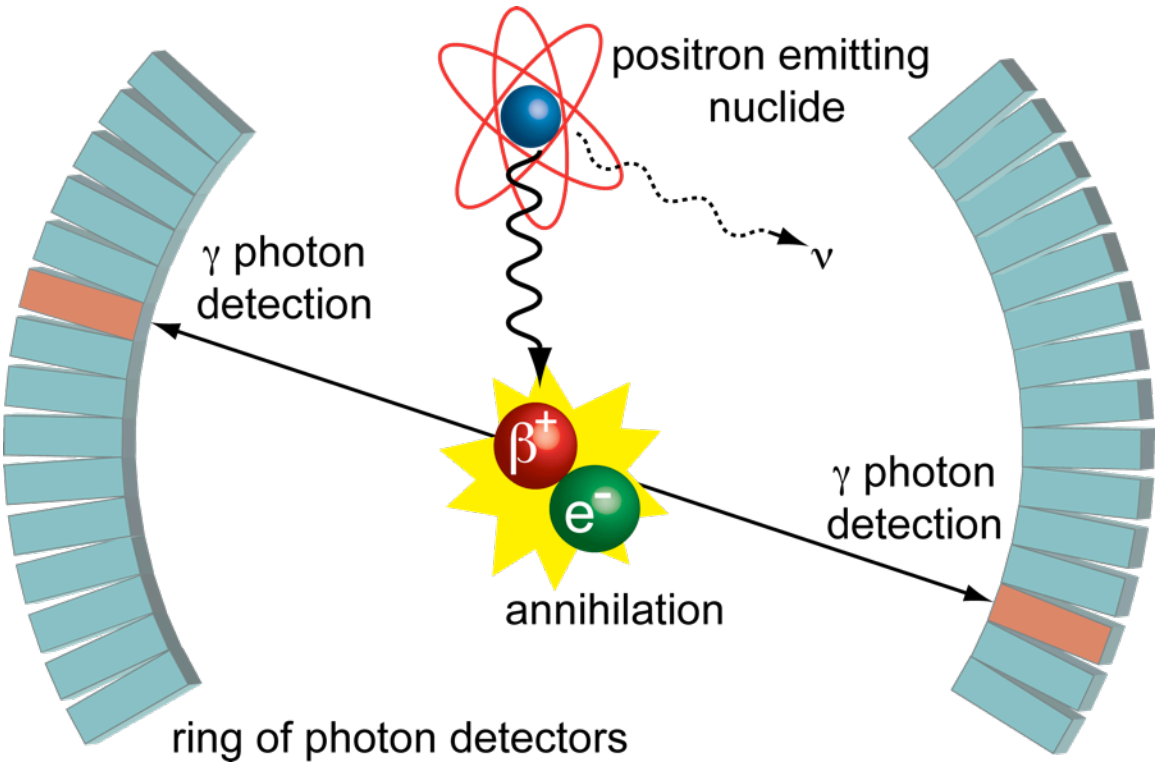

Fig. 2.1. Basis of PET imaging. A positron emitting isotope (e.g. ^{18}F, ^{11}C, ^{64}Cu) decays and emits a positron and a neutrino (ν). After traveling a short distance, the emitted positron interacts with an electron and both particles are annihilated releasing two-511 keV photons. The two γ-rays travel in opposite directions and are detected by a ring of photon detectors.

detection of millions of annihilation events, an image of the radiotracer distribution can be reconstructed via a number of algorithms.

Compared to many other in vivo imaging modalities, PET has the distinct advantage of being inherently quantitative. After calibration, the radioactivity in each voxel can be determined using a number of well-established methods. While inspection of PET images can be used for simple detection of tumors, especially clinically, it is difficult to make comparisons across subjects due to differences in windowing of the images, injected dose, and various physiological factors. Study design for PET generally breaks down in to two categories, static methods and kinetic methods. In static PET imaging, the radiotracer is injected

into the patient or animal, allowed to circulate, and imaged after the tracer has reached steady state in the tissue of interest. Typically, quantification is normalized to the injected activity and the weight of the patient, and is expressed as either percent injected dose per gram (%ID/g) or as standardized uptake value (SUV). In dynamic imaging, the radiotracer is infused into the subject while in the scanner and the uptake of the tracer can be followed until it reaches a steady state level. Time-activity curves are then generated for each tissue of interest and applied either to compartment modeling or graphical analysis to determine a wide array of biologically relevant parameters. Typically, due to longer imaging times and the need to collect blood samples, dynamic imaging is typically utilized only in research studies requiring absolute quantification.

2.3 [^{18}F]-FLT PET

Suitable methodologies for imaging proliferation have been studied by a number of groups. PET tracers that are precursors for DNA synthesis have been explored and include [^{11}C] and [^{18}F] labeled nucleosides and structural analogues (7-10). Among the most promising has been [^{18}F]-FLT. First described for use as a molecular imaging agent in 1998 by Shields, et al. [^{18}F]-FLT has been extensively studied in the pre-clinical setting and is rapidly being translated to clinical use, however, many aspects of [^{18}F]-FLT PET are still not well understood (11-14). Theoretically, [^{18}F]-FLT serves as a surrogate of proliferation by reporting the activity of thymidine salvage, a mechanism that serves to provide dividing cells with DNA precursors (deoxyribonucleosides) from the extracellular

environment. Like other nucleosides, [^{18}F]-FLT is thought to be transported across the cell membrane by facilitated diffusion via low-affinity, non-concentrative nucleoside carrier proteins. Upon internalization, [^{18}F]-FLT is monophosphorylated in a reaction catalyzed by the cytosolic enzyme thymidine kinase 1 (TK1). Unlike thymidine, [^{18}F]-FLT is not incorporated into DNA, yet phosphorylation to [^{18}F]-FLT monophosphate results in intracellular trapping and accumulation. TK1 activity is regulated at transcriptional, translational, and post-translational levels and activity tends to be closely correlated with DNA synthesis (late G1-S phase of cell cycle) (15). TK1 activity is diminished in quiescent, non-proliferating cells. Many preclinical and clinical studies have been published since the late 1990's exploring the utility of [^{18}F]-FLT PET imaging as a metric to assess proliferation in various species, tumor types, and organ sites (14, 16-21). From objective review of this large body of work, which includes both positive and negative results, it is clear that additional validation studies must be conducted at the basic science and early clinical level before [^{18}F]-FLT can be embraced as a universal biomarker of cellular proliferation in cancer.

Currently, the relationship between [^{18}F]-FLT uptake, TK1 biology, and cellular proliferation is not widely understood in oncology. Varying degrees of correlation between [^{18}F]-FLT uptake and histological markers of proliferation such as Ki67 labeling indices have been reported. Differences in TK1 regulation across tumor types likely contributes to much of the variability observed in [^{18}F]-FLT PET imaging in cancer. Studies have been carried out in normal cells in an effort to understand cellular regulation of TK1 expression and biological factors

that affect TK1 activity. However, much of this research has not yet translated directly into a broad understanding of [^{18}F]-FLT uptake in tumors. At the genetic level, TK1 has been thoroughly characterized in normal cells; the gene is located on chromosome 17 and was cloned in 1983 (22). Despite the observation that TK1 activity tends to be cell cycle-regulated and correlated with S-phase in normal cells, overexpression of thymidine kinase mRNA (23), as well as defective p53 response (24), can lead to loss of cell cycle control of TK1 expression. Both of these conditions, and additional defects in cell cycle regulatory molecules that can affect TK1 expression, are common in tumor cells. Typically, TK1 expression is negatively regulated via a p53/p21-dependent mechanism. Cyclin D, cyclin E, and p21 regulate the tumor suppressor retinoblastoma gene product (*Rb*), which when hyperphosphorylated (*ppRb*), releases E2F transcription factors to activate other downstream genes including TK1 (**Fig. 2.2**). Defects in any of these cell cycle regulatory molecules are common in tumors and lead to altered *Rb* activation and thus dysregulated E2F-dependent TK1 transcriptional activity. Molecularly targeted therapies that may affect these regulatory molecules may also in turn affect TK1 expression in unexpected ways. It is important to emphasize that careful elucidation of molecular determinants affecting TK1 regulation in cancer cells is urgently needed. Our preliminary data suggests that a number of important oncogenes and tumor suppressor genes are capable of regulating TK1 at transcriptional and translational levels, dictating the ability of [^{18}F]-FLT PET to report clinically relevant changes in proliferation and treatment response.

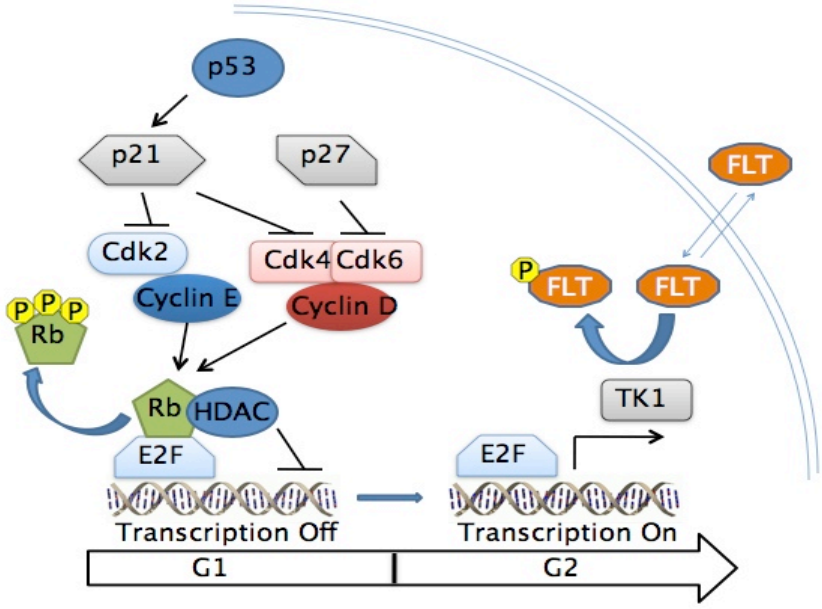

Fig. 2.2. Regulation of TK1. TK1 synthesis is regulated by p53 and p21 though E2F. Phosphorylation of Rb releases E2F which induces TK1 gene expression.

A central premise behind the use of [^{18}F]-FLT uptake as a surrogate of proliferation is that dividing cells utilize thymidine salvage to capture nucleoside precursors for DNA synthesis. While this premise holds true in many situations, thymidine salvage is not a prerequisite for cell survival in replicating mammalian cells, and in fact, is only a complementary route for providing cells with nucleosides. *De novo* synthesis of nucleosides is fully capable of providing all the DNA precursors that are needed for cell growth (15). Thus, [^{18}F]-FLT uptake in tumors relying predominately or completely on *de novo* nucleoside synthesis may poorly inform proliferative status compared with tumors that rely more heavily on thymidine salvage. Indeed, we have employed isogenically-matched human CRC cell line pairs with otherwise similar proliferation characteristics to illustrate that [^{18}F]-FLT uptake is reduced in tumors with greater tendency to utilize the *de novo* pathway (see chapter 4). The use of the *de novo* pathway also has ramifications

on histological validation of FLT PET imaging. Historically, Ki67 immunoreactivity has been the clinical gold-standard for validation of [^{18}F]-FLT PET imaging. This is unfortunate because there is an important disconnect between these two metrics. Nuclear Ki67 staining is positive for cells in any non-G0 phase of cell cycle and thus serves as a general marker of cell proliferation. In contrast, the closer association of [^{18}F]-FLT uptake with TK1 activity, which is primarily associated with S-phase, suggests that [^{18}F]-FLT PET provides more specific information than Ki67.

In 2008 we published our first [^{18}F]-FLT PET imaging in the context of predicting treatment response (25). Here we showed that in a *KRAS* wild-type human colorectal cancer DiFi xenografts treatment with cetuximab, a monoclonal antibody to EGFR, resulted in tumor regression, apoptosis, and evidence of EGFR occupancy by cetuximab. Conversely, in *KRAS* mutant human colorectal cancer HCT-116 xenografts no tumor regression, apoptosis, or evidence of EGFR occupancy was observed. [^{18}F]-FLT uptake was not decreased following treatment in either cell line xenograft model. Understanding the mechanisms that led to maintenance of TK1 levels, and thus [^{18}F]-FLT PET, in DiFi xenografts treated with an effective dose of cetuximab, despite reduced proliferation by other clinical means, was the impetus for the studies contained in this dissertation. Following the 2008 study, we subsequently studied the utility of [^{18}F]-FLT PET to predict treatment response in preclinical breast cancer treated with the HER2-targeted monoclonal antibody, trastuzumab (26), and in a clinical trial of patients with Ménétrier's disease, a pre-malignant hyperproliferative

disorder of the stomach (27). The results presented in this dissertation further elucidate the mechanistic basis of [^{18}F]-FLT in colorectal cancer and provide a basis for best practices when [^{18}F]-FLT PET is deployed in the clinical setting.

CHAPTER 3

SPECIFIC AIMS

1. To identify molecular determinants that affect [^{18}F]-FLT PET imaging in preclinical mouse models of human CRC.

We will employ preclinical CRC mouse models featuring tumors derived from established human CRC cell lines to evaluate [^{18}F]-FLT as a prognostic marker of proliferation (Aim 1A) and the effect of targeted therapy on [^{18}F]-FLT (Aim 1B). Models have been selected to recapitulate clinical features of human CRC, such as genetic mutations in *KRAS* and *BRAF*, and will be used to explore [^{18}F]-FLT PET imaging within therapeutic contexts that model ongoing clinical trials. Validation of [^{18}F]-FLT PET will be performed at genomic, proteomic, and cellular scales utilizing imaging-matched tumor tissues collected from treated and untreated cohorts.

2. To explore the utility of [^{18}F]-FLT PET to assess clinical and biological effects of inhibiting EGF receptor in neoadjuvant trials of patients with advanced CRC.

We will incorporate correlative pre- and post-treatment [^{18}F]-FLT PET imaging as part of a Phase II neoadjuvant trial presently enrolling at our institution. We will evaluate the effect of neoadjuvant blockade of EGFR in locally advanced rectal cancer on [^{18}F]-FLT PET. Analogous to Aim 1, validation of [^{18}F]-

FLT PET will be performed at proteomic and cellular scales utilizing imaging-matched tumor tissues collected pre-treatment, during the course of therapy, and following surgical resection.

The overarching goal of this study is an improved understanding of the biological basis of [^{18}F]-FLT PET imaging. We anticipate that results obtained here may also be applicable to other types of solid tumors.

CHAPTER 4

LIMITS OF [^{18}F]-FLT PET AS A BIOMARKER OF PROLIFERATION IN ONCOLOGY

1. Abstract

Background

Non-invasive imaging biomarkers of cellular proliferation hold great promise for quantifying response to personalized medicine in oncology. An emerging approach to assess tumor proliferation utilizes the positron emission tomography (PET) tracer 3'-deoxy-3'[^{18}F]-fluorothymidine, [^{18}F]-FLT. Though several studies have associated serial changes in [^{18}F]-FLT PET with elements of therapeutic response, the degree to which [^{18}F]-FLT PET quantitatively reflects proliferative index has been continuously debated for more that a decade. The goal of this study was to elucidate quantitative relationships between [^{18}F]-FLT PET and cellular metrics of proliferation in treatment naïve human cell line xenografts commonly employed in cancer research.

Methods and Findings

[^{18}F]-FLT PET was conducted in human cancer xenograft-bearing mice. Quantitative relationships between PET, thymidine kinase 1 (TK1) protein levels and immunostaining for proliferation markers (Ki67, TK1, PCNA) were evaluated using imaging-matched tumor specimens. Overall, we determined that [^{18}F]-FLT PET reflects TK1 protein levels, yet the cell cycle specificity of TK1 expression

and the extent to which tumors utilize thymidine salvage for DNA synthesis decouple [^{18}F]-FLT PET data from standard estimates of proliferative index.

Conclusions

Our findings illustrate that [^{18}F]-FLT PET reflects tumor proliferation as a function of thymidine salvage pathway utilization. Unlike more general proliferation markers, such as Ki67, [^{18}F]-FLT PET reflects proliferative indices to variable and potentially unreliable extents. [^{18}F]-FLT PET can not discriminate moderately proliferative, thymidine salvage-driven tumors from those of high proliferative index that rely primarily upon *de novo* thymidine synthesis. Accordingly, the magnitude of [^{18}F]-FLT uptake should not be considered a surrogate of proliferative index. These data rationalize the diversity of [^{18}F]-FLT PET correlative results previously reported and suggest future best-practices when [^{18}F]-FLT PET is employed in oncology.

2. Introduction

Non-invasive molecular imaging biomarkers of cellular proliferation hold great promise for characterizing tumors and predicting their response to personalized therapeutic regimens. To this end, positron emission tomography (PET) tracers based upon precursors for DNA synthesis have been explored and include 11-carbon ([^{11}C]) and 18-fluorine ([^{18}F]) labeled nucleosides and related structural analogues (7-10). The most promising and widely explored of these agents has been 3'-deoxy-3'[18F]-fluorothymidine ([^{18}F]-FLT) (14, 28-30). [^{18}F]-FLT PET, serves as a surrogate of proliferation by targeting the activity of

thymidine salvage, one of two distinct mechanisms that supply DNA precursors to dividing cells (**Fig. 4.1**).

In the salvage pathway, nucleosides including [^{18}F]-FLT are transported across the cell membrane by facilitated diffusion via low-affinity, non-concentrative nucleoside carrier proteins that are conserved across nearly all animal cells (15). Upon internalization, [^{18}F]-FLT is monophosphorylated in a

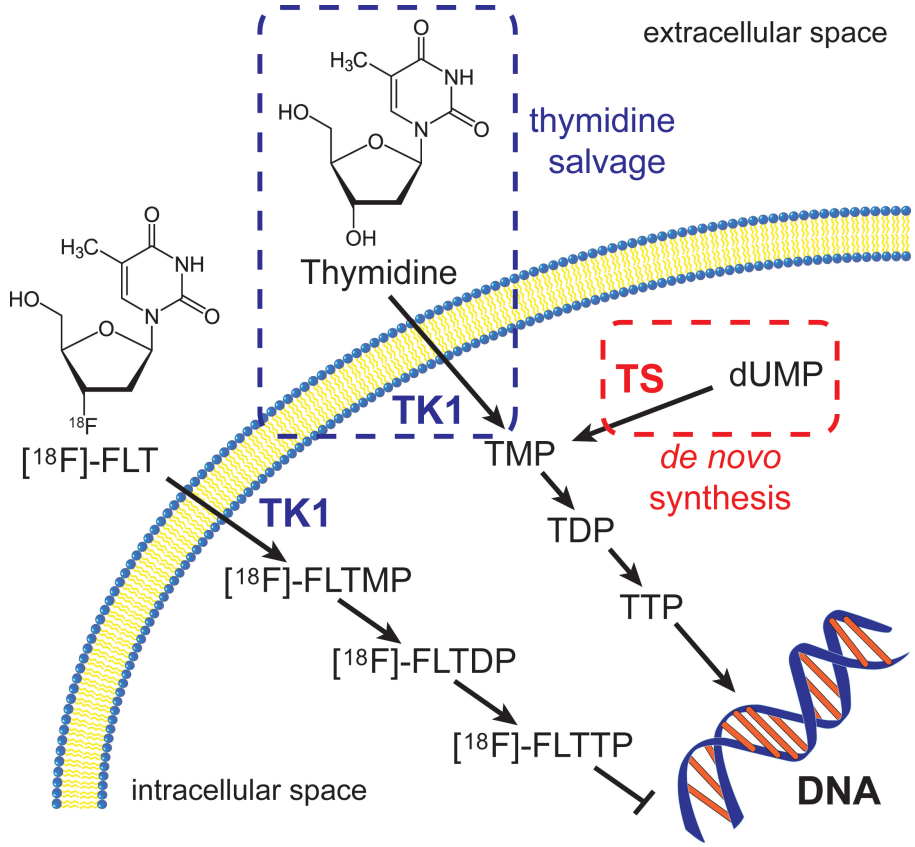

Fig. 4.1. Thymidine salvage and *de novo* synthesis pathways. In thymidine salvage, thymidine is transported across the cell membrane and phosphorylated by TK1 into thymidine monophosphate (TMP). The thymidine is further phosphorylated into thymidine diphosphate (TDP) and thymidine triphosphate (TTP) and then incorporated into DNA. Alternatively, using the *de novo* synthesis pathway, deoxyuridine monophosphate (dUMP) is converted to TMP by TS which can then be further phosphorylated and incorporated into DNA. Similarly to thymidine, [^{18}F]-FLT is transported into the cell and phosphorylated into [^{18}F]-FLT monophosphate ([^{18}F]-FLTMP) and trapped by TK1. [^{18}F]-FLTMP can be further phosphorylated into [^{18}F]-FLT diphosphate ([^{18}F]-FLTDP) and [^{18}F]-FLT triphosphate ([^{18}F]-FLTTP), however, due to the substitution of OH with ^{18}F in the 5-prime position, [^{18}F]-FLTTP is not incorporated into the DNA.

reaction catalyzed by the cytosolic enzyme thymidine kinase 1 (TK1). Unlike thymidine, which is further phosphorylated and subsequently incorporated into DNA, monophosphorylation of [^{18}F]-FLT results in intracellular trapping and accumulation without DNA incorporation. In many tissues, TK1 activity is regulated at transcriptional, translational, and post-translational levels (15) and activity is closely correlated with the DNA synthesis phase of proliferating cells (typically late G1-S). TK1 activity is diminished in quiescent, non-proliferating cells. Many preclinical and clinical studies have been published since the late 1990s which explored [^{18}F]-FLT PET imaging to assess proliferation in various species, tumor types, and organ sites. Among these, varying degrees of correlation between [^{18}F]-FLT uptake and histological markers of proliferation, such as Ki67 labeling indices (14, 16, 18-20, 31-33), have been observed. Accordingly, quantitative relationships between [^{18}F]-FLT uptake and cellular proliferation in tumors have remained poorly defined.

A key factor limiting [^{18}F]-FLT PET is *de novo* thymidine pathway utilization, although the extent of this limitation is not fully appreciated. The *de novo* pathway is complementary to thymidine salvage and is fully capable of providing all the thymidine needed for DNA synthesis (15). Through the action of the enzyme thymidylate synthase (TS), deoxyuridine monophosphate is converted to thymidine monophosphate, which is subsequently incorporated into DNA. It is widely assumed that [^{18}F]-FLT PET may underestimate proliferation in *de novo* pathway-dependent tumors, yet conclusive studies determining the extent of this discrepancy have not been reported.

In this study, we show that [^{18}F]-FLT PET directly measures TK1 levels and correlates with thymidine salvage pathway utilization. We further illustrate that [^{18}F]-FLT PET poorly reflects proliferative index in tumors that utilize the *de novo* pathway. Consequently, [^{18}F]-FLT PET only correlates with proliferative index as a function of salvage pathway utilization. These data explain, in part, the diversity of [^{18}F]-FLT PET correlative results previously reported and suggest future best-practices when [^{18}F]-FLT PET is employed in oncology.

3. Materials and Methods

Cell Lines and Mouse Models

All studies were approved by the Vanderbilt University Institutional Animal Care and Use Committee and all efforts were made to minimize animal suffering. Human colorectal cancer cell lines DiFi, HCT-116, HCT-116*p21*$^{-/-}$, HCT-116*p53*$^{-/-}$, SW620, HT-29, and Lim2405 and the human breast cancer cell line BT474 were grown in Dulbecco's modified Eagle's medium, DMEM, and Colo205 grown in RPMI (Cellgro, Manassas, VA) with 10% fetal bovine serum, (Atlanta Biologicals, Lawrenceville, GA), 1% penicillin and streptomycin (Life Technologies, Grand Island, NY) at 37°C and 5% CO_2. HCT-116, SW620, HT-29, and BT474 cells were obtained from ATCC. DiFi cells were a gift from from Dr. Bruce Boman (34), HCT-116*p21*$^{-/-}$ (35) and HCT-116*p53*$^{-/-}$ (36) cells were obtained from Dr. Bert Vogelstein's laboratory, and Lim2405 (37) cells were obtained from Dr. Robert Whitehead (Ludwig Institute for Cancer Research). Cell line xenografts were

generated in athymic nude mice (Harlan, Indianapolis, IN) as described (25) and imaged when volume reached approximately 250 mm^3.

[^{18}F]-FLT Radiosynthesis

[^{18}F]-FLT was prepared in a two-step, one-pot reaction as described (26, 29). [^{18}F]-FLT was obtained with average radiochemical purity of 98.3% and specific activity ≥ 345.5 TBq/mmol.

Small-Animal PET Imaging

Small-animal PET imaging was performed using a dedicated Concorde Microsystems Focus 220 microPET scanner (Siemens Preclinical Solutions, Knoxville, TN). Mice were maintained under 2% isoflurane anesthesia in 100% oxygen at 2 L/min and kept warm via a circulating water heating pad for the duration of the PET scan. Animals were administered 7.4-9.3 MBq (200-250 μCi) of [^{18}F]-FLT intravenously. For static scans, animals were allowed free access to food and water during a 40 minute uptake period, followed by anesthetization and a 20 minute image acquisition. Sixty minute dynamic acquisitions were initiated at the time of [^{18}F]-FLT injection. PET data were reconstructed using a three-dimensional (3D) ordered subset expectation maximization/maximum a posteriori (OSEM3D/MAP) algorithm. Dynamic data was binned into twelve 5 s (0-1 min) and fifty-nine 60 s (2-60 mins) frames. The resulting three-dimensional reconstructions had an x-y voxel size of 0.474 mm and inter-slice distance of 0.796 mm.

Image Analysis and Compartmental Modeling

ASIPro software (Siemens Preclinical Solutions) was used to manually draw three-dimensional regions of interest in the tumor volume and, for dynamic scans, the left ventricle. For static scans, [^{18}F]-FLT uptake was quantified as the percentage of the injected dose per gram of tissue (%ID/g) by dividing the ROI activity by the injected dose and multiplying by 100. For dynamic scans, a 3-compartment, 4-rate-constant model was used to characterize [^{18}F]-FLT pharmacokinetics as extensively described by Muzi et al (38). The compartmental model was implemented using the Matlab-based COMKAT (39) software package. Rate constants for [^{18}F]-FLT influx (K_1) and efflux (k_2) from the vascular compartment to the tissue compartment as well rate constants for [^{18}F]-FLT phosphorylation (k_3) and dephosphorylation (k_4) were determined from the model. The metabolic flux of [^{18}F]-FLT was calculated according to:

$$K_{FLT}=(K_1 \times k_3)/(k_2 + k_3). \quad [4.1]$$

Parametric maps illustrating K_1, K_{FLT}, and %ID/g were obtained through voxel-wise compartmental modeling using the PMOD 2.6 software package (PMOD Technologies, Zurich, Switzerland).

Immunohistochemistry (IHC)

Animals were sacrificed by cervical dislocation under isoflurane anesthesia and tumor samples were collected immediately following [^{18}F]-FLT PET, then subsequently fixed in 10% formalin for 24 h. Tissues were then

transferred to 70% ethanol prior to paraffin embedding. Tissues were sectioned (4 μm thickness) and stained for proliferation markers Ki67 (#M7240, Dako, Carpinteria, CA, 1:100 primary dilution), Proliferating Cell Nuclear Antigen (PCNA)(#V1006, Biomeda, Foster City, CA, 1:800 primary dilution), and TK1 (#57757, Abcam, Cambridge, MA, 1:100 primary dilution). Briefly, the tissue samples were de-paraffinized, rehydrated, and antigen retrieval was performed using citrate buffer (ph 6.0) solution for 15 minutes at 105 ºC followed by a 10 minute bench cool down. The samples were then treated with 3% hydrogen peroxide to eliminate endogenous peroxidase activity. The sections were subsequently blocked with a serum-free protein blocking reagent for 20 minutes. Primary antibody detection was accomplished using the following system: The tissue sections were incubated at room temperature for 60 minutes at the noted dilutions followed by a 30 minute incubation utilizing the Envision + System-HRP Labeled Polymer detection method. (Dako, Carpinteria, CA). Staining was completed after incubation with a 3,3'-Diaminobenzidine substrate-chromogen solution. Tissue slides were imaged at 40x magnification and manually scored to determine the percentage of positive cells per high power field. Tissues were evaluated by a certified GI pathologist (MKW). Three high power fields were acquired from a minimum of three separate tumors from each cell line xenograft model.

Immunoblotting

Tumor samples were immediately collected following [^{18}F]-FLT PET and flash frozen in liquid nitrogen. Subsequently, tumor samples were homogenized and diluted to 1 μg/μl in CellLytic lysis buffer (Sigma Aldrich, St. Louis, MO). Prior to resolution by electrophoresis, 20-40 μg of protein from each sample was loaded into 7.5-12% SDS PAGE gels and transferred to PVDF membranes (PerkinElmer, Waltham, MA). Membranes were blocked overnight at 4°C in tris-buffered saline 0.1% Tween-20 (TBST) containing 5% w/v nonfat dry milk powder. Subsequently, membranes were interrogated with antibodies to TS, p21, β-actin (#5499, #2947, #4970, Cell Signaling Technologies, Danvers, MA), and TK1 (Abcam, #57757). Membranes were probed for 1 h at room temperature in TBST with 3% bovine serum albumin.. Membranes were subsequently incubated for 1 h at room temperature with horseradish peroxidase-conjugated secondary antibody (Jackson ImmunoResearch, West Grove, PA) diluted 1:5000 in TBST containing 3% BSA. Western Lightning™ Plus-ECL (PerkinElmer) was used for chemiluminescent detection on a Xenogen IVIS 200. Densitometry was conducted using Living Image 3.2 software (PerkinElmer).

Cell Cycle Assay

HCT-116 and HCT-116*p21*$^{-/-}$ cells were propagated to 50% confluency in 6cm plates. Plates were washed with 2 mL PBS. Cells were then removed with trypsin/EDTA, pelleted, and fixed with 70% ethanol. Fixed cells were pelleted and resuspended in 1 mL PBS prior to the addition of 10 μL of 2 mg/mL DNase-free RNase A. The suspension was incubated at room temperature for 30 min and

labeled with propidium iodide (PI; Sigma Aldrich) according to the manufacturer's protocol. PI-stained cells were analyzed by flow cytometry (FACStar PLUS, BD, Franklin Lakes, NJ). Data analysis was performed using CellQuest software (BD) by manually gating to define and quantify sub-G0, G1, S, and G2/M populations.

Liquid Chromatography/Mass Spectrometry (LC/MS) analysis

Endogenous thymidine levels in HCT-116 and HCT-116*p21*$^{-/-}$ xenograft tumors were analyzed similarly as described by Li et al. (40) using a TSQ Quantum Triple Quadrupole Mass Spectrometer (Thermo Scientific, Maltham, MA). Homogenized tumors were precipitated in methanol and the supernatant was injected onto a 150 x 2.1 mm Hypersil GOLD C18 column (Thermo Scientific) and eluted with a linear gradient of 0.1% formic acid: 0.1% formic acid in acetonitrile form 98:2 to 95:5 for more than 5 minutes at a 0.3 mL/min flow rate.

Statistical Analysis

Differences in the distributions of [^{18}F]-FLT uptake (%ID/g) and histology among cell lines were tested using the non-parametric Wilcoxon Rank Sum (Mann-Whitney U) or Kruskal-Wallis one-way analysis of variance tests using the GraphPad Prism 4 software package. Differences were considered statistically significant if $p < 0.05$. Non-parametric (Spearman) correlations were calculated among the mean expression values from the cell lines for each of 3 metrics of proliferation ([^{18}F]-FLT %ID/g, Ki67 IHC, TK1 IHC). To assess the precision of the

observed correlations, 10,000 bootstrap samples were generated from each of the independent data sets as described (41) and their resulting means and Spearman correlations were calculated. The approximate 95% confidence intervals were obtained from the 2.5^{th} and 95.5^{th} percentiles of the 10,000 bootstrap correlations. A confidence interval containing zero was not considered statistically significant ($p > 0.05$).

4. Results

Comparison of proliferation markers in HCT-116 and DiFi xenograft tumors

To understand the cellular proliferation profiles of DiFi and HCT-116 xenograft tumors, we used IHC to evaluate relationships between TK1 levels, PCNA, a marker of cells in S-phase, and Ki67, a marker of cells in any non-G0-phase (**Fig. 4.2**). Both xenograft models exhibited near-identical Ki67 indices, indicating a similar fraction of proliferating cells at collection (~70% positive cells/ field, $p = 0.0651$). Though Ki67 was similar between the two models, interestingly, PCNA was dramatically different. In HCT-116 xenografts, we observed only slightly fewer PCNA-positive cells than Ki67-positive cells (53.91 ± 3.18 % vs. 68.50 ± 5.52 %, $p = 0.0003$), yet only a small fraction of tumor cells in DiFi xenografts were PCNA-positive (13.59 ± 1.48 % vs. 72.37 ± 12.64 %, $p = 0.0003$). Given its S-phase specificity, TK1 levels tracked more closely with PCNA than Ki67 and, accordingly, were significantly higher in HCT-116 tumors

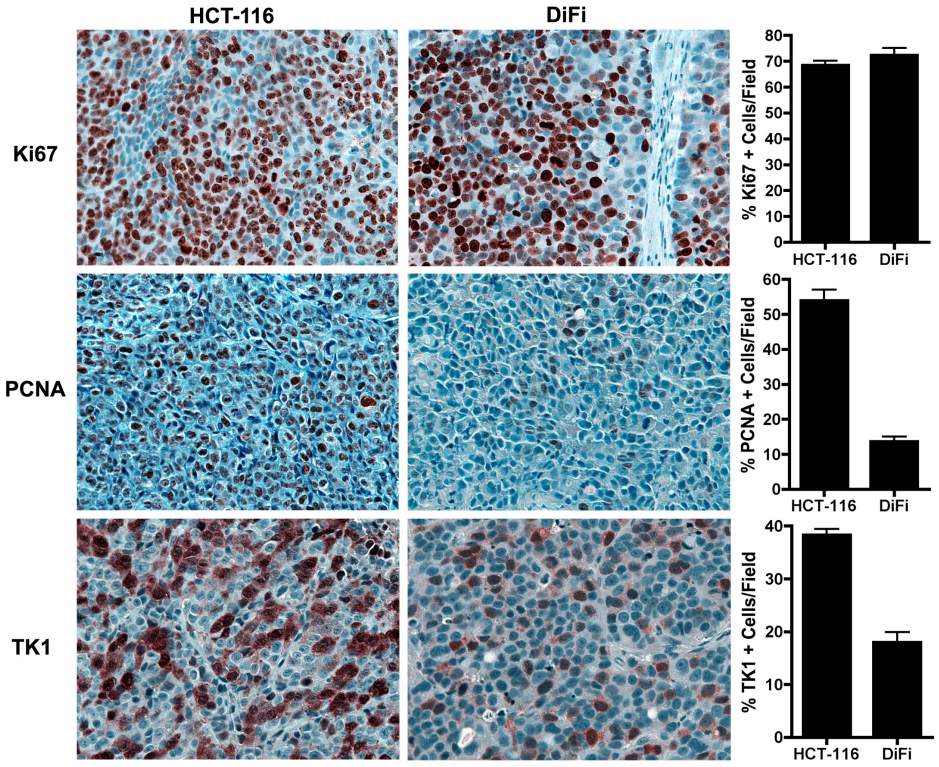

Fig. 4.2. IHC markers of proliferation in HCT-116 and DiFi human CRC xenografts. Representative high power microscopic images (40x) of HCT-116 and DiFi xenograft tissue stained for Ki67, PCNA, and TK1 are shown along with quantification of the percentage of positive cells per field for each marker. HCT-116 and DiFi xenograft tissues exhibit a similar proportion of proliferating cells as measured by Ki67 indices (68.50 ± 5.52 % vs. 72.37 ± 12.64%; p = 0.0651). The proportion of PCNA positive cells, representing S-phase, was significantly increased in HCT-116 xenografts (53.91 ± 3.18 %) compared to DiFi xenografts (13.59 ±1.48%; p = 0.0007). Similar to PCNA, the percentage of TK1-positive cells was significantly higher in HCT-116 xenografts (38.32 ± 1.90 %) than DiFi cells (17.95 ± 3.95 %; p = 0.0007). TK1 indices for both cell lines were reduced compared to Ki67 indices.

than DiFi tumors (p = 0.0005). Overall, TK1 indices were significantly lower than analogous Ki67 indices in both models (HCT-116: 38.32 ± 1.90 % vs. 68.50 ± 5.52 %, p = 0.013; DiFi: 17.95 ± 3.95 % vs. 72.37 ± 12.64 %, p = 0.002), implying that only subset of Ki67-positive cells in either model would be expected to also accumulate [^{18}F]-FLT.

Quantitative [^{18}F]-FLT PET imaging of HCT-116 and DiFi xenograft-bearing mice

We subsequently evaluated [^{18}F]-FLT PET in HCT-116 and DiFi xenograft-bearing mice (**Fig. 4.3**). Compartmental modeling of dynamic PET imaging data was used to determine rate constants that quantitatively reflect tracer delivery, retention, and clearance. Representative time activity curves for HCT-116 and DiFi xenografts and left ventricle estimates of blood pool activity are shown (**Fig. 4.3A/D**). Blood pool characteristics of [^{18}F]-FLT were similar in both models, where the tracer demonstrated a sharp rise following intravenous injection and rapid clearance. HCT-116 xenografts accumulated [^{18}F]-FLT faster and to a greater extent overall compared to DiFi xenografts. Time activity curves could be

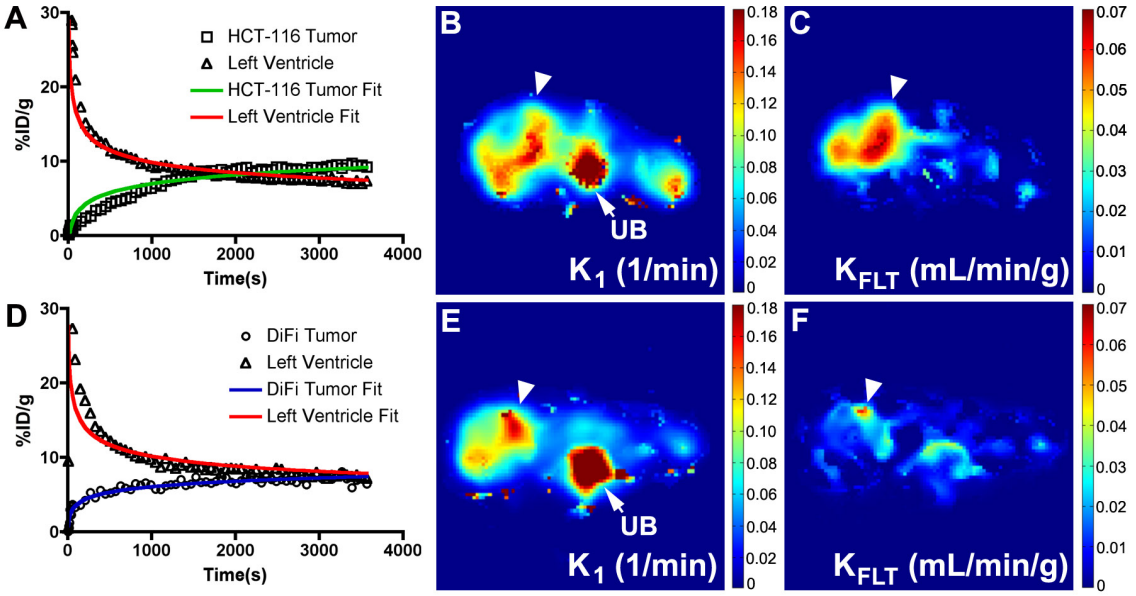

Fig. 4.3 HCT-116 xenografts exhibit higher [^{18}F]-FLT flux than DiFi xenografts. Representative time activity curves for HCT-116 (A) and DiFi (D) xenografts and left ventricle estimates of blood pool activity are shown. In both models, a sharp rise in activity in the blood pool is observed following tracer injection, followed by rapid clearance. Fit lines derived from compartmental modeling closely matched the measured data. Parametric maps reveal heterogeneous intratumoral delivery of [^{18}F]-FLT in both HCT-116 (B) and DiFi (E) xenografts (tumor localized by arrowhead). Increased [^{18}F]-FLT delivery was observed in the urinary bladder (denoted by UB) in both cell line xenografts. The tumor regions exhibiting the greatest [^{18}F]-FLT flux in HCT-116 tumors (C) also exhibited the highest tracer delivery. Only modest [^{18}F]-FLT flux was observed in DiFi xenografts (F), despite having similar delivery as HCT-116 xenografts (B).

fit to a three compartment, four-parameter model in both xenograft models. Rate constants K_1, k_2, and k_4, corresponding to tracer delivery, efflux, and de-phosphorylation, respectively, were not different between HCT-116 and DiFi tumors (**Table 4.1**). As expected based on TK1 IHC, rate constants for [^{18}F]-FLT phosphorylation (k_3) and [^{18}F]-FLT flux (K_{FLT}) were elevated in HCT-116 xenografts compared to DiFi. In fact, the two-fold difference in K_{FLT} between HCT-116 and DiFi xenografts was in close agreement with the difference in TK1 indices by IHC. Delivery of [^{18}F]-FLT, as estimated by K_1 values, was essentially equivalent between HCT-116 and DiFi xenografts. Parametric mapping was used to explore tracer kinetics on a voxel-by-voxel basis (**Fig. 4.3 B/C; E/F**). Intratumoral delivery was heterogeneous in both tumor types (**Fig. 4.3B/E**), with evidence of modest central necrosis in both models. Elevated delivery was noted in xenograft tissue compared with adjacent non-tumor tissue, with the exception of the urinary bladder. In HCT-116 xenografts, tumor regions exhibiting the greatest [^{18}F]-FLT flux also exhibited the greatest tracer delivery (**Fig. 4.3C**). Importantly however, parametric analysis clearly illustrated that the modest flux observed in DiFi xenografts (**Fig. 4.3F**) was not the result of impaired delivery, as DiFi xenografts exhibited similar tracer delivery compared with HCT-116 xenografts (**Fig. 4.3E, Table 4.1**).

Cell Line	K_1 (mL/min/g)	k_2 (1/min)	k_3 (1/min)	k_4 (1/min)	K_{FLT} (mL/min/g)	%ID/g
HCT-116	0.087 ± 0.041	0.094 ± 0.054	0.077 ± 0.013	0.141 ± 0.252	0.042 ± 0.020	8.56 ± 1.17
DiFi	0.105 ± 0.018	0.086 ± 0.019	0.027 ± 0.016	0.027 ± 0.016	0.021 ± 0.005	3.92 ± 1.08
p-value	0.2303	0.4121	0.0061	0.9273	0.0242	<0.0001

Table 4.1. Kinetic parameters derived from compartmental modeling of dynamic [^{18}F]-FLT PET scans in HCT-116 and DiFi tumor xenografts.

Adequacy of static [^{18}F]-FLT PET to evaluate xenograft tumors

Given the complexity and modest throughput of dynamic PET scanning, we evaluated whether similar information regarding [^{18}F]-FLT uptake could be gathered from simple, 20 minute static PET scans following a 40 minute tracer uptake phase. Representative images illustrating the relative 60 minute accumulation of [^{18}F]-FLT (%ID/g) qualitatively illustrate increased [^{18}F]-FLT uptake in HCT-116 xenografts (**Fig. 4.4A**) compared to DiFi (**Fig. 4.4B**) xenografts. Similar to flux data derived from dynamic imaging and compartmental modeling (**Table 4.1**) and TK1 levels by IHC, static imaging resulted in an approximately two-fold difference in [^{18}F]-FLT accumulation between HCT-116 xenografts (8.56 ± 1.17 %ID/g) and DiFi xenografts (3.92 ± 1.08 %ID/g) ($p < 0.0001$). Spatially, the accumulation of [^{18}F]-FLT as visualized by static imaging (**Fig. 4.4A,B**) appeared to be equivalent to K_{FLT} maps derived from compartmental modeling (**Fig. 4.3C,F**). Given that similar metrics of uptake could be obtained from kinetic modeling of dynamic imaging data (K_{FLT}) and simple static imaging (%ID/g) (**Table 4.1, Fig. 4.4C**) , static imaging was used to characterize other cell line xenografts used in the remainder of these studies.

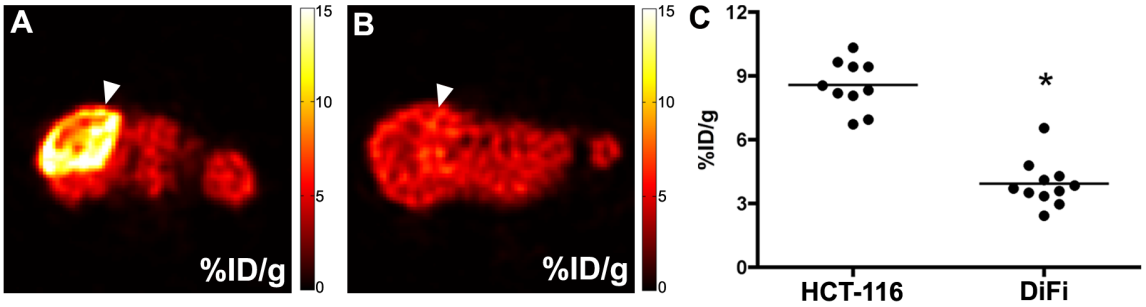

Fig. 4.4. Static [^{18}F]-FLT PET uptake is 2-fold greater in HCT-116 xenografts than DiFi xenografts. Representative 20 minute static PET scans reflect the relative 60 minute accumulation of [^{18}F]-FLT (%ID/g) qualitatively and show increased tracer uptake in HCT-116 xenografts (A) compared to DiFi (B) xenografts (tumor localized by arrowhead). Spatially, %ID/g maps (A,B) are similar to K_{FLT} maps derived from parametric modeling (**Fig. 4.3C,F**). Static PET imaging reveals approximately a 2-fold increase in [^{18}F]-FLT accumulation in HCT-116 xenografts (8.56 ± 1.17 %ID/g) compared to DiFi xenografts (3.92 ± 1.08 %ID/g; $p < 0.0001$) (C) and was similar to [^{18}F]-FLT flux (K_{FLT}) means derived from compartmental modeling (**Table 4.1**).

Effect of de-novo thymidine pathway utilization on [^{18}F]-FLT PET imaging

Using an isogenically matched cell line pair, we initially set out to explore the effect of *p21* deletion upon [^{18}F]-FLT PET, hypothesizing that loss of the cell cycle inhibitor would result in elevated tracer uptake. Indeed, compared to parental HCT-116 cells, HCT-116*p21*$^{-/-}$ cells exhibited a significantly greater S-phase fraction as measured by flow cytometry (25.02% vs. 15.31%; $p = 0.0002$) (**Fig. 4.5A**). Interestingly, compared to parental HCT-116 cells, HCT-116*p21*$^{-/-}$ cells expressed elevated levels of TS, the enzyme responsible for conversion of deoxyuridine to thymidine, and comparatively diminished levels of TK1 (**Fig. 4.5B**). We generated parental HCT-116 and HCT-116*p21*$^{-/-}$ xenograft tumors in nude mice and found that despite this, both models exhibited similar Ki67 indices

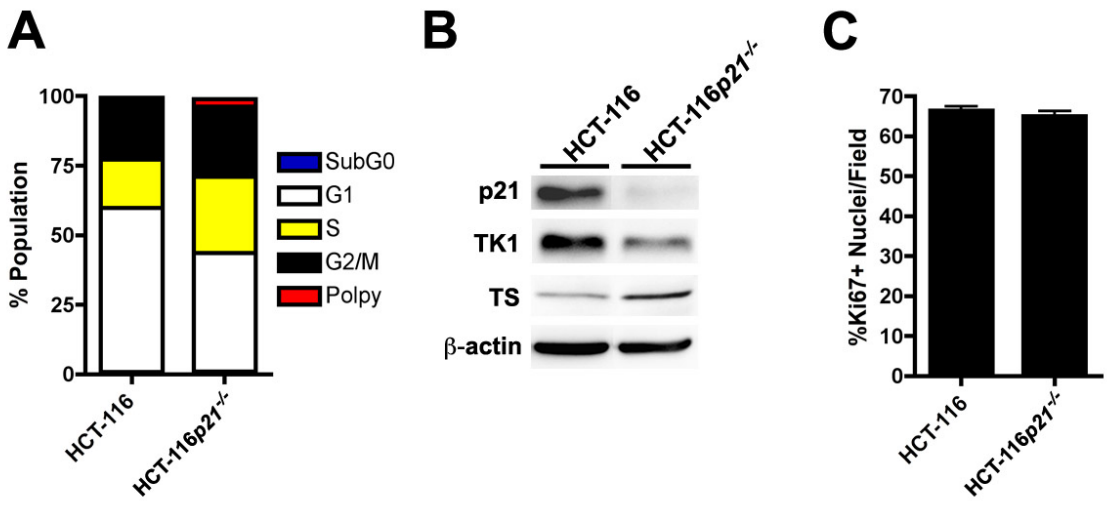

Fig. 4.5. *p21* deletion results in elevated S-phase fraction and *de novo* pathway utilization in HCT-116, although Ki67 remains unchanged. Compared to parental HCT-116 cells, HCT-116*p21*$^{-/-}$ cells exhibited a significantly greater S-phase fraction as measured by flow cytometry (25.02% vs. 15.31%; p = 0.0002) (A). Compared to HCT-116 cells, HCT-116*p21*$^{-/-}$ cells expressed elevated TS protein levels, and comparatively diminished levels of TK1 (B). When grown as xenografts, HCT-116 (68.50 ± 5.52%) and HCT-116*p21*$^{-/-}$ (65.08 ± 3.34%; p = 0.2049) xenografts exhibit similar Ki67 indices (C).

(**Fig. 4.5C**). Thus, parental HCT-116 cells and HCT-116*p21*$^{-/-}$ cells appeared to represent an ideal model system to directly evaluate the impact of the *de novo* pathway on [^{18}F]-FLT uptake *in vivo*.

Similar to our *in vitro* observations, western blot analysis of HCT-116 and HCT-116*p21*$^{-/-}$ xenografts illustrated reduced TK1 levels and elevated TS levels in HCT-116*p21*$^{-/-}$ xenografts compared to the parental cell line (**Fig. 4.6A**). Western blot densitometry of representative xenografts illustrated that HCT-116*p21*$^{-/-}$

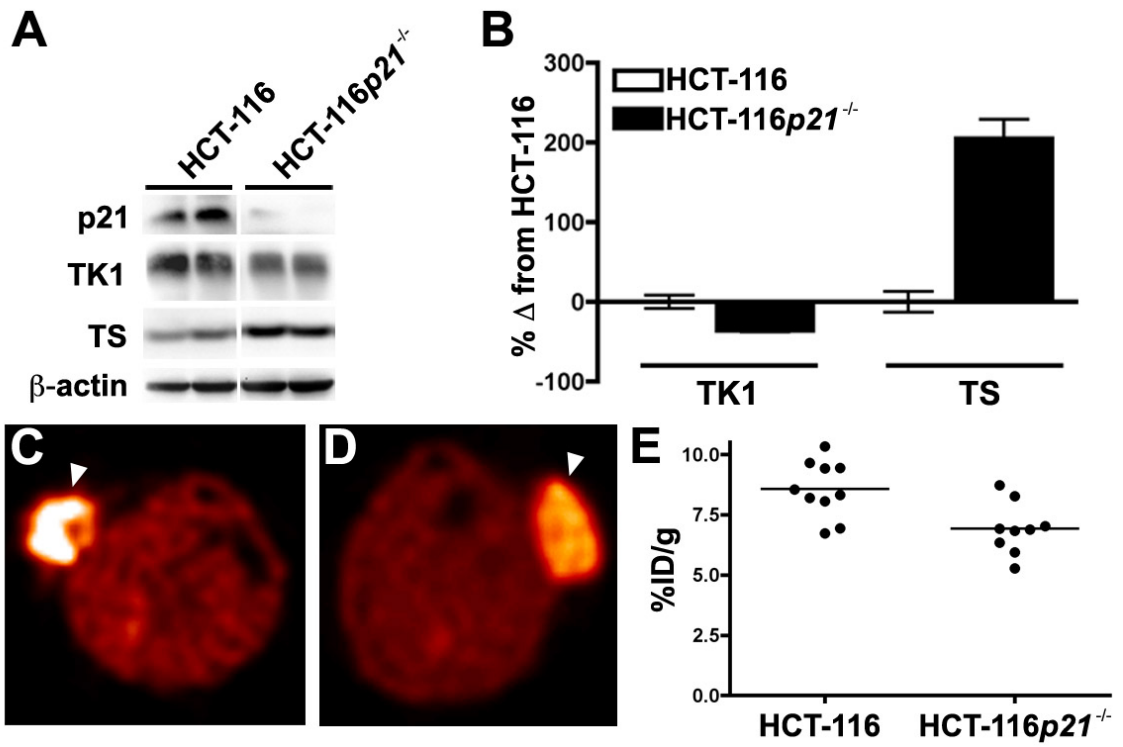

Fig. 4.6. Isogenically matched cell line xenografts illustrate that *de novo* pathway utilization results in decreased [^{18}F]-FLT uptake. Western blot analysis illustrated reduced TK1 levels and elevated TS levels in HCT-116*p21*$^{-/-}$ xenografts compared to wild type HCT-116 xenografts (A). Densitometry of the western blot illustrated that HCT-116*p21*$^{-/-}$ tumors exhibited one-third less TK1 protein and double the TS protein compared to the parental line (B). Illustrating the sensitivity of [^{18}F]-FLT PET to *de novo* pathway utilization, PET imaging of HCT-116 (C) and HCT-116*p21*$^{-/-}$ (D) xenografts closely reflected the relative tumor cell TK1 levels inherent to each model (tumor localized by arrowhead). HCT-116 xenografts (8.56 ± 1.17 %ID/g) exhibited approximately 1/3 greater uptake than analogous HCT-116*p21*$^{-/-}$ xenografts (6.91 ± 1.07 %ID/g; p = 0.005) (E).

tumors exhibited approximately one-third less TK1 protein and approximately double the TS compared to the parental line (**Fig. 4.6B**). Illustrating the sensitivity of [^{18}F]-FLT PET to *de novo* pathway utilization, PET imaging of HCT-116 (**Fig. 4.6C**) and HCT-116*p21*$^{-/-}$ (**Fig. 4.6D**) xenografts closely reflected the relative tumor cell TK1 levels inherent to each model, where HCT-116 xenografts (8.56 ± 1.17 %ID/g) exhibited approximately 1/3 greater uptake than analogous HCT-116*p21*$^{-/-}$ xenografts (6.91 ± 1.07 %ID/g; (p = 0.005) (**Fig. 4.6E**). Since others have suggested that endogenous thymidine levels can impact [^{18}F]-FLT

accumulation in tumors (42), we measured tissue thymidine levels in HCT-116 (37.39 ± 12.61 ng/g tumor) and HCT-116*p21*$^{-/-}$ (19.30 ± 11.86 ng/g tumor) xenografts (**Fig. 4.7**). No statistical difference in thymidine levels was observed (p = 0.400). These data illustrate that *de novo* pathway utilization results in under-estimation of proliferation by [^{18}F]-FLT PET and, importantly, suggests that this metric is incapable of distinguishing moderately proliferative tumors that rely to a greater extent on thymidine salvage from highly proliferative tumors that are more reliant upon the *de novo* pathway.

Statistical correlation between [^{18}F]-FLT PET and proliferation markers

To more broadly evaluate relationships between [^{18}F]-FLT PET, TK1 levels and Ki67 immunoreactivity in common cell line xenograft models, we systematically evaluated these metrics using a colon-centric panel of human

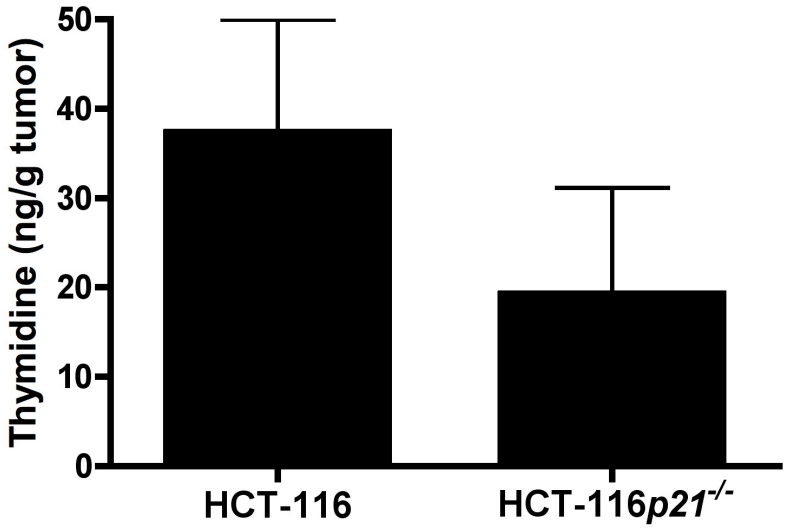

Fig 4.7. Endogenous thymidine levels are similar between HCT-116 and HCT-116*p21*$^{-/-}$ xenografts. HCT-116 tumor xenografts showed similar endogenous thymidine levels (37.39 ± 12.61 ng/g tumor) than HCT-116*p21*$^{-/-}$ xenografts (19.30 ± 11.86 ng/g tumor, p = 0.4000).

cancer cell lines. The cell lines selected contained representative mutations commonly found in human cancer, including *p53*, *BRAF*, *KRAS*, and *PI3K*. Among nine models, [^{18}F]-FLT uptake was highly variable and ranged from 1.66 - 8.89 %ID/g (**Table 4.2**). The mean uptake across the models was significantly different (Kruskal-Wallis, p <0.0001). Ki67 positivity was variable amongst the nine cell line models, but to a lesser degree than [^{18}F]-FLT uptake (**Table 4.2**). However, mean Ki67 scoring remained significantly different amongst the cell lines by Kruskal-Wallis analysis (p < 0.0001). TK1 IHC was evaluated in seven of the nine models (**Table 4.2**); the percentage of TK1 positive cells per field was significantly different amongst those evaluated (p < 0.0001). No statistically significant relationships were observed among mutation status (*p53*, *BRAF*, *KRAS*, *PI3K*) and [^{18}F]-FLT uptake, Ki67 IHC scoring, or TK1 IHC scoring. The observed Spearman (nonparametric) correlations between [^{18}F]-FLT PET, Ki67,

Cell Line	[^{18}F]-FLT uptake (% ID/g)		Ki67 score (% + cells/field)		TK1 score (% + cells/field)		*p53*	*BRAF*	*KRAS*	*PI3K*
	Mean	SD	Mean	SD	Mean	SD				
HCT-116	8.69	1.57	68.50	5.52	38.32	1.90	WT	WT	Mut	Mut
HCT-116*p53*$^{-/-}$	7.77	0.99	64.52	5.56	32.97	4.63	-	WT	Mut	Mut
HCT-116*p21*$^{-/-}$	6.91	1.07	65.08	3.34	19.06	1.71	WT	WT	Mut	Mut
Colo-205	5.65	1.20	62.14	8.99	17.98	4.90	Mut	Mut	WT	WT
Lim 2405	5.24	1.19	85.57	3.63	41.36	4.27	WT	Mut	WT	WT
BT474	4.25	0.79	57.32	4.28	-	-	Mut	WT	WT	Mut
DiFi	3.72	0.99	72.37	12.64	17.95	3.95	Mut	WT	WT	WT
HT-29	3.20	0.65	58.37	9.14	21.73	3.66	Mut	Mut	WT	Mut
SW620	1.66	0.21	74.22	6.35	-	-	Mut	WT	Mut	WT

Table 4.2. Characterization of [^{18}F]-FLT uptake, IHC scoring and tumor mutation status in 8 CRC and one breast cancer cell line xenografts.

and TK1 are found in **Table 4.3**. The Spearman correlation coefficient between [^{18}F]-FLT uptake and Ki67 indices was -0.07 ($p > 0.05$), indicating correlation between these metrics consistent with random variation. However, a statistically significant ($p < 0.05$) Spearman correlation coefficient of 0.36 was observed between [18F]-FLT uptake and TK1 scoring. Among the seven cell line models with both Ki67 and TK1 IHC, a statistically significant ($p < 0.05$) Spearman correlation coefficient of 0.29 was observed. Using 10,000 bootstrap correlations derived from the data sets, ninety-five percent confidence intervals were constructed from the 2.5th and 97.5th percentiles of the bootstrapped correlations. (**Table 4.3**). As the ninety-five percent confidence intervals for [^{18}F]-FLT uptake and TK1, as well Ki67 and TK1 scoring, did not contain 0, they were considered statistically significant ($p < 0.05$). However, the correlation between [^{18}F]-FLT uptake and Ki67 scoring was not significant.

5. Discussion

Currently, there is considerable enthusiasm for advancing [^{18}F]-FLT PET as a cancer imaging biomarker, especially in drug development. Commercial access

Marker 1	Marker 2	Spearman Correlation (95% confidence interval)
% ID/g	Ki67	-0.07 (-0.233 to 0.217)
% ID/g	TK1	0.36 (0.142 to 0.643)
Ki67	TK1	0.29 (0.107 to 0.786)

Table 4.3. Summary of Spearman correlation statistics between [^{18}F]-FLT uptake and IHC proliferation markers including 95th percentile confidence intervals from bootstrap estimates.

to [^{18}F]-FLT is increasing, as well as a heightened awareness of the potential of [^{18}F]-FLT PET as a non-invasive biomarker in oncology. These efforts should be accompanied by further basic and clinical research to better inform its interpretation and use. [^{18}F]-FLT is not a new tracer, and the degree to which [^{18}F]-FLT PET quantitatively reflects proliferative index has been continuously debated for more that a decade. Pre-clinical and clinical studies have demonstrated varying degrees of agreement between [^{18}F]-FLT uptake in tumors and histological markers of proliferation. In a recent survey of published preclinical studies, [^{18}F]-FLT uptake was found to correlate with Ki67 indices in lung cancer (43), B-cell lymphoma (32) and epithelial cancer (43), but did not correlate with Ki67 in colorectal cancer (44), neuroblastoma (45), or across a variety of xenograft types (42). Clinically, [^{18}F]-FLT PET has been correlated with Ki67 to varying degrees as well. Correlation has been observed in lymphoma (46) and thoracic (47, 48) cancers, but not esophogeal tumors (49). Both correlation and lack thereof has been observed in human lung (33, 50, 51), breast (52, 53), and colorectal (54, 55) cancer. Recently, we found that [^{18}F]-FLT PET served as a non-invasive surrogate of Ki67 in Ménétrier's disease, a rare hyperproliferative disorder of the stomach (56). Unlike our present study, other studies have not always found TK1 levels to correlate with [^{18}F]-FLT PET uptake in a number of studies (33, 42). Based upon this diversity of results and our desire to use non-invasive measurements of proliferation to predict treatment response (25, 26, 56) we explored the relationship between [^{18}F]-FLT uptake and cellular metrics of proliferation in a variety of treatment-naive tumors.

Determinants of [^{18}F]-FLT PET include delivery, internalization, and intracellular trapping. Delivery may be affected by a number of factors including tissue vascularity, blood vessel permeability, and extravasation. The activity of nucleoside transporters are required to shuttle [^{18}F]-FLT from the extracellular to intracellular environment. Via compartmental modeling, we demonstrate that the sum of these processes is similar in two xenograft models that exhibit very large differences in [^{18}F]-FLT retention (**Table 4.1, Figs. 4.2, 4.3**). Even though kinetic modeling results were comparable to static imaging results in simple xenografts, dynamic [^{18}F]-FLT PET may still have value in studies where vascularity is uncertain or in certain organ sites. For example, Muzi *et al.* showed that delivery was the dominant factor governing [^{18}F]-FLT retention in gliomas where the blood brain barrier has been compromised (19).

Following delivery and internalization in a cell, [^{18}F]-FLT is phosphorylated by TK1 to promote trapping which, in turn, generates imaging contrast. TK1 is primarily expressed in late G1- and S-phase of cell cycle before being degraded prior to G2- and M-phase (15). As such, highly proliferative tumors with comparatively modest fraction of cells in S-phase exhibit similarly modest TK1 levels. This situation was modeled by comparing HCT-116 and DiFi xenografts. In these models, despite similar Ki67 indicies, we observe disparate PCNA and TK1 indicies (**Fig. 4.2**), which agrees with the difference in [^{18}F]-FLT PET between the models (**Fig. 4.3, 4.4**). In this situation, [^{18}F]-FLT PET serves as a much more sensitive marker of DNA synthesis than Ki67, but does not reflect overall proliferation adequetely, especially in DiFi xenografts. We showed that utilization

of the *de novo* pathway of thymidine synthesis further decouples [^{18}F]-FLT PET from Ki67 indices, as shown in our comparison of the HCT-116 and HCT-116*p21*$^{-/-}$ xenografts (**Fig. 4.6)**. These results agree with Moroz *et al.* who suggested that [^{18}F]-FLT uptake was unrepresentative of xenograft growth in tumors utilizing the de novo pathway utilization (57). Recently, Zhang et al. (42) reported that [^{18}F]-FLT uptake was inversly related to endogenous thymdine levels. However, in our study which featured the isogenically matched HCT-116 and HCT-116*p21*$^{-/-}$ xenografts we failed to observe any relationship between thymidine levels and [^{18}F]-FLT uptake (**Fig. 4.7**).

Perhaps it is unfortunate that Ki67 has historically been the gold standard for validation of [^{18}F]-FLT PET imaging as evidenced by the conflicting correlations between these two markers. Nuclear Ki67 staining is positive for cells in any non-G0 phase of cell cycle and thus serves as a general marker of cell proliferation. In contrast, the closer association of [^{18}F]-FLT uptake with TK1 activity, which is typically confined to S-phase, suggests that information regarding proliferation obtained from [^{18}F]-FLT PET imaging is unique and more specific than Ki67. We illustrate this point using 9 different human tumor xenograft cell lines. [^{18}F]-FLT uptake is correlated with TK1 indices, but not Ki67 (**Table 4.3**). Since Ki67 is not S-phase specific, it is reasonable that [^{18}F]-FLT PET may poorly correlate with Ki67, especially in the prognostic setting.

6. Conclusion

Our findings illustrate that [^{18}F]-FLT PET reflects tumor proliferation as a function of thymidine salvage pathway utilization. Unlike more generalizable proliferation markers, such as Ki67, [^{18}F]-FLT PET reflects proliferative indices to variable and potentially unreliable extents. [^{18}F]-FLT PET cannot discriminate moderately proliferative, thymidine salvage-driven tumors from those of high proliferative index that rely primarily upon *de novo* thymidine synthesis. Accordingly, the magnitude of [^{18}F]-FLT uptake should not be considered a surrogate of proliferative index. These may explain, at least in part, the diversity of [^{18}F]-FLT PET correlative results previously reported and suggest future best-practices when [^{18}F]-FLT PET is employed in oncology.

CHAPTER 5

[^{18}F]-FLT PET PREDICTS RESPONSE TO ^{V600E}BRAF-TARGETED THERAPY IN PRECLINICAL MODELS OF COLORECTAL CANCER

1. Abstract

Selective inhibition of oncogenic targets and associated signaling pathways forms the basis of personalized cancer medicine. The clinical success of ^{V600E}BRAF inhibition in melanoma, coupled with the emergence of acquired resistance, underscores the importance of rigorously validating quantitative biomarkers of treatment response in this and similar settings. Since constitutive activation of BRAF leads to proliferation in tumors, we explored [^{18}F]-FLT PET to non-invasively quantify changes in tumor proliferation that are associated with pharmacological inhibition of ^{V600E}BRAF downstream effectors and that precede changes in tumor volume.

Methods: Human colorectal cancer (CRC) cell lines expressing *^{V600E}BRAF* were used to explore relationships between up-regulation of p27 and phosphorylation of BRAF downstream effectors upon small molecule ^{V600E}BRAF inhibitor exposure. Athymic nude mice bearing *^{V600E}BRAF*-expressing human CRC cell line xenografts were treated with a small molecule ^{V600E}BRAF inhibitor (or vehicle) daily for ten days. Predictive [^{18}F]-FLT PET was conducted prior to changes in tumor volume. Correlations were evaluated among PET imaging, inhibition of p-MEK and p-ERK by western blot, tumor proliferation by histology, and small molecule exposure by MALDI imaging mass spectrometry (IMS).

Results: Treatment of CRC cell lines with PLX4720 reduced proliferation associated with target inhibition and up regulation of p27. *In vivo,* PLX4720 treatment reduced [^{18}F]-FLT uptake, but not [^{18}F]-FDG uptake, in Lim2405 xenografts prior to quantifiable differences in xenograft volume. Reduced [^{18}F]-FLT PET reflected a modest, yet significant, reduction of Ki67 immunoreactivity, inhibition of p-MEK and p-ERK, and elevated tumor cell p27 protein levels. Both [^{18}F]-FLT PET and [^{18}F]-FDG PET accurately reflected a lack response in HT-29 xenografts, which MALDI IMS suggested may have stemmed from limited PLX4720 exposure.

Conclusions: We utilized preclinical models of CRC to demonstrate [^{18}F]-FLT PET as a sensitive predictor of response to ^{V600E}BRAF inhibitors. Since [^{18}F]-FLT PET predicted reduced proliferation associated with attenuation of BRAF downstream effectors, yet [^{18}F]-FDG PET did not, these data suggest that [^{18}F]-FLT PET may represent an alternative to [^{18}F]-FDG PET for quantifying clinical responses to BRAF inhibitors.

2. Introduction

BRAF is the most frequently mutated protein kinase in human cancer (58). A variety of activating mutations in *BRAF* exist, though the V600E mutation, which substitutes glutamic acid for valine, is the most commonly observed (59). This mutation results in constitutive activation of BRAF and associated downstream effectors within the mitogen-activated protein kinase (MAPK)

pathway (60). Tumor expression of ^{V600E}*BRAF* correlates with increased proliferation, aggressiveness, and poor prognosis (61, 62). Furthermore, growth and proliferation of tumors that express ^{V600E}*BRAF* tend to depend on MAPK pathway activity, illustrating the attractiveness of pharmacological inhibition of BRAF in these tumors (63). A majority of melanomas (64) and thyroid cancers (65) express ^{V600E}*BRAF*. Expression of mutant *BRAF* has been observed in other solid tumors, such as colon cancer (~15%) (58, 66). Recent studies have shown that inhibition of mutant BRAF with therapeutic small molecules (e.g., PLX4032) leads to reduced proliferation and tumor regression in melanoma (67, 68). In this disease, reduced proliferation following PLX4032 stems from inhibition of BRAF effectors (e.g., p-MEK, p-ERK) and up-regulation of cell cycle inhibitors (e.g., p21, p27) (69, 70).

The relationship between BRAF inhibition, reduced proliferation, and clinical response in ^{V600E}*BRAF* melanoma suggests that non-invasive imaging metrics of proliferation may represent promising biomarkers of efficacy in this setting. Analogously, recent studies have associated proliferation with acquired resistance to BRAF inhibitors in melanoma (71). Additionally, clinical results evaluating ^{V600E}BRAF inhibition in other solid tumors, such as colon cancer (72), have been less promising for reasons that may include resistance-mediated proliferation (73). The widely used PET tracer 2-deoxy-2-[^{18}F]fluoro-D-glucose ([^{18}F]-FDG) has been utilized to document clinical response to BRAF inhibition in melanoma (67, 74), though tissue uptake of this tracer reflects a host of metabolic processes only tangentially related to proliferation. In contrast, PET

imaging with 3'-deoxy-3'-[^{18}F]-fluorothymidine ([^{18}F]-FLT) measures proliferation more directly by targeting thymidine salvage, which is related to DNA synthesis.

In this study, we utilized preclinical models of CRC to demonstrate [^{18}F]-FLT PET as a sensitive predictor of response to ^{V600E}BRAF inhibitors. In a ^{V600E}BRAF-sensitive model, [^{18}F]-FLT PET predicted tumor growth arrest and reduced proliferation associated with attenuation of BRAF downstream effectors that was undetectable with [^{18}F]-FDG PET. In another model, [^{18}F]-FLT PET accurately reflected a lack of *in vivo* response that appeared to stem from limited drug exposure in tumor tissue. Our data suggests that [^{18}F]-FLT PET represents an alternative to [^{18}F]-FDG PET for quantifying clinical responses to BRAF inhibitors in ^{V600E}*BRAF*-expressing solid tumors.

3. Materials and Methods

In vitro studies

HT-29 (ATCC HTB-38) human CRC cell lines were obtained from ATCC and Lim2405 cells were provided by Dr. Robert Whitehead, Ludwig Institute for Cancer Research. Cell lines were maintained as sub-confluent monolayer cultures in 10-cm plates in a 95% humidity, 5% CO_2, 37°C atmosphere in Dulbecco's Modified Eagle's Medium (DMEM; Mediatech). Growth medium was supplemented with 10% fetal bovine serum (Atlanta Biologicals) and 1 mg/mL gentamycin sulfate (Gibco). PLX4720 was synthesized as described (75) and was prepared as a 10 mM stock solution in dimethyl sulfoxide (DMSO) and aliquoted to achieve final drug concentrations as noted.

Lim2405 and HT-29 cells were propagated to 50% confluency in 6-cm plates. Cells were treated with PLX4720 (0, 10, 250, 1000, 5000 nM) for 24 h and prepared for flow cytometry as described (25, 76). Propidium iodide (PI)-stained cells were analyzed by flow cytometry (FACStar PLUS, Becton-Dickinson). Data analysis was performed using CellQuest software (Becton-Dickinson) by manually gating to define and quantify sub-G0, G1, S, and G2/M populations.

In vivo studies

All studies involving animals were conducted in compliance with federal and institutional guidelines. Cell line xenografts were generated in 5-6 week old female athymic nude mice (Harlan Sprague-Dawley) following subcutaneous injection of $1x10^7$ cells on the right flank. Palpable tumors were detected within 2 to 3 weeks post-implantation. Experiments commenced once tumor volumes reached 150-200 mm^3. For treatment, tumor-bearing mice were administered 60 mg/kg PLX4720 or saline vehicle by oral gavage (100 µL total volume) daily. PET imaging was conducted on day 3 for [^{18}F]-FDG, 16-20 h following the second PLX4720 dose, and day 4 for [^{18}F]-FLT, 16-20 h following the third PLX4720 dose, prior to changes in volume between vehicle-treated and PLX4720-treated tumors. For longitudinal volume assessment, xenograft-bearing mice received a single 60 mg/kg dose of PLX4720 for 10 consecutive days.

Radiopharmaceutical synthesis

[^{18}F]-FLT was prepared from ^{18}F-fluoride in a two-step, one-pot reaction as previously described (25, 77) using a GE TRACERlab FX-FN automated module. Aqueous ^{18}F-fluoride was eluted with Kryptofix-222 and K_2CO_3 in CH_3CN/H_2O into the reaction vessel. Three sequences of heating (110°C) with He(*g*) flow resulted in dry ^{18}F-fluoride/Kryptofix-222/K_2CO_3. The cyclic precursor 2,3′-anhydro-5′-*O*-benzoyl-2′-deoxythymidine (ABX Advanced Biochemical Compounds) was added in DMSO and reacted for 10 min at 160°C. The benzoyl-protecting group was removed from the labeled intermediate by basic hydrolysis (0.25 mol/L NaOH, 50°C, 10 min). The reaction mixture was purified on a semi-preparative C-18 high-performance liquid chromatography column eluting with 10% ethanol/10 mmol/L sodium phosphate buffer and sterilized by 0.2 μm membrane filtration. Radiochemical identity, purity, and specific activity were determined by analytic high-performance liquid chromatography. The [^{18}F]-FLT product was obtained with average radiochemical purity of 98.3% and specific activity of 345.5 TBq/mmol. [^{18}F]-FDG was synthesized in the Vanderbilt University Medical Center Radiopharmacy and distributed by PETNET. The average radiochemical purity of the product was 98.5% and specific activity was more than 37 TBq/mmol.

Imaging

PET imaging was performed using a dedicated small animal PET scanner (Concorde Microsystems Focus 220) as described (25). Briefly, mice were maintained under 2% isoflurane anesthesia in 100% oxygen at 2 L/min and kept

warm via a circulating water heating pad during the PET scan. Mice were administered 7.4-9.3 MBq of [^{18}F]-FLT intravenously and allowed free access to food and water during a 40 minute uptake period followed by a 20 min PET acquisition. For [^{18}F]-FDG, mice were fasted for approximately 6 h prior to imaging and warmed in a heated (31º C) chamber for 1 h prior to [^{18}F]-FDG injection and during the uptake period to minimize brown fat uptake of [^{18}F]-FDG. Mice were administered 7.4-9.3 MBq of [^{18}F]-FDG intravenously and allowed free access to water during a 50 minute uptake period followed by a 10 min PET acquisition.

High-resolution ultrasound measurement of xenograft volumes was conducted as previously described (78). Briefly, 3-dimensional ultrasound imaging data sets were collected for each xenograft using a Vevo 770 ultrasound microimaging system (VisualSonics). Mice were anesthetized using 2% isoflurane in oxygen and remained on a heated stage during the course of imaging. Xenografts were covered in warmed (37°C) Aquasonic 100 ultrasound gel (Parker Laboratories) and centered in the imaging plane. Three-dimensional B-mode data were acquired by automated translation of the 30-MHz ultrasound transducer along the entire length of the xenograft.

For PET imaging, scans were reconstructed using OSEM3D/MAP as described (79). The resulting three-dimensional reconstructions had a voxel size of 0.474 mm in the x-y plane and 0.796 mm inter-slice. ASIPro software (Siemens) was used to manually draw three-dimensional regions of interest (ROIs) around the tumor volumes in the reconstructed images. [^{18}F]-FLT uptake

was quantified and expressed as percent injected dose per gram of tissue (%ID/g) by dividing the ROI activity by the injected dose and multiplying by 100. For volumetric analysis of xenografts, ultrasound data was imported into Amira 5.2 (Visage Imaging). Tumors were manually segmented and volume was determined by summation of the in-plane segmented regions and multiplying by the inter-slice spacing.

Antibodies and immunoblotting

In vitro cell samples were collected from 10-cm plates following 48 h of PLX4720 exposure. For immunoblotting, media was removed and cell monolayers were washed with PBS prior to the addition of 450 µL lysis buffer (7 mL CelLytic M lysis buffer (Sigma), mini protease inhibitor cocktail (Roche), 100 µL phosphatase inhibitor cocktail 1 and 2 (Sigma). Protein concentrations were normalized using a BCA assay. Frozen tumor samples were subsequently homogenized and diluted to 1 µg/µL in lysis buffer. All samples were vortexed and centrifuged to collect the final cell lysate.

For western blotting, 20-40 µg of protein was loaded into 7.5-12% SDS PAGE gels and resolved by electrophoresis. Membranes were immunoblotted with antibodies to p-MEK1/2 (Cell Signaling #9154S), total MEK (Cell Signaling #9126), p-ERK1/2 (Cell Signaling #4370S), total ERK (Cell Signaling #4695), p27 (Cell Signaling #3686S), and β-tubulin (Novus Biologicals #NB600-936). The membranes were imaged on a Xenogen IVIS 200 using Western Lightning Plus-ECL (PerkinElmer) substrate.

Immunohistochemistry

Immediately following sacrifice, excised tumors were fixed in 10% formalin for 24 h and transferred to 70% ethanol. Samples were then blocked in paraffin and sectioned prior to immunostaining for Ki67 (Dako #M7240) and TK1 (Abcam #57757). Tissues were evaluated by an expert GI pathologist (MKW). Stained samples were imaged at 40x magnification and analyzed for expression of histological markers. The index for each marker was expressed as the average number of positive cells per field based on counting ≥ 3 random fields per tumor section and 3 sections per condition.

MALDI IMS

Immediately following PET imaging, xenograft-bearing mice were sacrificed, placed in 50mL conical tubes containing de-ionized water and subsequently frozen using dry ice. Transverse sections prepared for MALDI IMS as described (80, 81). Mass spectra were acquired in positive-ion mode using a MALDI LTQ XL linear ion trap mass spectrometer. An average of 15 laser shots/ scan was used to produce a mass spectrum every 200 μm laterally across the tissue. Two dimensional ion density images were extracted from raw data using ImageQuest (version 1.0.1; Thermo Scientific, San Jose, CA, USA). False color ion ion intensity maps were co-registered with white light images to visualize drug concentration in the mouse tissues (80).

Statistics

Statistical significance of data were evaluated using the non-parametric Wilcoxon Rank Sum (Mann-Whitney U) tests in GraphPad Prism 4. Data were considered significant if $P < 0.05$.

4. Results

In vitro sensitivity of CRC cells to PLX4720

The *V600EBRAF* expressing Lim2405 and HT-29 cell lines exhibited marked sensitivity to PLX4720, characterized primarily by concentration-dependent G1-arrest and decreased S-phase (**Figure 5.1A**) as measured by PI flow cytometry**.** Other cell cycle phases were only modestly affected, suggesting that primary effect of PLX4720 exposure in these cell lines was diminished DNA synthesis.

Reasoning that [^{18}F]-FLT PET measures cellular proliferation in a S-phase dependent manner, we utilized Lim2405 and HT-29 cells to explore the

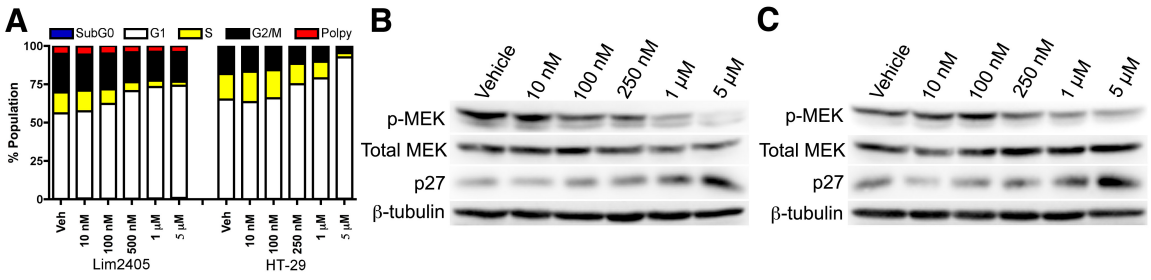

Figure 5.1. *In vitro* PLX4720 exposure decreases proliferation and leads to elevated p27 levels in human CRC cell lines harboring *V600EBRAF*. Lim2405 and HT-29 cells expressing *V600EBRAF* exhibited marked sensitivity to PLX4720. (**A**) PI flow cytometry demonstrated concentration-dependent G1-arrest and decreased S-phase fractions**.** Western blot analysis of lysates collected from HT-29 (**B**) and Lim2405 (**C**) cells following 48 hr *in vitro* PLX4720 exposure (0, 10 nM, 100 nM, 250 nM, 1 μM, 5 μM) are shown. In both cell lines, p-MEK was inhibited at concentrations greater than 250 nM. Additionally, increased p27 protein expression was observed at PLX4720 concentrations greater than 250 nM.

relationship between inhibition of BRAF downstream effectors and cell cycle inhibitors. As expected, PLX4720 treatment resulted in reduced p-MEK by 50% or greater at concentrations of approximately 250 nM and above for both Lim2405 (**Figure 5.1B**) and HT-29 (**Figure 5.1C**). Levels of p27 were inversely related to p-MEK following PLX4720 exposure.

In vivo sensitivity of Lim2405 xenografts to PLX4720

Mice bearing Lim2405 xenografts were used to evaluate early, post-treatment [^{18}F]-FLT PET to predict changes in xenograft volume stemming from small molecule BRAF inhibitor exposure. Mice were treated daily with PLX4720 over a 10-day treatment course. PLX4720 treatment resulted in significant growth arrest of Lim2405 xenografts that was detectable using high-resolution ultrasound imaging by day 7 (**Figure 5.2A**). [^{18}F]-FLT PET imaging of xenograft-bearing mice was conducted on day 4, when there was no quantifiable difference in xenograft volume between PLX4720-treated and vehicle-treated cohorts. We found [^{18}F]-FLT uptake to be significantly reduced in PLX4720-treated Lim2405 xenografts (9.9 ± 1.4 %ID/g, N = 5) compared to similar vehicle-treated controls (14.9 ± 1.5 %ID/g. N = 5) (**Figures 5.2B/C**). Analogously, pre-treatment/post-treatment comparisons of individual mice showed a statistically significant

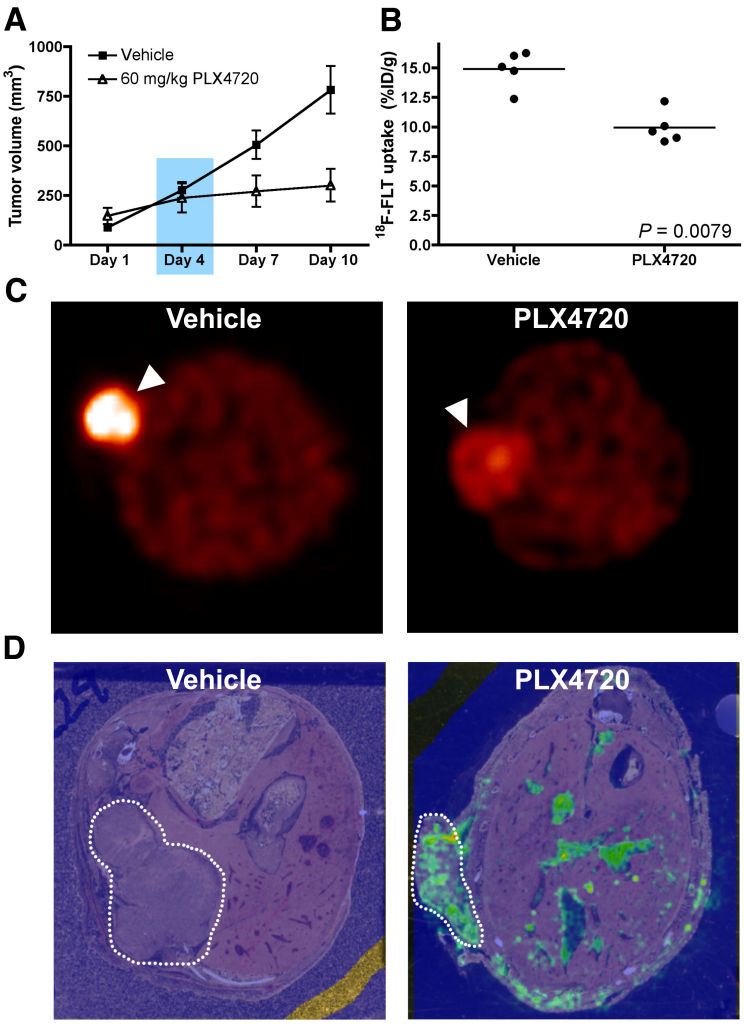

Figure 5.2. Reduced *in vivo* [^{18}F]-FLT PET precedes quantifiable, PLX4720-dependent differences in tumor volume and correlates with drug exposure in Lim2405 xenografts. Mice bearing Lim2405 xenografts were treated daily with PLX4720 or vehicle. (**A**) Over a 10 day regimen, PLX4720 treatment induced significant xenograft growth arrest detectable by treatment day 7. [^{18}F]-FLT PET was carried out on treatment day 4 when there was negligible difference in tumor volume between PLX4720-treated and vehicle-treated controls (blue box). (**B**) Representative transverse images of vehicle-treated and PLX4720-treated cohorts collected on treatment day 4 (xenograft denoted by arrowhead). (**C**) [^{18}F]-FLT PET was significantly lower in PLX4720-treated xenografts compared to vehicle-treated controls. Immediately following PET, mice were sacrificed and thin, transverse sections of vehicle-treated and PLX4720-treated mice were prepared for MALDI IMS. (**D**) Pseudocolor maps of ion intensity corresponding to the parent molecular mass of PLX4720 demonstrate minimal signal intensity in vehicle-treated animals. In contrast, treated animals demonstrated considerable PLX4720 ion intensity, with the drug primarily localized to tumor tissue (dotted line). Other tissues exhibiting PLX4720 ion intensity included the bowel, consistent with oral administration.

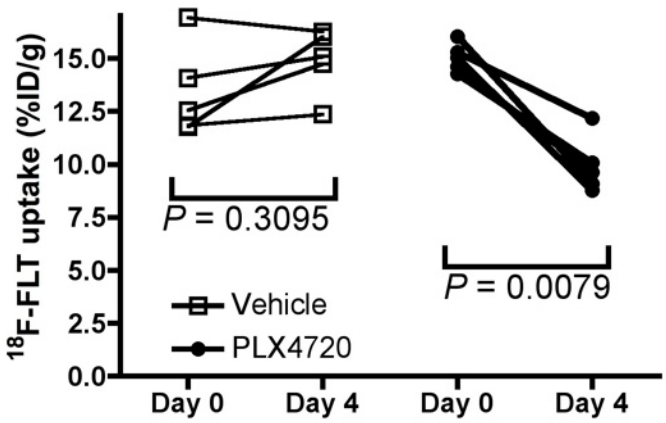

Figure 5.3. Pre-treatment/post-treatment comparison of [^{18}F]-FLT uptake in Lim2405 xenograft tumors. Pre-treatment and post-treatment [^{18}F]-FLT uptake was similar in vehicle-treated Lim2405 xenografts. In PLX4720-treated xenografts, [^{18}F]-FLT was significantly reduced for each individual mouse imaged.

decrease following PLX4720 exposure, but not following vehicle exposure group (**Figure 5.3**). Unlike [^{18}F]-FLT PET, [^{18}F]-FDG PET was not significantly different between vehicle-treated and PLX4720-treated Lim2405 xenograft tumors (**Figure 5.4**). A subset of mice were immediately sacrificed following imaging for correlative analysis that included preparation of whole-animal transverse thin sections for MALDI IMS; this technique was used to evaluate relative PLX4720 tissue concentrations and the spatial distribution in Lim2405 xenograft-bearing mice at the time of imaging. Pseudocolor maps of the MALDI ion intensity corresponding to the parent molecular mass of PLX4720 confirmed the presence of un-metabolized drug in tumors and adjacent non-tumor tissues such as the bowel. No background ion intensity was observed in vehicle-treated mice (**Figure 5.2D**).

Western blot analysis of imaging-matched Lim2405 xenograft tissues harvested shortly following imaging on treatment day 4 illustrated that reduced

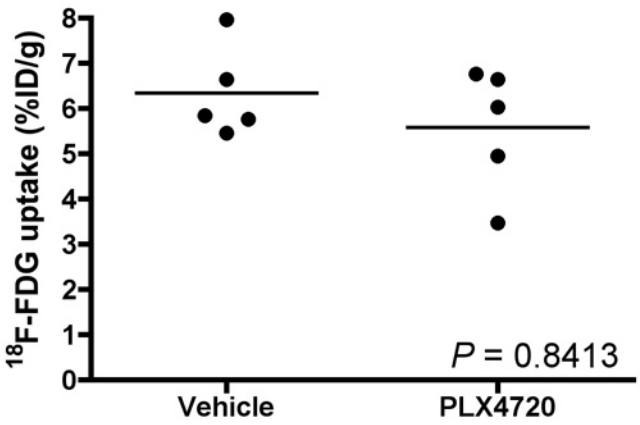

Figure 5.4. [^{18}F]-FDG PET is similar between vehicle-treated and PLX4720-treated Lim2405 xenograft tumors. Contrary to [^{18}F]-FLT PET (*see **Figure 5.2, Figure 5.3**)*, no statistically significant difference in [^{18}F]-FDG uptake was observed between vehicle-treated and PLX4720-treated Lim2405 xenografts.

[^{18}F]-FLT PET was associated with approximately 50% inhibition of p-MEK and p-ERK (**Figure 5.5**) and an approximately 2-fold up-regulation of p27 levels. Using immunohistochemistry, we observed a 25% reduction in TK1 positivity in PLX4720-treated Lim2405 xenografts compared to vehicle-treated controls (**Figures 5.6A/B**). Similarly, Ki67 immunoreactivity was also reduced in PLX4720-treated tumors (**Figures 5.6A/B**), although to a lesser extent than observed for TK1.

In vivo sensitivity of HT-29 xenografts to PLX4720

Analogous to studies with Lim2405 xenografts, mice bearing HT-29 xenografts were treated daily with PLX4720 or vehicle over a 10-day treatment course. No difference in xenograft volume was observed between PLX4720-treated and vehicle-treated mice over the 10 day treatment course. (**Figure 5.7A**). Unlike Lim2405 xenografts, at day 4, [^{18}F]-FLT uptake was similar

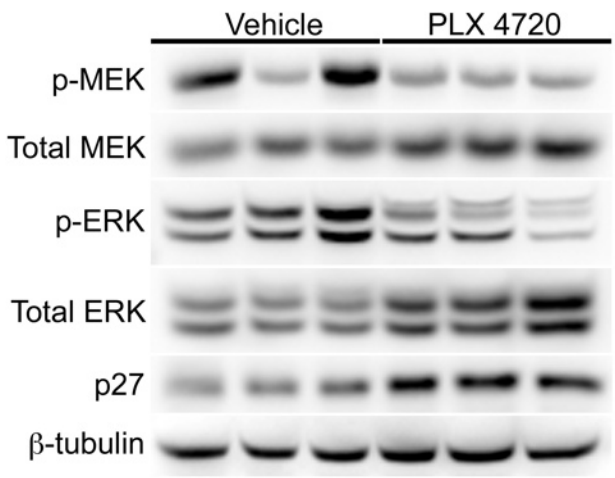

Figure 5.5. Early [^{18}F]-FLT PET predicts inhibition of BRAF downstream effectors and p27 up-regulation. Western blot analysis quantifying BRAF effector molecules and p27 in [^{18}F]-FLT PET imaging-matched Lim2405 xenografts (*see **Figure 2***). Compared to vehicle controls, xenografts harvested from PLX4720-treated cohorts at treatment day 4 exhibited reduced levels of p-MEK and p-ERK and elevated levels of p27.

comparing PLX4720-treated and vehicle-treated HT-29 xenografts (vehicle: 2.21 ± 0.06 %ID/g, N = 5; PLX4720: 1.97 ± 0.14 %ID/g, N = 5) (**Figure 5.7B**), suggesting that [^{18}F]-FLT PET accurately predicted lack of response. Similarly, no difference in [^{18}F]-FDG uptake was observed between PLX-4720-treated and vehicle-treated HT-29 xenograft bearing mice (**Figure 5.8A**). PLX4720 treatment did not affect relative p-MEK or p-ERK levels in HT-29 xenografts, as determined by Western blot of tumor tissues, harvested immediately following imaging on treatment day 4 (**Figure 5.7C**). Surprisingly, unlike similarly treated Lim2405 xenografts, appreciable levels of PLX4720 were not detected in HT-29 xenografts

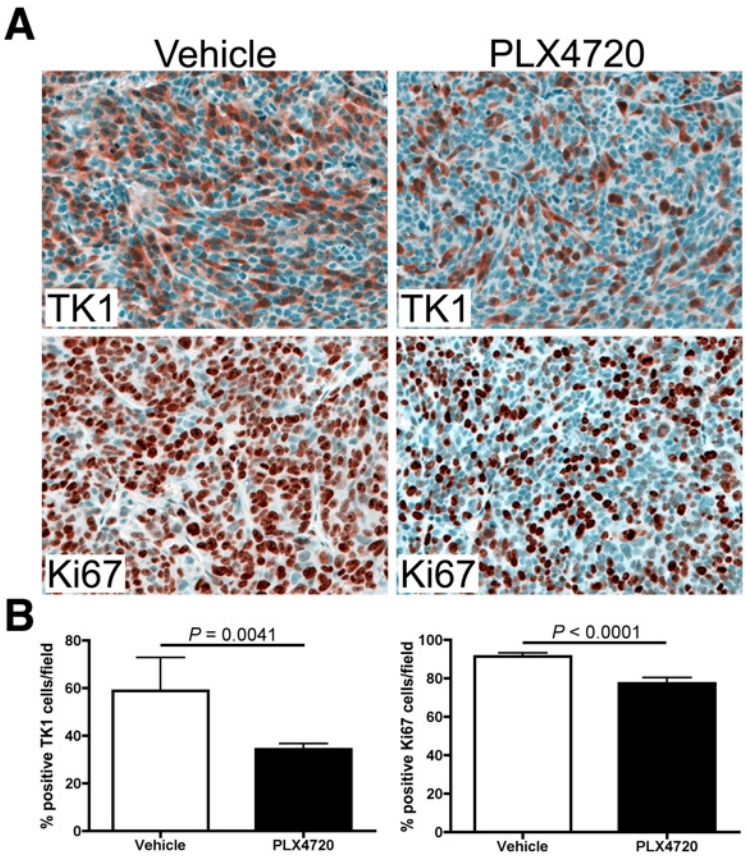

Figure 5.6. Early [^{18}F]-FLT PET agrees with tumor cell TK1 levels and Ki67 immunohistochemistry. Immunohistochemistry analysis of [^{18}F]-FLT PET imaging-matched Lim2045 xenografts (*see **Figure 5.2***). (**A**) Representative TK1 and Ki67 immunohistochemistry images of xenografts harvested at treatment day 4 are shown for both vehicle-treated and PLX720-treated tumors. (**B**) PLX4720-treated xenografts exhibited approximately 25% fewer TK1-positive cells per field compared to vehicle controls (34.3% vs. 58.8%, p = 0.0041). A modest, though statistically significant (p < 0.001), reduction in the number of Ki67 positive cells per field was observed for PLX4720-treated xenografts compared to vehicle controls (77.4% vs. 89.5%).

of treated mice, although drug was detected in adjacent bowel (**Figure 5.7D**). In agreement with [^{18}F]-FLT PET, neither TK1 levels (**Figure 5.8B**) nor Ki67 immunoreactivity (**Figure 5.8C**) were significantly affected by PLX4720 treatment in HT-29 xenografts.

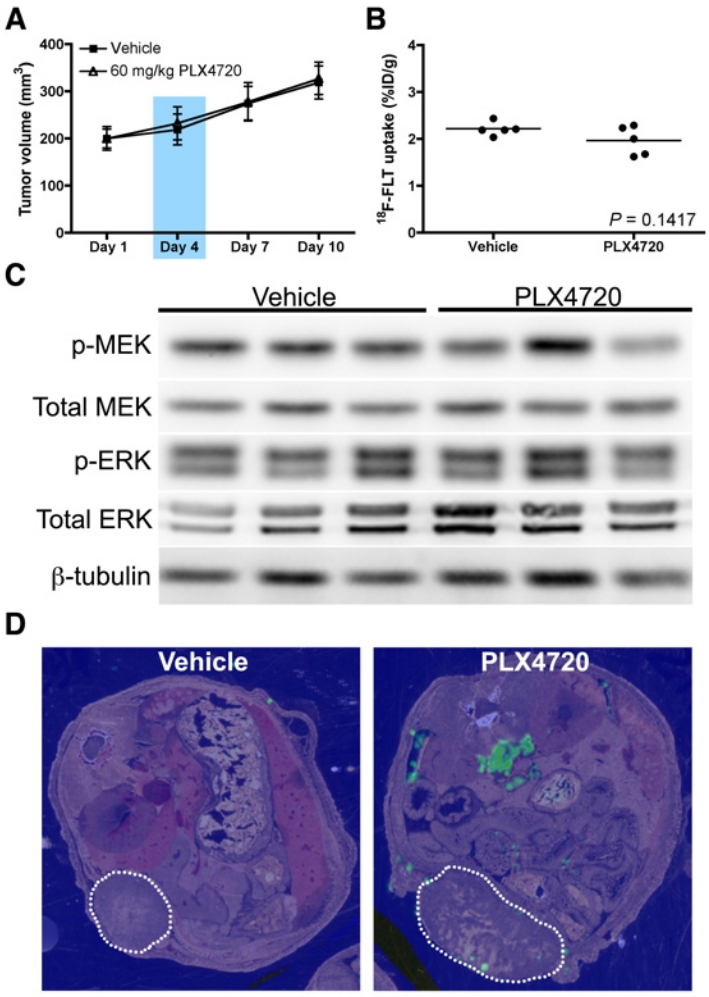

Figure 5.7. [^{18}F]-FLT PET predicts lack of response to PLX4720 in HT-29 xenografts. Mice bearing HT-29 xenografts were treated daily with PLX4720 or vehicle. (**A**) Over a 10 day regimen, no difference in tumor volume was observed between PLX4720-treated and vehicle-treated. Tumor [^{18}F]-FLT PET (**B**) and phosphorylation of BRAF effectors (**C**) were similar between vehicle-treated and PLX4720-treated HT-29 cohorts. (**D**) Representative transverse MALDI IMS pseudocolor maps of ion intensity corresponding to the parent molecular mass of PLX4720 demonstrate minimal signal intensity in vehicle-treated animals. Treated animals demonstrated little PLX4720 ion intensity within tumor tissue (dotted line), yet PLX4720 ion intensity was observed in the bowel.

5. Discussion

Current imaging criteria for evaluating therapeutic response are primarily based upon anatomical response criteria, such as Response Evaluation Criteria

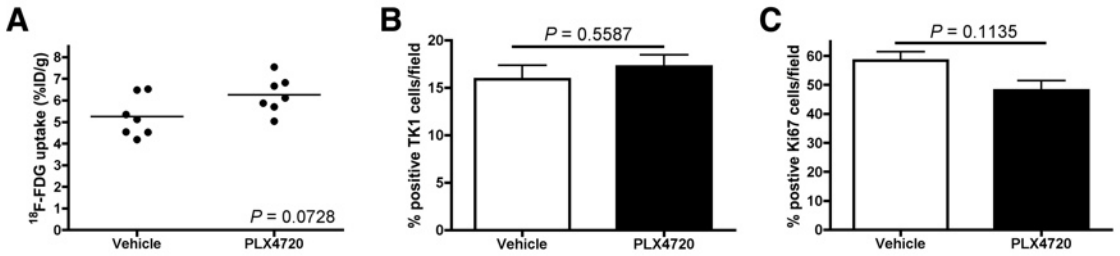

Figure 5.8. [^{18}F]-FDG PET is similar between vehicle-treated and PLX4720-treated HT-29 xenografts and agrees with immunohistochemistry markers of proliferation. (A) Similar to [^{18}F]-FLT PET in HT-29 xenografts, no difference was observed between vehicle-treated and PLX4720-treated HT-29 tumor xenografts using [^{18}F]-FDG PET. Corroborating PET, biochemical, and MALDI results (*see **Figure 5.7***), TK1 (**B**) and Ki67 (**C**) in vehicle-treated and PLX4720-treated HT-29 xenografts exhibited similar immunoreactivity.

in Solid Tumors (RECIST) or similar guidelines. Since relevant cellular and molecular changes may precede changes in size and occur within hours of treatment, RECIST criteria and associated conventional imaging methods may be ill-suited for assessing early responses of tumors to therapy. These limitations have led to the development of newer criteria, such as PERCIST (82) that recognize the potential utility of [^{18}F]-FDG PET to predict early response. For example, [^{18}F]-FDG PET has shown clinical utility to predict response for ^{V600E}BRAF in melanoma (83), although that was not the case in this study which utilizes preclinical models of CRC. A drawback of [^{18}F]-FDG, however, is that its uptake reflects numerous metabolic processes. For this reason, more specific imaging biomarkers of proliferation may be better suited to predict treatment response in certain clinical scenarios (84).

Compared to [^{18}F]-FDG PET, [^{18}F]-FLT PET exhibits increased proliferation specificity (11, 14) and may be a more suitable option in some settings for evaluating response to targeted therapy. Uptake of [^{18}F]-FLT reflects proliferation by reporting the activity of thymidine salvage, a mechanism that provides dividing

cells with DNA precursors from the extracellular environment. Upon internalization, [^{18}F]-FLT is monophosphorylated by the cytosolic enzyme TK1, resulting in intracellular trapping and accumulation (21, 85, 86). *TK1* expression is a product of E2F transcription, which can be activated by MAPK signaling (87). For example, Solit and colleagues reported that [^{18}F]-FLT PET correlated with response to a MEK inhibitor in melanoma xenografts (88). Given this, we hypothesized that [^{18}F]-FLT PET would also be sensitive to ^{V600E}BRAF inhibition in tumors whose proliferation was associated with constitutive MAPK pathway activity.

In this study, we utilized preclinical models of CRC to explore [^{18}F]-FLT PET as a metric to predict response to a ^{V600E}BRAF inhibitor. In a ^{V600E}BRAF-sensitive model, we found that [^{18}F]-FLT PET predicted tumor growth arrest and reduced proliferation associated with attenuation of BRAF downstream effectors. Notably, in the same model [^{18}F]-FDG PET failed to predict drug sensitivity. In another model that exhibited *in vitro* but not *in vivo* sensitivity, [^{18}F]-FLT PET accurately reflected a lack of *in vivo* response that correlated with limited drug exposure in tumor tissue. Through the use of MALDI-IMS, we were able to document that the sensitive model, Lim2405 xenografts, exhibited significantly greater levels PLX4720 in tumor tissue at the time of [^{18}F]-FLT PET than the insensitive model, HT-29 xenografts. Though both models were treated and imaged similarly, we anticipate that differences in vasculature and/or stroma may have contributed to the observed differences in exposure. Regardless, [^{18}F]-FLT PET effectively reflected tumor proliferation in both models.

Other preclinical results have documented the sensitivity of CRC cell lines to ^{V600E}BRAF inhibition, though clinical results evaluating this approach in patients with colon cancer have been less promising (72). Clinically, it remains unclear whether the lack of single agent efficacy in *^{V600E}BRAF* colon tumors stems from resistance, or as with our study, a lack of adequate exposure, or potentially other reasons. A recent preclinical study found that combined BRAF and EGFR inhibition results in improved efficacy in this setting (73). Importantly, since combination therapy led to reduced MAPK activity and proliferation, our results suggest that [^{18}F]-FLT PET represents a potentially superior, quantitative biomarker to evaluate the efficacy of analogous combination regimens in this setting.

6. Conclusion

We utilized preclinical models of CRC to demonstrate [^{18}F]-FLT as a sensitive predictor of response to a ^{V600E}BRAF inhibitor. Since [^{18}F]-FLT PET predicted reduced proliferation associated with attenuation of BRAF downstream effectors, while [^{18}F]-FDG PET did not, we anticipate this imaging metric may represent an alternative to [^{18}F]-FDG PET for quantifying clinical responses to BRAF inhibitors.

CHAPTER 6

[^{18}F]-FLT PET REFLECTS PI3K-mTOR-MEDIATED PRO-SURVIVAL RESPONSE TO TARGETED THERAPY IN COLORECTAL CANCER

1. Abstract

Biomarkers that predict response to targeted therapy in oncology are an essential component of personalized medicine. In preclinical treatment response studies that featured models of wild-type *KRAS* or mutant-*BRAF* colorectal cancer treated with either cetuximab or vemurafenib, respectively, we illustrate that [^{18}F]-FLT PET, a non-invasive molecular imaging readout of thymidine salvage, closely reflects pro-survival responses to targeted therapy that are mediated by PI3K-mTOR activity. Activation of pro-survival mechanisms forms the basis of numerous modes of therapeutic resistance. Therefore, we conclude that [^{18}F]-FLT PET may serve a novel and potentially critical role to predict tumors that exhibit molecular features that reflect recalcitrance to MAPK-targeted therapy in this and potentially other clinically-relevant settings. Though these studies focused on colorectal cancer, we envision that the results may be applicable to other solid tumors as well.

2. Introduction

With increased ability to rapidly and inexpensively characterize the genetic basis of an individual patient's tumor, personalized therapies are rapidly becoming the norm in oncology. Landmark examples of the success of

personalized medicine in oncology include the use of vemurafenib to treat *^{V600E}BRAF* melanoma (67), trastuzumab to treat *HER2* overexpressing breast cancers (89), and imatinib, a Bcr-Abl tyrosine kinase inhibitor, in chronic myelogenous leukemia (90). With an increasing reliance on molecularly targeted therapies, there remains an equally critical challenge to develop and validate specific biomarkers that reflect target inhibition, pathway inactivation, and predict overall clinical response. Most biomarkers utilized in oncology studies require tissue sampling which is highly susceptible to sampling error due and bias from heterogeneity. Analogously, serum-based biomarkers lack the ability to directly visualize the tumor and demonstrate that the measured effect is directly the result of tumor response. Non-invasive imaging circumvents these limitations and offers major advantages over traditional biomarkers. Of the multitude of imaging modalities available clinically, the sensitivity of positron emission tomography (PET) coupled with the ability to readily produce biologically active molecules bearing positron-emitting isotopes makes PET imaging one of the most attractive modalities for detecting tumors and profiling their biological responses to therapy.

Our laboratory has studied the biological basis of 3'-deoxy-3'[18F]-fluorothymidine ([^{18}F]-FLT) accumulation in tumors (25, 26, 91) and other diseased tissue (27). [^{18}F]-FLT was originally developed to serve as a non-invasive measure of cellular proliferation, with obvious utility in oncology studies (10, 14). A thymidine analog, [^{18}F]-FLT serves as a surrogate measure of proliferation by reporting on the activity of thymidine salvage, a pathway that provides DNA precursors to dividing cells. Upon cellular internalization, [^{18}F]-FLT

is monophosphorylated in a reaction catalyzed by the cytosolic enzyme thymidine kinase 1 (TK1) and trapped in the cell. Unlike thymidine, [^{18}F]-FLT is not incorporated into DNA. TK1 activity is closely correlated with DNA synthesis and tends to be diminished in quiescent cells. [^{18}F]-FLT has been widely studied as a marker of treatment response in a spectrum of tumor types and treatments both in the pre-clinical and clinical settings (92). However, it is important to note that unlike more generalizable proliferation markers, such as Ki67, [^{18}F]-FLT PET reflects proliferative indices to variable and potentially unreliable extents. [^{18}F]-FLT PET cannot discriminate moderately proliferative, thymidine salvage-driven tumors from those of highly proliferative tumors that rely primarily upon *de novo* thymidine synthesis. Despite a lack of correlation with proliferation in some circumstances, we envisioned that TK1 levels, and thus [^{18}F]-FLT PET, could reflect other, potentially important molecular events associated with response to therapy.

In this study, using preclinical models of colorectal cancer we demonstrate two unique circumstances where [^{18}F]-FLT PET does not correlate with proliferation but rather reflects pro-survival responses to targeted therapy that are mediated by PI3K-mTOR pathway activity. In these settings, [^{18}F]-FLT PET was discordant with [^{18}F]-FDG PET, the most widely utilized tracer in clinical oncology, which was insensitive to mTOR- or PI3K-pathway activity. Cetuximab-mediated inhibition of MAPK activity in a wild-type *KRAS* cell line model and vemurafenib-mediated inhibition of BRAF in a ^{V600E}*BRAF* mutant cell line model had no effect on [^{18}F]-FLT PET unless PI3K-mTOR was subsequently attenuated

pharmacologically or via genetic silencing. Overall, these studies demonstrate a novel role for [^{18}F]-FLT PET as a means to predict tumors that resist MAPK inhibition through PI3K-mTOR activation in colorectal cancer and potentially other solid tumors.

3. Results

Regulation of TK1 following EGFR blockade in wild-type KRAS colorectal cancer cells

We previously evaluated molecular imaging biomarkers to predict response to cetuximab in preclinical models of colorectal cancer (25). In these studies, we found that imaging readouts of EGFR occupancy and apoptosis predicted response to cetuximab in DiFi cell line xenografts. DiFi cells were isolated from a rectal cancer arising in a patient with familial polyposis express wild-type KRAS and exhibit EGFR amplification (34). Interestingly, [^{18}F]-FLT PET did not predict response in these studies, despite reduced proliferation and subsequent treatment-induced tumor regression (25). Building on these observations, our more recent studies (93) demonstrated that while [^{18}F]-FLT PET accurately reflects TK1 levels, it does not necessarily correlate with standard clinical measures of proliferation, such as Ki67 immunoreactivity. Consequently, in this study, we first sought to elucidate relationships between EGFR blockade with cetuximab and TK1 protein and mRNA levels. Initially, we used cultured DiFi cells to evaluate the temporal relationship between cetuximab exposure and p-ERK, TK1, and p27 protein levels over 24 hours (**Fig. 6.1A**). As

expected, p-ERK levels were almost immediately attenuated, showing a dramatic reduction within the first hour of cetuximab exposure (5.0 μg/mL). Levels of p-ERK remained well-below baseline for up to 24 hours under these conditions. Paradoxically, TK1 protein levels increased following cetuximab exposure, which peaked at 12 hours, and then rapidly declined between 15 and 24 hours to below baseline levels. Protein levels of the cell cycle inhibitor p27 rose dramatically at 12 hours and remain elevated through the end of the time course. In the presence of elevated p27 levels, TK1 levels dropped precipitously to below control levels, implicating p27 as potentially a key determinant of TK1 regulation in DiFi cells responding to cetuximab.

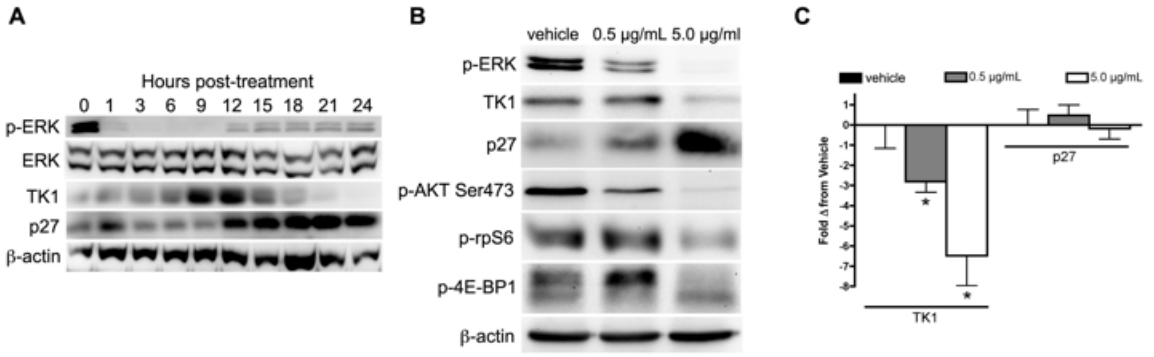

Fig. 6.1. Diminished TK1 protein levels correlate with attenuation of mTOR-PI3K pathway activity and upregulation of p27.(**A**) Western blot of DiFi cell lysates following cetuximab exposure (5 μg/mL) resulted in rapid attenuation of downstream MAPK targets including p-ERK, which remained well-below baseline levels to 24 hours. Paradoxically, TK1 protein levels increased from 1-12 hours until p27 protein levels rise, at which time TK1 fell to fellow baseline. (**B**) DiFi cells treated with either 0.5 μg/mL or 5.0 μg/mL cetuximab resulted in an approximately 50% reduction and full attenuation of p-ERK protein levels, respectively at 24 hours. At 0.5 μg/mL TK1 levels were unaffected despite a modest rise in p27 protein levels. However, 5.0 μg/mL cetuximab resulted in greatly decreased TK1 with a large increase in p27 protein levels. PI3K-mTOR activity, as measured by p-AKT Ser473, p-rpS6, and p-4E-BP1, was either maintained or elevated at 0.5 μg/mL cetuximab but was attenuated at 5.0 μg/mL cetuximab. (**C**) qRT-PCR analysis showed *TK1* mRNA was significantly reduced at 0.5 μg/mL ($p = 0.0279$) and 5.0 μg/mL ($p = 0.0186$), while no change in *p27* mRNA levels was observed at either dose.

To further evaluate the relationships between MAPK pathway inhibition, TK1 regulation, and p27, DiFi cells were exposed to two concentrations (0.5 μg/mL and 5.0 μg/mL) of cetuximab for 24 hours (**Fig. 6.1B**). These levels of cetuximab resulted in attenuation of p-ERK by approximately 50% or nearly 100% at 24 hours. At 0.5 μg/mL, TK1 protein levels were unaffected despite modestly elevated p27 and an approximately 50% reduction of p-AKT Ser473. Conversely, the 5.0 μg/mL level of exposure resulted in TK1 levels that were dramatically attenuated. Similar to the time course study, reduced TK1 correlated with a robust increase in p27. Additionally, a complete attenuation of p-ATK Ser473 was observed at 5.0 μg/mL. In contrast to protein, *TK1 mRNA* tended to follow p-ERK levels more directly (**Fig. 6.1C**), which is not surprising given the dependence of *TK1* on E2F transcription (94), a downstream product of MAPK activity. Interestingly, *p27* mRNA was unaffected by cetuximab exposure, suggesting that the elevated p27 protein levels stemmed from inhibition of downstream targets that affect post-translational modification of p27, with AKT being one of these (95). To determine if TK1 protein levels observed at 0.5 μg/mL levels of exposure were maintained through increased translational efficiency, we measured p-rpS6 and p-4E-BP1 levels, both products of pro-translational PI3K-mTOR activity (**Fig. 6.1B**). We found p-rpS6 levels to be attenuated only at the highest concentration of cetuximab, suggesting a lack of effect on mTOR activity at the 0.5 μg/mL exposure level. Furthermore, p-4E-BP1 levels were elevated at the lower concentration of cetuximab, suggesting increased potential

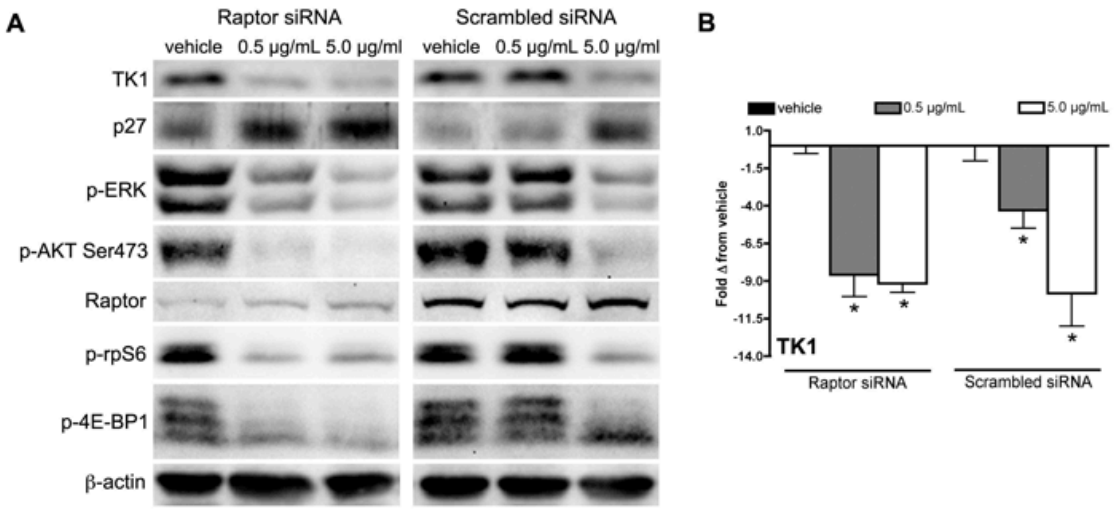

Fig. 6.2. Cetuximab-mediated regulation of TK1 levels require attenuation of PI3K-mTOR signaling. (**A**) Silencing mTORC1 facilitated upregulation of p27 and attenuated TK1 protein levels at 0.5 µg/mL cetuximab without affecting the anti-MAPK activity effects of cetuximab. Levels of p-AKT Ser473, p-rpS6, and p-4E-BP1 were reduced at 0.5 µg/mL cetuximab exposure with Raptor knockdown but not in scrambled siRNA control. (**B**) As evidence of the functionality of the p27 upregulated at the 0.5 µg/mL concentration following Raptor knockdown, TK1 mRNA levels were similarly reduced at 0.5 µg/mL and 5.0 µg/mL with Raptor knockdown.

for translation at the ribosomal cap (96). Conversely, Both p-rpS6 and p-4E-BP1 were attenuated at the higher level of cetuximab exposure. Taken together with *TK1* mRNA levels, these results provided evidence for increased translational efficiency of TK1 at the lower level of cetuximab exposure that appear to proceed through mTOR activation.

Silencing mTOR-PI3K activity facilitates cetuximab-mediated attenuation of TK1 levels in DiFi cells

To explore the role of mTOR on TK1 regulation in cetuximab-treated DiFi cells, we silenced mTOR activity using an siRNA to Raptor, an essential member of the mTOR Complex 1 (mTORC1) (97). Notably, in the absence of mTORC1 activity, TK1 protein levels were attenuated at both 0.5 µg/mL and 5.0 µg/mL

concentrations of cetuximab, without an obvious effect on MAPK pathway activity (**Fig. 6.2A**). As expected, Raptor silencing resulted in attenuation of p-AKT Ser473 and p-rpS6 as well as blocking phosphorylation of 4E-BP1. In addition to attenuated TK1 protein levels, another important effect of mTORC1 inactivation was a marked increase in p27 protein levels, which appeared to be at least partially responsible for *TK1* transcriptional control at the lowest level of cetuximab exposure (**Fig. 6.2B**). Interestingly, as observed previously, the rise in p27 protein levels was itself not a product of transcription as *p27 mRNA* was not elevated at either concentration of cetuximab (**Fig. 6.3**). These results suggest that mTOR activation imparts its effect on TK1 through downstream effectors such as AKT through post-translational modification and degradation of cell cycle inhibitors, including p27 (95). As evidence of this, mTORC1 inhibition in conjunction with EGFR blockade led to a profound reduction of TK1 protein

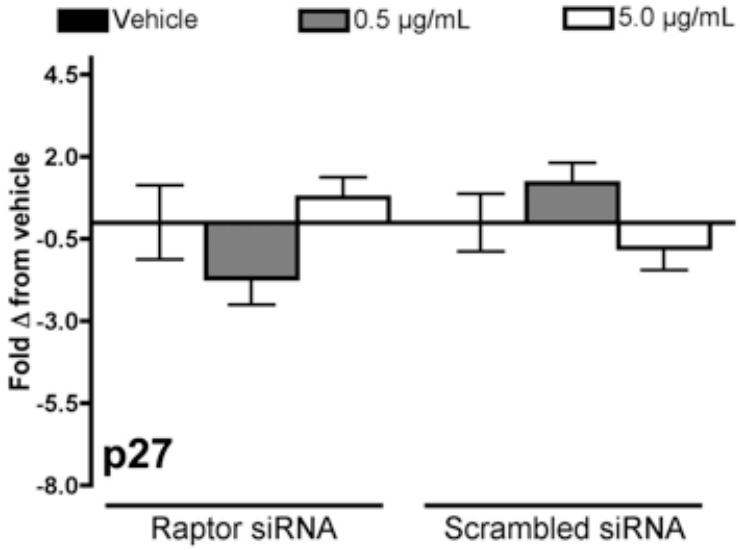

Fig. 6.3. **Elevated p27 protein levels are observed following cetuximab exposure in DiFi cells are not transcriptionally induced.** No statistically significant change in p27 was observed in DiFi cells treated with raptor siRNA or scrambled RNA when treated with either 0.5 µg/mL or 5.0 µg/mL cetuximab.

levels not observable with cetuximab exposure alone at the lower concentration.

[^{18}F]-FLT PET reflects inhibition of PI3K-mTOR activity in cetuximab-treated DiFi cell line xenografts in vivo

To study the effects of PI3K-mTOR activity on TK1 and [^{18}F]-FLT PET *in vivo*, we subsequently imaged DiFi xenograft-bearing mice with [^{18}F]-FLT PET following treatment at two levels of cetuximab exposure (20 mg/kg or 40 mg/kg) or vehicle. Analogous to our previous studies (25), similar [^{18}F]-FLT accumulation was observed in xenografts treated with vehicle or 20 mg/kg cetuximab. Conversely, increasing the treatment dosage of cetuximab to 40 mg/kg resulted in diminished [^{18}F]-FLT accumulation in DiFi xenografts (**Fig. 6.4A**). Western blot analysis of xenograft tissue harvested immediately following imaging confirmed diminished TK1 protein levels at the 40 mg/kg dosage relative to vehicle-treated and mice treated with 20 mg/kg cetuximab (**Fig. 6.4B**). Similar to *in vitro* studies, diminished TK1 protein levels correlated with elevated p27 protein levels, but not *p27* mRNA levels (**Fig. 6.5**). Also similar to *in vitro* studies, TK1 protein levels were unaffected by the lower dosage of cetuximab, despite significantly reduced *TK1* mRNA at both levels of cetuximab exposure (**Fig. 6.4C**). Immunohistochemistry of imaging-matched xenograft tissues illustrated that PI3K-mTOR activity, as measured by p-AKT Ser473 and p-rpS6 levels, were only inhibited at the highest cetuximab exposure (**Fig. 6.4D**). Interestingly, Ki67 was reduced at both levels of cetuximab exposure (**Fig 6.4D, Fig. 6.6**), suggesting that [^{18}F]-FLT PET was decoupled from standard measures of proliferation as we

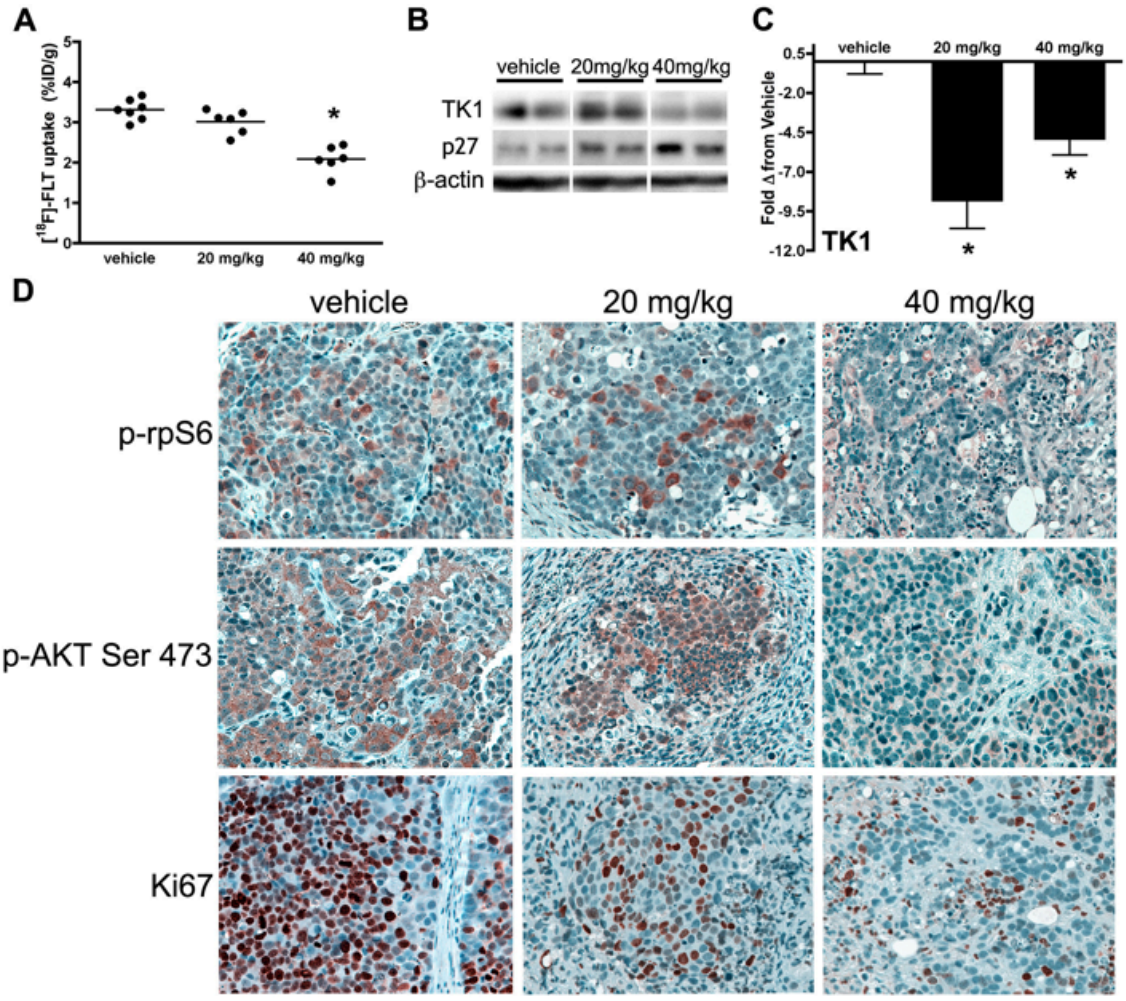

Fig. 6.4. [^{18}F]-FLT PET reflects inhibition of PI3K-mTOR activity in cetuximab-treated DiFi xenografts. DiFi tumor xenografts were imaged on day 7 of 20 mg/kg or 40 mg/kg cetuximab treatment regimens. (**A**) [^{18}F]-FLT PET was only reduced in DiFi xenografts treated at the 40 mg/kg level ($p = 0.0012$). (**B**) Western blot analysis of tissues harvested immediately after imaging confirmed that TK1 protein levels were only decreased at the 40 mg/kg dose level. Greatly increased p27 protein levels were observed at the 40 mg/kg dose levels. (**C**) Similar to *in vitro* observations, TK1 mRNA was significantly reduced at both 20 mg/kg ($p = 0.0003$) and 40 mg/kg ($p = 0.0339$) dose levels. (**D**) IHC analysis of p-rpS6 and p-AKT Ser473 showed little change in staining at 20 mg/kg, however both markers were greatly reduced at 40 mg/kg. Ki67 IHC was reduced at both levels of cetuximab exposure.

have previously reported (93). While [^{18}F]-FLT PET appeared to be sensitive to the PI3K-mTOR activity in that [^{18}F]-FLT uptake was only reduced when these targets were inhibited, [^{18}F]-FDG PET imaging was not sensitive to this

Fig. 6.5. Cetuximab-dependent p27 protein induction is not a result of transcriptional activity. No statistically significant change in p27 levels was observed in DiFi xenografts treated with either 20 mg/kg or 40 mg/kg cetuximab relative to vehicle-treated xenografts

phenomenon. For example, we observed that [^{18}F]-FDG uptake was reduced relative to vehicle controls at both levels of cetuximab exposure (**Fig. 6.7**). Overall, these results suggest that the biological readouts of proliferation provided by [^{18}F]-FLT PET are unique and not necessarily captured by [^{18}F]-FDG PET or standard measures of proliferation.

TK1 protein levels do not reflect ^{V600E}BRAF inhibition in COLO 205 cells

Analogous to the DiFi model treated with cetuximab, we evaluated relationships between target inhibition, inhibition of downstream effector molecules, and TK1 levels in a ^{V600E}BRAF-expressing colon cancer cell line treated with selective inhibition of ^{V600E}BRAF (**Fig. 6.8**). PLX4032 exposure for 48 hours led to a concentration-dependent inhibition of p-MEK levels. Paradoxically,

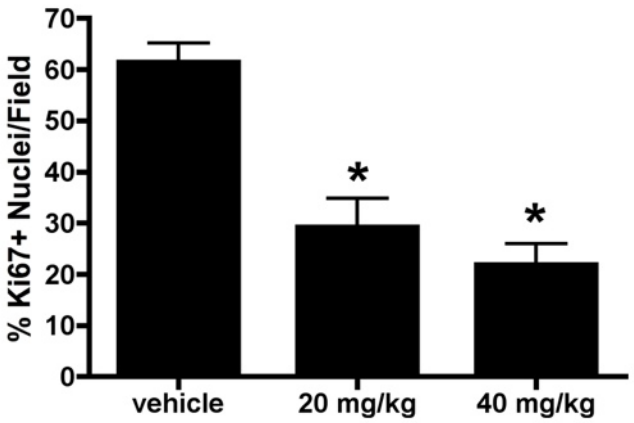

Fig. 6.6. [^{18}F]-FLT PET in cetuximab-treated DiFi xenografts reflects Ki67 immunoreactivity only when PI3K-mTOR signaling was attenuated. Ki67 IHC was reduced at both 20 mg/kg ($p = 0.0028$) and 40 mg/kg ($p = 0.0004$) cetuximab.

p-ERK levels were increased in a concentration-dependent manner, except at the highest dose (5 μM) (**Fig. 6.8A**). The mismatch between p-MEK and p-ERK was not observed at exposure durations of 2 hours (**Fig. 6.9**) or 24 hours (**Fig. 6.10**). While p-AKT Ser473 levels were only moderately reduced with PLX4032 exposure at 48 hours, we observed a PLX4032 concentration-dependent increase in p-rpS6 that correlated with the increase in p-ERK. Analogously, concomitantly increased p-rpS6 and diminished DUSP6 levels suggested that the increase in p-ERK was at least partially the result of diminished phosphatase activity associated with mTOR activation (98). PLX4032 exposure had only a modest effect on p27 levels, which were elevated in a concentration-dependent manner, though slightly. TK1 levels were increased slightly at modest PLX4032 concentrations and similar to vehicle at higher levels of exposure, except for the highest concentration (5 μM). Surprisingly, *TK1* mRNA levels appeared to be

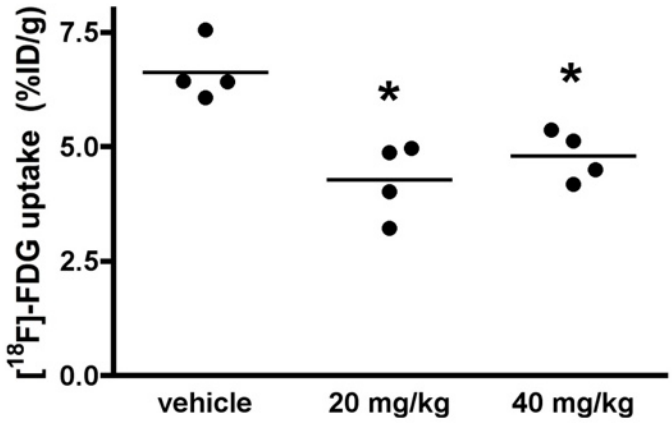

Fig. 6.7. [^{18}F]-FDG PET does not reflect inhibition of PI3K-mTOR signaling in cetuximab-treated DiFi xenografts DiFi tumor xenografts were imaged on day 7 of a 20 mg/kg or 40 mg/kg cetuximab treatment regimen. [^{18}F]-FDG PET was reduced at both the 20 mg/kg ($p = 0.0286$) and 40 mg/kg ($p = 0.0286$) dose levels.

closely associated with inhibition of p-MEK and, unlike TK1 protein levels, were reduced in an essentially concentration-dependent manner (**Fig. 6.8B**).

[^{18}F]-FLT PET, but not [^{18}F]-FDG PET, reflects elevated mTOR activity and correlates with a lack of p-ERK inhibition in PLX4720-treated COLO 205 xenografts

To evaluate the relationship between [^{18}F]-FLT PET and downstream BRAF effectors following PLX4720 exposure *in vivo*, mice bearing COLO 205 xenografts were treated daily with 60 mg/kg PLX4720 for 4 days imaged with [^{18}F]-FLT PET or [^{18}F]-FDG PET (**Fig. 6.11**). In agreement with *in vitro* studies showing that BRAF inhibition had little effect on TK1 levels in COLO 205 cells, treatment with PLX4720 had little effect on [^{18}F]-FLT PET imaging. Conversely, [^{18}F]-FDG PET was dramatically reduced in similarly treated cohorts (**Fig. 6.11B)**.

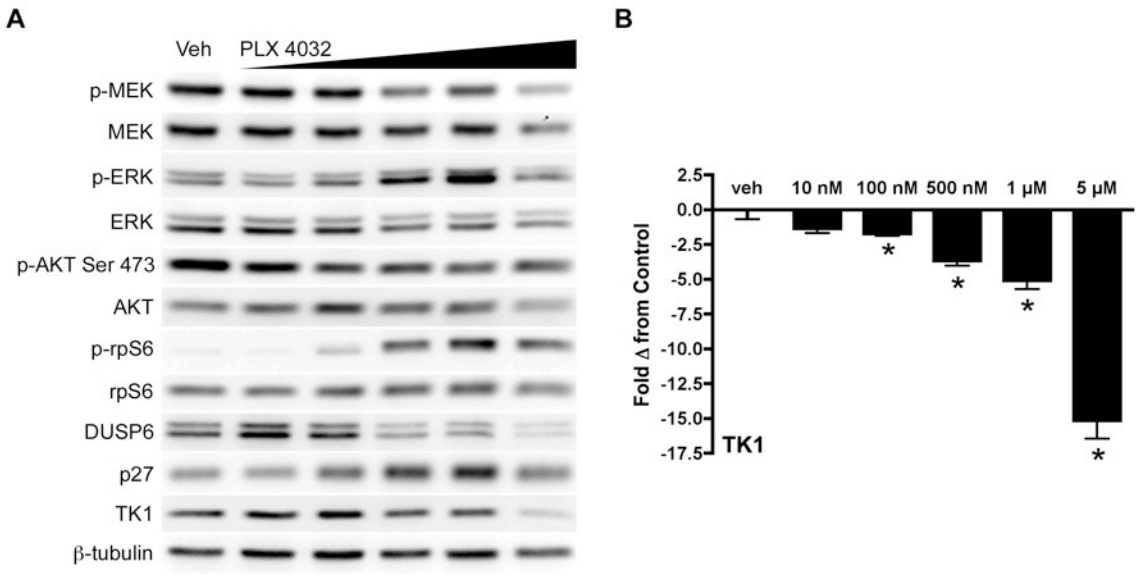

Fig. 6.8. **TK1 protein levels do not reflect p-ERK attenuation following inhibition of ^{V600E}EBRAF inhibition in COLO 205 cells.** COLO 205 cells were collected 48 hours of PLX4032 exposure at 10nM, 100nM, 500 nM, 1 μM, or 5μM. (**A**) Western blot analysis demonstrated target inhibition of p-MEK, however, an increase in p-ERK levels. PI3K and mTOR signaling were maintained as measured by maintenance of p-AKT Ser473 and a concentration-dependent increase in p-rpS6. The ERK-phosphatase DUSP6 increased in conjunction with mTOR signaling and was inversely proportional to p-ERK levels. Slight p27 induction was observed, and no change in TK1 levels was observed except at the highest dose. (**B**) Decreased *TK1* mRNA levels were observed at all drug concentrations above 10nM ($p < 0.05$).

In agreement with imaging, TK1 levels of PLX4720-treated xenografts were similar to vehicle-treated controls. Also similar to *in vitro* studies, we found elevated p-ERK levels and p-rpS6 levels in PLX4720-treated xenografts relative to vehicle-treated controls, despite inhibition of the BRAF effector, p-MEK.

mTORC1/mTORC2 regulation of TK1 in PLX4032-treated COLO 205 cells

To examine mTOR's role in TK1 regulation following ^{V600E}BRAF inhibition, cultured COLO 205 cells were treated concomitantly with 250nM PP242, a selective mTORC1/mTORC2 inhibitor (99) and increasing concentrations of PLX4032 for 48 hours (**Fig. 6.12**). We found that PP242 had little effect on

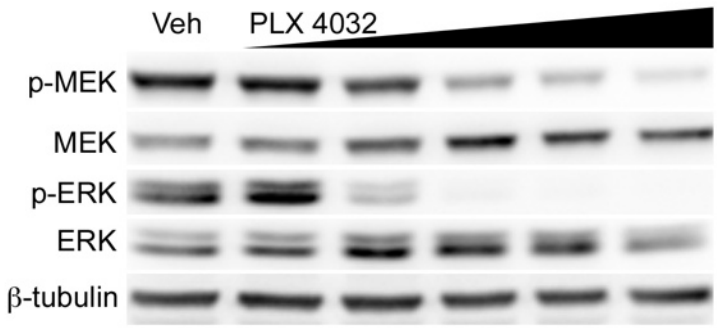

Fig. 6.9. Inhibition of MAPK-pathway activity in COLO 205 cells following exposure to PLX4032 for 2 hours. ^{V600E}BRAF downstream effectors p-MEK and p-ERK were similarly inhibited following 2 hours PLX4032 exposure.

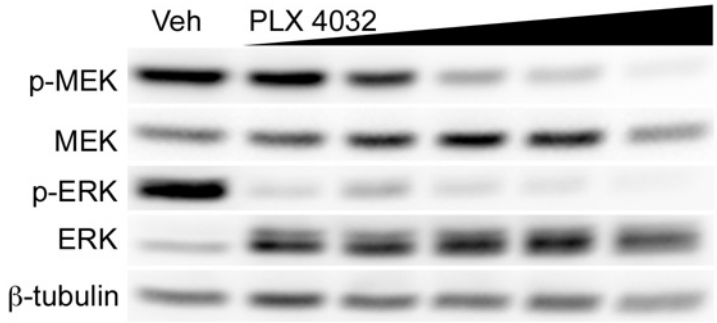

Fig. 6.10. Relative inhibition of ^{V600E}BRAF downstream effectors following 24 hours exposure of COLO 205 cells to PLX4302. COLO 205 cells were collected at 24 hours following treatment with 10 nM, 100 nM, 500 nM, 1 μM, or 5 μM PLX4032.

PLX4032-dependent inhibition of p-MEK, yet effectively blocked activation of p-AKT at Ser473 and blunted the previously observed activation of p-rpS6 caused by PLX4032 exposure (see **Fig. 6.8A**). However, mTOR blockade was insufficient to attenuate p-ERK levels in a PLX4032-dependent manner, nor to completely attenuate p-rpS6 levels (**Fig. 6.12A**). As with single agent *in vitro* studies, p-rpS6 activation correlated with a slight attenuation of DUSP6 levels and a slight elevation of p-ERK at higher PLX4032 concentrations. Nonetheless, combined inhibition of p-AKT Ser473 and p-MEK resulted in dramatically decreased TK1, at both the protein and mRNA level. In the presence of elevated p27, *TK1* mRNA levels fell dramatically, with significant reductions observed at

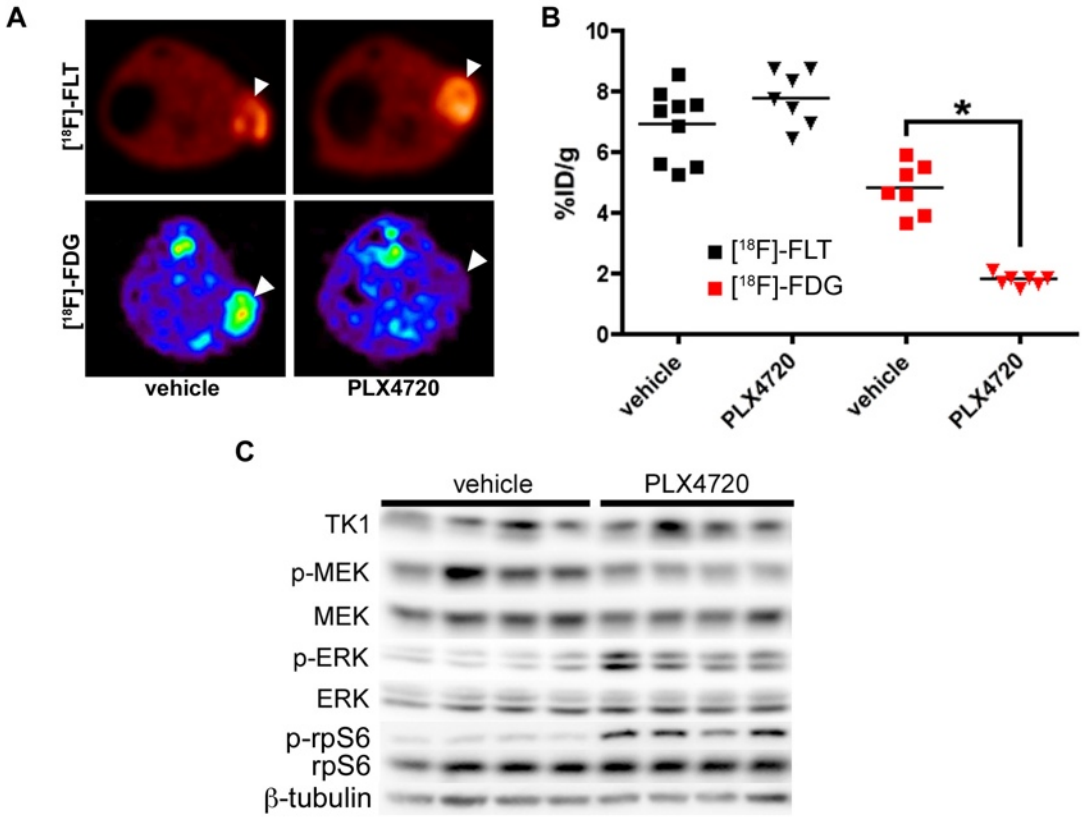

Fig. 6.11. PLX4720 exposure does not affect [^{18}F]-FLT PET in COLO 205 xenografts despite evidence of target inhibition and diminished [^{18}F]-FDG uptake. (**A**) Representative transverse [^{18}F]-FLT and [^{18}F]-FDG PET images acquired after three daily treatments with vehicle or 60 mg/kg PLX4720 (tumor indicated by arrowhead). (**B**) Quantification of PET data illustrated similar [^{18}F]-FLT uptake in vehicle-treated and PLX4720-treated tumors. Unlike [^{18}F]-FLT PET, PLX4720 exposure elicited a significant reduction in [^{18}F]-FDG uptake ($p = 0.0006$) (**C**) Western blot analysis of vehicle- and PLX4720-treated tumor tissue confirmed that PLX4720 had no effect on TK1 protein levels in agreement with [^{18}F]-FLT PET. Target inhibition, as measured by p-MEK levels, was observed. However, similar to *in vitro* studies, PLX4720-treated COLO 205 xenografts exhibited elevated p-ERK and p-rpS6 protein levels relative to vehicle controls.

PLX4032 concentrations as low as 10 nM (**Fig. 6.12B**). Furthermore, suggesting that p-AKT activity was responsible for post-translational modification and degradation of p27, in the presence of p-AKT Ser473 inhibition, p27 protein was dramatically elevated but *p27* mRNA was not (**Fig. 6.12C**).

Regulation of TK1 following dual PI3K-mTOR inhibition and ^{V600E}BRAF inhibition

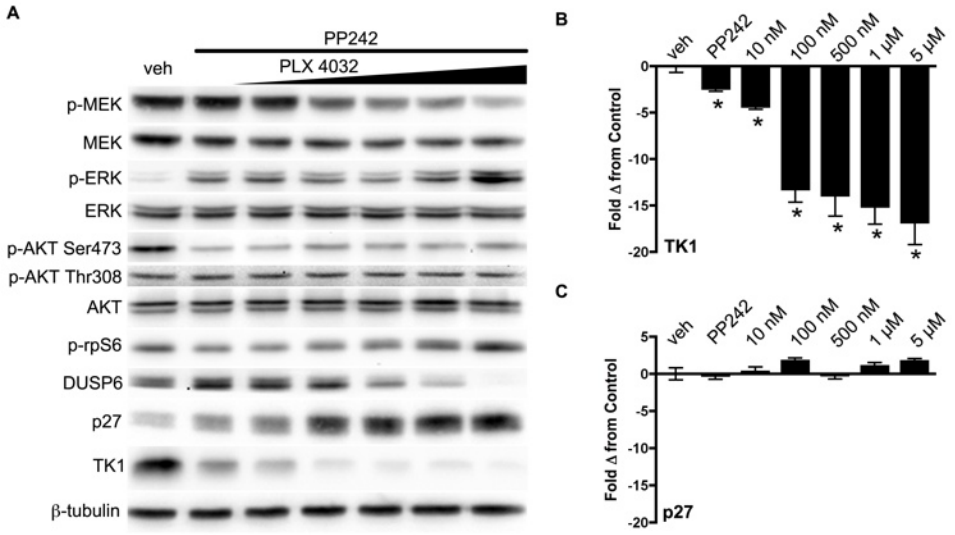

Fig. 6.12. Combined ^{V600E}BRAF and mTOR inhibition results in transcriptional control of TK1 protein levels in COLO 205 cells. (**A**) Western blot of COLO 205 cells treated with PP242 (250 nM) and increasing PLX4032. Similar to single agent PLX4032, p-MEK, but not p-ERK, was inhibited in a PLX4032-dependent manner. Consistent with mTORC1/mTORC2 inhibition, p-AKT Ser473, but not p-AKT Thr308, was inhibited. Unlike single agent PLX4032, which resulted in concentration-dependent activation of p-rpS6, combined treatment maintained p-rpS6 levels at essentially baseline levels except at the highest PLX4032 concentration. Similarly, DUSP6 levels were inversely related to p-ERK protein levels. With combined mTOR and ^{V600E}BRAF blockade, p27 and TK1 protein levels were inversely correlated and dramatically affected by PLX4032 exposure. (**B**) Similarly, *TK1* mRNA was significantly reduced at PLX4032 concentrations as low as 10 nM. (**C**) Despite elevated p27 protein levels, *p27* mRNA was unaffected by combined mTOR-^{V600E}BRAF inhibition.

Given that combined ^{V600E}BRAF-mTOR inhibition was insufficient to attenuate p-rpS6 (see **Fig. 6.12**), and coupled with the observation that PI3K activity has been proposed as a mechanism of resistance to BRAF inhibition in colorectal cancer (100) and melanoma (101, 102), we evaluated the effects of dual PI3K-mTOR inhibition in COLO 205 cells in conjunction with ^{V600E}BRAF inhibition (**Fig. 6.13**). COLO 205 cells were treated with either PLX4032, BEZ235, a small molecule dual inhibitor of PI3K and mTOR (103), or the combination for 24 hours. Indeed, inhibiting both mTOR activity, as measured by p-AKT Ser473, and PI3K activity, as measured by p-AKT Thr308, in the presence

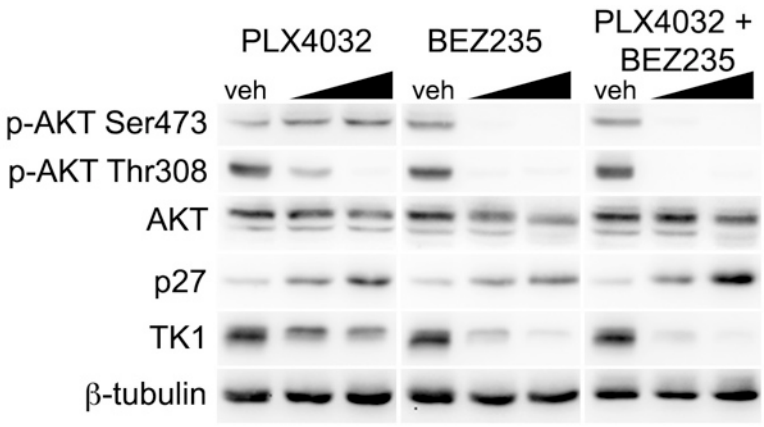

Fig. 6.13. Combined ^{V600E}BRAF and dual PI3K/mTOR inhibition effectively regulates TK1 protein levels and results in greater p27 protein levels than single agents alone. Single agent PLX4032 resulted in activation of p-AKT Ser473 following 24 hours of exposure at two concentrations (100 nM, 1 μM). The addition of the dual PI3K/mTOR inhibitor BEZ235 blocks p-AKT Ser473 activation and resulted in a greater increase in p27 protein levels and diminished TK1 protein levels.

of PLX4032 resulted in greater p27 protein levels and decreased TK1 protein levels. These results prompted our evaluation of this combination *in vivo*.

[^{18}F]-FLT PET reflects inhibition of PI3K-mTOR activity in PLX4720-treated xenografts

To explore the effects of dual PI3K-mTOR inhibition on [^{18}F]-FLT PET in PLX4720-treated COLO205 xenografts *in vivo*, we treated xenograft-bearing mice daily with either vehicle, PLX4720, BEZ235, or in combination, and imaged the mice on treatment day 4. Strikingly, only the combination cohort exhibited decreased [^{18}F]-FLT PET relative to vehicle-treated controls or single agent-treated cohorts (**Fig. 6.14A**). Western blot analysis of imaging-matched xenograft tissue revealed the anticipated increase of p-ERK levels and p-rpS6 levels in PLX4720-treated mice previously observed in our *in vitro* studies (**Fig. 6.14B**).

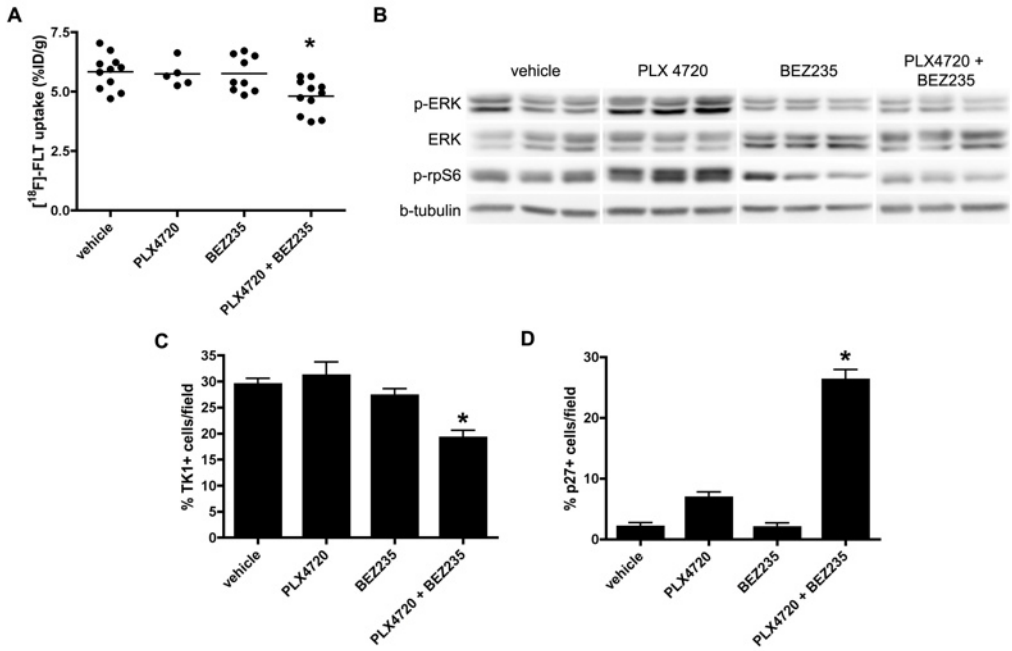

Fig. 6.14. [^{18}F]-FLT PET reflects BEZ235-dependent inhibition of PI3K/mTOR activity in PLX4720 treated COLO 205 xenografts. Xenograft-bearing mice were imaged with [^{18}F]-FLT PET on treatment day 4. (**A**) [^{18}F]-FLT uptake was diminished in the combination treatment cohort relative to vehicle ($p = 0.0087$) or single agent PLX4720- ($p = 0.0174$) or BEZ235- ($p = 0.0403$) treated cohorts. (**B**) Western blot of xenograft tissue harvested immediately following imaging illustrated elevated p-ERK and p-rpS6 levels in PLX4720-treated mice. Combining PLX4032 with BEZ235 resulted in reduced p-ERK and p-rpS6 protein levels. (**C**) TK1 levels, as measured by immunoreactivity, were reduced only in the combination treatment group in agreement with [^{18}F]-FLT PET. (**D**) Consistent with *in vitro* studies, diminished TK1 levels, and consequently [^{18}F]-FLT PET, correlated with elevated p27 that was elevated only in the combination treated group, as measured by immunoreactivity.

However, combination treatment with PLX4720 and BEZ235 led to an overall reduction of p-ERK levels and p-rpS6 levels compared to vehicle-treated controls. In agreement with imaging, TK1 protein levels were reduced in the combination group only (**Fig. 6.14C**), although Ki67 immunoreactivity was reduced for all treatment groups relative to the vehicle-treated cohort (**Fig. 6.15**). In further agreement with *in vitro* studies, combination treatment led to a significant increase in p27 protein levels, but not mRNA levels, compared to vehicle and single agent cohorts (**Fig. 6.14D**, **Fig. 6.16**). These results suggest

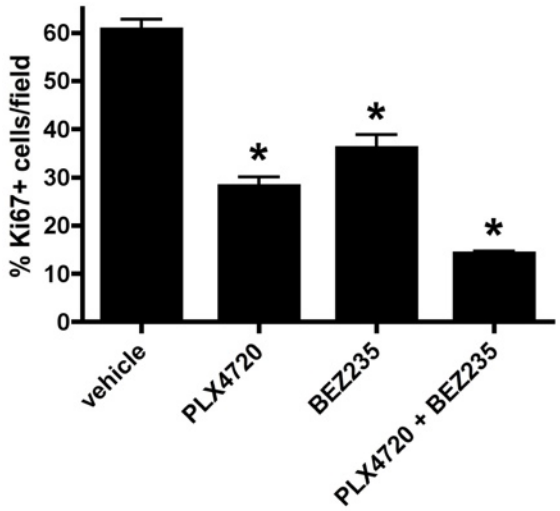

Fig. 6.15. Unlike [^{18}F]-FLT PET, Ki67 immunoreactivity is reduced in COLO 205 xenografts treated with PLX4720 and BEZ235 alone, as well as the combination. Ki67 immunostaining was significantly reduced in all treatment regimens in COLO 205 xenografts ($p < 0.0001$) compared to vehicle-treated xenografts.

that the primary determinant of reduced [^{18}F]-FLT PET in this setting was elevated p27, which was the result of combining blockade of ^{V600E}BRAF and PI3K-mTOR activity.

4. Discussion

Imaging biomarkers to both predict early response to targeted therapy as well as to predict resistance to treatment response are essential components of personalized medicine in oncology. Current clinical means of assessing treatment response by imaging are based upon the Response Evaluation Criteria in Solid Tumors (RECIST) guidelines (1). These criteria are solely based upon changes in tumor size, and do not take advantage of cellular and molecular information now available through contemporary imaging methodologies. Importantly, as cellular and molecular changes can occur within hours of treatment and may precede changes in tumor volume, the RECIST criteria are frequently inadequate

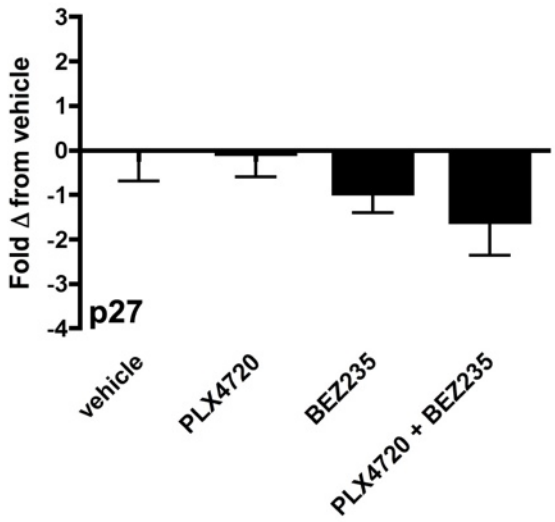

Fig. 6.16. *p27* mRNA is not affected by PLX4720 and BEZ235 alone, or combination treatment in COLO 205 xenograft tumors. No change in *p27* mRNA levels was observed in any treatment regimen compared to vehicle-treated xenografts.

for assessing early tumor response to targeted therapy. These limitations led to the development of newer criteria, such as PERCIST (82), which recognize the potential utility of [^{18}F]-FDG PET to predict early response. However, as [^{18}F]-FDG uptake in tissue reflects a broad range of metabolic processes, including inflammation, a more specific marker of cellular proliferation may better assess treatment response in targeted therapy (84). Notably [^{18}F]-FDG PET was not able to predict activation of PI3K-mTOR signaling in this study.

[^{18}F]-FLT, a thymidine analog, serves as a surrogate marker of proliferation by reporting on the activity of the thymidine salvage pathway, which provides DNA precursors to dividing cells. Since its first use as an imaging probe (14), [^{18}F]-FLT has been extensively studied in small animal models of treatment response and in clinical trials. While many studies, including our own, have shown [^{18}F]-FLT to be sensitive to treatment efficacy (26, 91), others have failed to show changes in [^{18}F]-FLT tumor uptake despite effective treatment (25, 104).

We have extensively investigated the relationship between [^{18}F]-FLT PET and proliferation, and have shown that [^{18}F]-FLT PET does not necessarily reflect proliferation (93), and [^{18}F]-FLT PET may be sensitive to important cellular processes such as activation of signaling pathways, as we demonstrate in this study.

In the context of EGFR inhibition in a wild-type *KRAS* colorectal cancer cell line, we show that a lack of TK1 attenuation, and thus similar [^{18}F]-FLT PET, in treated xenografts predicted PI3K-mTOR activity. Importantly, [^{18}F]-FLT PET in these settings did not reflect target inhibition and thus an additional biomarker to evaluate pharmacodynamic response could potentially be required in the setting of resistance. When mTOR activity was abrogated, by either genetically silencing mTORC1 or sufficiently increasing the dose of cetuximab, TK1 levels were regulated, which, in turn, lead to decreased [^{18}F]-FLT PET. In this study, [^{18}F]-FLT PET provides clinically important information that is unavailable through [^{18}F]-FDG PET imaging, indicating that a tumor that may resist cetuximab treatment through mTOR-mediated mechanisms that may necessitate a change in treatment wither through increased dosage or the targeting of other signaling pathways. We further studied this phenomenon in a different therapeutic setting, the inhibition of ^{V600E}BRAF in a ^{V600E}BRAF mutant colorectal cancer cell line. While inhibition of mTOR signaling in EGFR blockade in wild-type KRAS was sufficient to control TK1, both the PI3K and mTOR pathways served to maintain TK1 protein levels by transcriptional and post-translational mechanisms during pro-survival signaling during ^{V600E}BRAF inhibition. As such, [^{18}F]-FLT PET may

aid the elucidation of the mechanisms of resistance to targeted therapies which are relevant in colorectal cancer (73), and potentially other solid tumors such as melanoma (71).

Clinically, many tumors may initially respond to targeted therapy only to recur with more aggressive phenotypes, notably after ^{V600E}BRAF inhibition in melanoma (71, 105, 106). It is therefore clinically important to detect activation of resistance pathways that may predict future recurrence. This is the first study to demonstrate that [^{18}F]-FLT can serve as an early PET biomarker of pro-survival signaling. It is notable that [^{18}F]-FDG PET was insufficient to observe the activity of the pro-survival signals detected by [^{18}F]-FLT PET. Therefore, we envision a new role for [^{18}F]-FLT PET in the setting of predicting response to targeted therapy.

5. Materials and Methods

Cell lines and mouse models

All studies were approved by the Vanderbilt University Institutional Animal Care and Use Committee and all efforts were made to minimize animal suffering. DiFi human cells were a gift from from Dr. Bruce Borman (34) and COLO 205 cells were obtained from ATCC (CCL-222). DiFi human colorectal cancer cells were grown in Dulbecco's modified Eagle's medium, DMEM, and COLO 205 cells were grown in RPMI (Cellgro) with 10% fetal bovine serum, (Atlanta Biologicals), 1% penicillin and streptomycin (GIBCO) at 37°C and 5% CO_2. Cetuximab was obtained from the Vanderbilt Pharmacy, PLX4032 and PLX4720 were

synthesized as described (75), PP242 was obtained from Sigma Aldrich, and BEZ235 from Selleck Chem. Stock solutions of each drug were prepared and aliquoted to achieve final drug concentrations for *in vitro* studies.

For *in vivo* studies, cell line xenografts were generated in athymic nude mice (Harlan) as described (25) and treatment began when tumor volume reached approximately 150 mm^3. For treatment of DiFi xenografts, saline vehicle, 20 mg/kg, or 40 mg/kg cetuximab were administered i.p. every third day. PET imaging of DiFi xenograft bearing mice was conducted 7 days after the initiation of treatment, 24 hours following the third treatment. For COLO 205 xenografts, mice were treated with DMSO vehicle, 60 mg/kg PLX4720, or 40 mg/kg BEZ235 daily by oral gavage (100 µL total volume). PET imaging of COLO 205 xenograft-bearing mice was conducted 4 days after the initiation of treatment, approximately 24 hours following the third treatment.

siRNA methods

Raptor and random sequence siRNA reagents were obtained from Thermo Scientific. siRNA knockdown was performed as per manufacturer's instructions. In short, 500,000 DiFi cells were plated into each well of a 6-well plate. After 24 hours, siRNA was added to the appropriate wells. After 48 hours, saline vehicle, 0.5 µg/mL or 5.0 µg/mL cetuximab were added to the appropriate wells. After a further 24 hours, cells were harvested for western blotting and qRT-PCR as described below.

Radiopharmaceutical synthesis

[^{18}F]-FLT was prepared in a two-step, one-pot reaction as described (26, 29). [^{18}F]-FLT was obtained with average radiochemical purity of 98.3% and specific activity ≥ 345.5 TBq/mmol. [^{18}F]-FDG was synthesized in the Vanderbilt University Medical Center Radiopharmacy and distributed by PETNET. The average radiochemical purity of the product was 98.5% and specific activity was more than 37 TBq/mmol.

Small-animal imaging

Small-animal PET imaging was performed using a dedicated microPET scanner (Concorde Microsystems Focus 220). Mice were maintained under 2% isoflurane anesthesia in 100% oxygen at 2 L/min and kept warm via a circulating water heating pad for the duration of the PET scan. For [^{18}F]-FLT animals were administered 7.4-9.3 MBq (200-250 μCi) intravenously. Animals were allowed free access to food and water during a 40 minute uptake period, followed by anesthetization and a 20 minute image acquisition. For [^{18}F]-FDG, mice were fasted for approximately 6 hours prior to imaging and warmed in a heated (31º C) chamber for 1 h prior to [^{18}F]-FDG injection and during the uptake period to minimize brown fat uptake of [^{18}F]-FDG. Mice were administered 7.4-9.3 MBq of [^{18}F]-FDG intravenously and allowed free access to water during a 50 minute uptake period followed by a 10 minute PET acquisition.

PET data were reconstructed using OSEM3D/MAP. The resulting three-dimensional reconstructions had an x-y voxel size of 0.474 mm and inter-slice distance of 0.796 mm. ASIPro software (Siemens) was used to manually draw

three-dimensional regions of interest in the tumor volume. Tumor samples were immediately collected following [^{18}F]-FLT PET and flash frozen in liquid nitrogen. [^{18}F]-FLT uptake was quantified as the percentage of the injected dose per gram of tissue (%ID/g) by dividing the ROI activity by the injected dose and multiplying by 100.

Immunoblotting

Prior to resolution by electrophoresis, 20-40 µg of protein from each sample was loaded into 7.5-12% SDS PAGE gels and transferred to PVDF membranes (PerkinElmer). Membranes were blocked overnight at 4°C in tris-buffered saline 0.1% Tween-20 (TBST) containing 5% w/v nonfat dry milk powder. Subsequently, membranes were interrogated with antibodies obtained from Cell Signaling Technology unless noted to p-ERK 1/2 Thr202/Tyr204 (#4370), ERK 1/2 (#4372), TK1 (Abcam, #57757), p27 (#3686), p-AKT Ser473 (#4060), p-AKT Thr308 (#4056), AKT (#4685), p-rpS6 Ser236/236 (#4858), rpS6 (#2217), p-4EBP1 Thr37/46 (#2855), p-MEK Ser217/221 (#9154), MEK (#9126), DUSP6 (#3058), β-actin (#4970), β-tubulin (Novus Biologicals, #NB600-936). Membranes were probed for 1 hour at room temperature in TBST with 3% bovine serum albumin (BSA). Membranes were subsequently incubated for 1 hour at room temperature with horseradish peroxidase-conjugated secondary antibody (Jackson ImmunoReserach) diluted 1:5000 in TBST containing 3% BSA. Western Lightning™ Plus-ECL (PerkinElmer) was used for chemiluminescent detection on a Xenogen IVIS 200.

Immunohistochemistry (IHC)

Animals were sacrificed and tumor samples were collected immediately following PET imaging, then subsequently fixed in 10% formalin for 24 hours. Tissues were then transferred to 70% ethanol prior to paraffin embedding. Tissues were sectioned (5 μm thickness) and stained for p-rpS6 (Cell Signaling, #4858, 1:100 primary dilution), p-AKT Ser473 (Cell Signaling, #4060, 1:100 primary dilution), Ki67 (Dako, #M7240, 1:100 primary dilution), p27 (Dako, #M7203, 1:100 primary dilution). Briefly, the tissue samples were de-paraffinized, rehydrated, and antigen retrieval was performed using citrate buffer (ph 6.0) solution for 15 minutes at 105 ºC followed and subsequently allowed to cool for 10 minutes at room temperature. The samples were then treated with 3% hydrogen peroxide to eliminate endogenous peroxidase activity. The sections were subsequently blocked with a serum-free protein blocking reagent for 20 minutes. Primary antibody detection was accomplished using the following system: The tissue sections were incubated at room temperature for 60 minutes at the noted dilutions followed by a 30 minute incubation utilizing the Envision + System-HRP Labeled Polymer detection method (Dako, Carpinteria, CA). Staining was completed after incubation with a 3,3'-Diaminobenzidine substrate-chromogen solution. Tissue slides were imaged at 40x magnification and manually scored to determine the percentage of positive cells per high power field.

qRT-PCR

RNA was collected by using RNeasy as suggested by supplier (QIAGEN). Both cDNA and realtime PCR experiments were carried out by using iScript cDNA synthesis kit and iQ™ SYBR Green Supermix (BIO-RAD) by supplier instruction. Amplifications were performed in a BIO-RAD CFX96 Real-Time System for 40 cycles. Data was acquired by Bio-Rad CFX Manager software and fold changes were analyzed as described by Schefe et al (107).

Statistical Analysis

Statistical significance of data was evaluated using the non-parametric Wilcoxon Rank Sum (Mann-Whitney U) tests using the GraphPad Prism 4 software package. Differences were considered statistically significant if $p < 0.05$.

CHAPTER 7

[^{18}F]-FLT PET TO PREDICT EARLY RESPONSE TO NEOADJUVANT THERAPY IN WILD-TYPE *KRAS* RECTAL CANCER

1. Abstract

Effective implementation of personalized medicine in oncology requires tailoring an individualized therapeutic regimen for a given patient based upon *the* molecular characteristics of their disease, and deploying effective biomarkers that predict responses early in the course of therapy. In this pilot study, we evaluated [^{18}F]-FLT PET, a non-invasive molecular imaging biomarker of thymidine salvage pathway activity, as a means to predict response to neoadjuvant therapy that included cetuximab in wild-type *KRAS* rectal cancer patients. Baseline [^{18}F]-FLT PET was collected prior to treatment initiation. Followup [^{18}F]-FLT was collected after three weekly infusions of cetuximab, and following a combined regimen of cetuximab, 5-FU, and radiation. Imaging-matched biopsies were collected concomitantly with each PET study. Diminished [^{18}F]-FLT PET was observed in 3/4 of patients following cetuximab treatment alone and in all patients following combination therapy. Reduced [^{18}F]-FLT PET following combination therapy predicted disease free status at surgery. Overall, [^{18}F]-FLT PET imaging agreed with Ki67 immunoreactivity from biopsy samples and surgically resected tissue and was predictive of treatment-induced p27 levels. To our knowledge, this study represents the first clinical evaluation of [^{18}F]-FLT PET to predict response to neoadjuvant therapy which included EGFR blockade with cetuximab in patients

with rectal cancer. Our results suggest that [^{18}F]-FLT PET is a promising imaging biomarker of treatment response in this setting.

2. Introduction

Standard imaging criteria for evaluating therapeutic response are based upon anatomical information according to Response Evaluation Criteria in Solid Tumors (RECIST) guidelines (1). These criteria, which are based solely on a reduction in tumor size, do not take advantage of cellular and molecular information now available through contemporary imaging methodologies. Importantly, since relevant cellular and molecular changes may precede changes in size and occur within hours of treatment, RECIST criteria and conventional imaging methods are frequently inadequate for assessing early tumor response. These limitations, coupled with the increasing clinical relevance of employing complex, molecularly targeted therapeutic regimens to treat cancer, highlight a critical need to accelerate the translation of novel imaging approaches that are capable of reporting cellular and molecular responses of tumor cells to therapy.

The widely used Positron emission tomography (PET) tracer 2-deoxy-2-(^{18}F)fluoro-D-glucose ([^{18}F]-FDG) is an important tool for cancer diagnosis and staging. [^{18}F]-FDG uptake and image contrast is predicated on increased glucose metabolism in neoplastic tissues compared to normal tissue. However, [^{18}F]-FDG tissue uptake broadly reflects a host of metabolic processes, highlighting an unmet clinical need for imaging methods that more directly measure proliferation.

The PET tracer 3′-deoxy-3′[18F]-fluorothymidine ([^{18}F]-FLT) has been proposed as a potential imaging biomarker of proliferation in oncology, especially to predict response to therapy in clinical trials and drug development (14, 84). [^{18}F]-FLT PET serves as a marker of proliferation by reporting on the activity of the thymidine salvage pathway. Upon cellular internalization by nucleoside transporters, [^{18}F]-FLT is phosphorylated by thymidine kinase 1 (TK1). [^{18}F]-FLT-monophosphate is trapped and accumulates in the cell resulting in imaging contrast. However, unlike thymidine, [^{18}F]-FLT is not incorporated into the DNA. TK1 is primarily expressed during DNA synthesis (S-phase) and is diminished in quiescent cells, forming the basis of the use of [^{18}F]-FLT PET as a proliferation marker. [^{18}F]-FLT PET has been thoroughly evaluated in treatment response studies in pre-clinical (25, 26, 43) and clinical (19, 56, 92, 108) studies. Unlike more generalizable proliferation markers, such as Ki67, [^{18}F]-FLT PET reflects proliferative indices to variable and potentially unreliable extents (93). [^{18}F]-FLT PET cannot discriminate moderately proliferative, thymidine salvage-driven tumors from those of high proliferative index that rely primarily upon *de novo* thymidine synthesis. Accordingly, the magnitude of [^{18}F]-FLT uptake should not necessarily be considered a surrogate of proliferative index (93). Nonetheless, [^{18}F]-FLT PET may reflect important cellular and molecular events associated with response to therapy, such as elevated p27.

The epidermal growth factor receptor (EGFR, HER1, ErbB-1) is frequently over-expressed in colorectal cancer (CRC) and, as such, has become a target for therapy in advanced CRC (109). A number of small molecule inhibitors of EGFR

tyrosine kinase inhibitors have been developed, and have shown promise in manny settings such as mutant EGFR lung cancer (110). However, trials of EGFR tyrosine kinase inhibitors have not been successful in CRC (111). Treatment of CRC with monoclonal antibodies, such as cetuximab (Erbitux), has shown more promise clinically when used in patients whose tumors express wild-type *KRAS* (112-114). We have previously evaluated [^{18}F]-FLT PET to assess treatment response to cetuximab in a preclinical (25) and clinical studies (111). Here we report the results of a correlative pre- and post-treatment [^{18}F]-FLT PET study that evaluated this imaging metric to predict response in a phase II neoadjuvant clinical trial of cetuximab followed by combined cetuximab and chemoradiotherapy in patients with advanced CRC.

3. Materials and Methods

Patients

All studies were approved by the Vanderbilt Institutional Review Board. Written informed consent was obtained from the patients prior to patient enrollment. Patients with proven wild-type *KRAS*-expressing rectal tumors were enrolled in a multi-center clinical trial investigating the benefits of adding

Patient ID	Sex	Age	Baseline ^{18}F-FLT PET (SUV_{max})	Post cetuximab ^{18}F-FLT PET (SUV_{max})	Change from baseline ^{18}F-FLT PET	Post cetuximab and chemoradiotherapy ^{18}F-FLT PET (SUV_{max})	Change from baseline ^{18}F-FLT PET	Stage at surgery
1	M	39	6.66	5.45	-18.24%	2.21	-66.82%	ypT3N1c
2	F	45	5.03	N/A				
3	F	48	7.29	10.58	45.06%	1.84	-74.79%	pCR
4	M	58	9.62	4.29	-55.40%	2.51	-73.94%	pCR
5	M	62	8.77	6.52	-25.59%	1.80	-79.50%	ypT2N0

Table 7.1. Patient characteristics, ^{18}F-FLT PET imaging, and clinical results.

cetuximab to standard neoadjuvant chemoradiotherapy. A summary of patient characteristics can be found in **Table 7.1** and a treatment and imaging study schema is shown in **Fig. 7.1**. A pre-treatment [^{18}F]-FLT PET/CT study and tissue biopsy were obtained immediately prior to treatment with a loading dose of 400 mg/m^2 cetuximab, followed by weekly infusions of 250 mg/m^2 cetuximab. A second [^{18}F]-FLT PET/CT study and tissue biopsy were obtained after the third cetuximab infusion, and prior to the initiation of chemotherapy and radiation. Cetuximab infusions continued weekly combined with continuous infusion of 225mg/m^2/day fluorouracil (5-FU) and radiation therapy (50.4 Gy in 28 fractions) for an additional 6 weeks. A third [^{18}F]-FLT PET/CT image was obtained prior to surgical resection of the tumor.

Radiochemical synthesis

[^{18}F]-FLT was prepared from [^{18}F]-fluoride in a two-step, one-pot reaction as previously described (25, 77) using a GE TRACERlab FX-FN automated module. Aqueous [^{18}F]-fluoride was eluted with Kryptofix-222 and K_2CO_3 in CH_3CN/H_2O

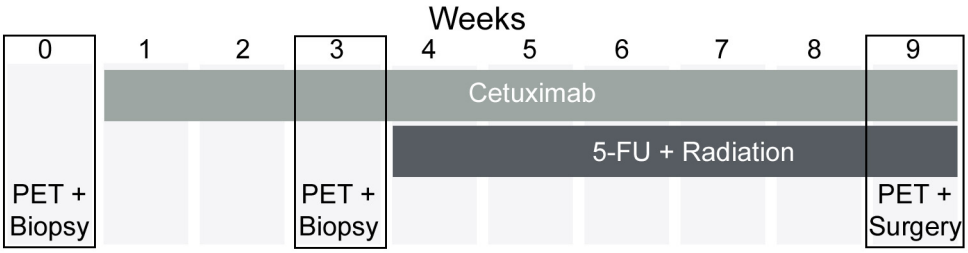

Fig. 7.1. Study schema. Baseline [^{18}F]-FLT PET/CT scan and tissue biopsy were collected prior to treatment. A second [^{18}F]-FLT PET/CT and scan were collected following three weekly infusions of cetuximab. Subsequently, patients received continuous infusion of 5-FU and radiotherapy in conjunction with weekly cetuximab. Prior to surgery, a final [^{18}F]-FLT PET/CT scan was obtained and tissue was collected from the surgical resection.

into the reaction vessel. Three sequences of heating (110°C) with He(*g*) flow resulted in dry [^{18}F]-fluoride/Kryptofix-222/K_2CO_3. The cyclic precursor 2,3′-anhydro-5′-*O*-benzoyl-2′-deoxythymidine (ABX Advanced Biochemical Compounds) was added in DMSO and reacted for 10 min at 160°C. The benzoyl-protecting group was removed from the labeled intermediate by basic hydrolysis (0.25 mol/L NaOH, 50°C, 10 minutes). The reaction mixture was purified on a semi-preparative C-18 high-performance liquid chromatography column eluting with 10% ethanol/10 mmol/L sodium phosphate buffer and sterilized by 0.2 μm membrane filtration. Radiochemical identity, purity, and specific activity were determined by analytic high-performance liquid chromatography. The [^{18}F]-FLT product was obtained with average radiochemical purity of 98.3% and specific activity of 345.5 TBq/mmol.

[^{18}F]-FLT PET/CT Imaging

Patients received an intravenous injection of 185 MBq of [^{18}F]-FLT and then rested for 60 minutes prior to imaging. Imaging was performed with an integrated PET/CT scanner (Discovery LS, GE Healthcare), consisting of a combined full-ring PET scanner (Advance NXi) and an eight-section helical CT scanner (Light Speed Plus). The CT was performed with 140 kV, 80 mA, a tube-rotation time of 0.8 seconds per rotation, a pitch of 1.675 mm/rotation, with CT slice thickness of 3.75 mm at intervals of 3.27 mm and a matrix of 512 by 512 pixels. The CT data were reconstructed with a slice thickness of 5.0 mm and a matrix of 512 by 512 pixels. Patients were allowed normal, quiet breathing during imaging. PET data

sets were reconstructed iteratively using the ordered subsets expectation maximization (OSEM) algorithm with segmented attenuation correction (two iterations). PET images were up-interpolated by vendor-provided software to match the CT matrix for image fusion. Independent as well as co-registered images were displayed by using a vendor provided workstation (Xeleris; GE Medical Systems). Images were evaluated by a qualified nuclear medicine physician (Dr. Ronald C. Walker, MD).

Immunohistochemistry

Biopsy samples were blocked in paraffin and sectioned prior to immunostaining for proliferation markers including Ki67, TK1, and p27. Five μM thick sections were incubated with primary monoclonal antibodies for Ki67 (Dako #M7240, 1:100 dilution), TK1 (Abcam #57757, 1:100 dilution) and p27 (Dako #M7203, 1:100 dilution). Briefly, tissues were deparaffinized, rehydrated, and antigen retrieval was performed using a citrate buffer solution (pH 6.0) applied for 15 minutes at 105º C followed by a 10 minute cool down at room temperature. A solution of 3% H_2O_2 was used to eliminate endogenous peroxidase activity and then blocked with a serum-free protein blocking reagent for 20 minutes. For detection of primary antibodies, tissue sections were incubated for 60 minutes at room temperature at the dilutions noted above. Subsequently, samples were incubated for 30 minutes utilizing the Envision+ System-HRP Labeled Polymer detection method. Staining was completed after incubation with a DAB substrate-chromagen solution. Stained samples were evaluated by a gastrointestinal

pathologist (Dr. M. Kay Washington, MD, PhD) and imaged at high magnification for reproduction.

Tumor genotyping

DNA was extracted from paraffin fixed, formalin embedded samples from each patient enrolled in the study. Tumor genotypes were assayed from 20 ng DNA using the SNaPshot mutational profiling method which consists of

KRAS

Position	AA mutant	Nucleotide mutant
G12	p.G12C	c.34G>T
	p.G12S	c.34G>A
	p.G12R	c.34G>C
	p.G12V	c.35G>T
	p.G12A	c.35G>C
	p.G12D	c.35G>A
G13	p.G13C	c.37G>T
	p.G13S	c.37G>A
	p.G13R	c.37G>C
	p.G13D	c.38G>A
	p.G13A	c.38G>C
	p.G13V	c.38G>T
Q61	p.Q61K	c.181C>A
	p.Q61R	c.182A>G
	p.Q61L	c.182A>T
	p.Q61H	c.183A>T
		c.183A>C
A146	p.A146T	c.436G>A
	p.A146P	c.436G>C
	p.A146V	c.437C>T
K117	p.K117N	c.351A>C
		c.351A>T

BRAF

G466	p.G466V	c.1397G>T
G469	p.G469E	c.1406G>A
	p.G469A	c.1406G>C
	p.G469V	c.1406G>T
D594	p.D594G	c.1781A>G
	p.D594V	c.1781A>T
G596	p.G596R	c.1786G>C
V600	p.V600E	c.1799T>A

AKT

E17	p.E17K	c.49G>A

PIK3CA

Position	AA mutant	Nucleotide mutant
H1047	p.H1047R	c.3140A>G
	p.H1047L	c.3140A>T
E542	p.E542K	c.1624G>A
E545	p.E545K	c.1633G>A
	p.E545Q	c.1633G>C
	p.E545A	c.1634A>C
	p.E545G	c.1634A>G
	p.E545V	c.1634A>T
Q546	p.Q546K	c.1636C>A
	p.Q546E	c.1636C>G
	p.Q546P	c.1637A>C
	p.Q546R	c.1637A>G
	p.Q546L	c.1637A>T
D549	p.D549N	c.1645G>A

SMAD4

E330	p.E330A	c.989A>C
D351	p.D351H	c.1051G>C
	p.D351N	c.1051G>A
D355	p.D355E	c.1065C>A
R361	p.R361S	c.1081C>A
	p.R361C	c.1081C>T
	p.R361H	c.1082G>A

PTEN

R233	p.R233	c.697C>T
R159	p.R159S	c.477G>T
R267	p.R267fs*9	c.800delA

NRAS

G12	p.G12C	c.34G>T
	p.G12S	c.34G>A
	p.G12A	c.35G>C
	p.G12D	c.35G>A
	p.G12V	c.35G>T
Q61	p.Q61K	c.181C>A
	p.Q61R	c.182A>G

Table 7.2. Point mutations detected by SNaPshot assay

multiplexed PCR, multiplexed single-base primer extension, and capillary electrophoresis (115-117). The current assay was designed to detect 62 point mutations in 7 genes (**Table 7.2**). Briefly, PCR primers were pooled to amplify the target DNA, and PCR was performed using the following conditions: 95^{o}C (8 min), followed by 40 cycles of 95^{o}C (20 sec), 58^{o}C (30 sec) and 72^{o}C (1 min), and then a final extension of 72^{o}C (3 min). Next, PAGE-purified primers were pooled together and multiplex single-base extension reactions were performed on Exo-SAP-it treated (USB) PCR products using the following conditions: 96^{o}C (30 sec), followed by 35 cycles of 96^{o}C (10 sec), 50^{o}C (5 sec), and 60^{o}C (30 sec). Extension products were applied to capillary electrophoresis in an ABI 3730 analyzer and the data were interpreted using ABI GeneMapper software (version 4.0). Human male genomic DNA (Promega) was used as a wild type control. Spiking primers were mixed to create a pan-positive control mix for the assay.

4. Results

[^{18}F]-FLT PET *Imaging*

Five patients with a confirmed wild-type *KRAS* rectal tumor were enrolled in the imaging study. Pre-treatment [^{18}F]-FLT PET scans were acquired for each patient. The typical biodistribution of [^{18}F]-FLT was observed in all patients, with elevated activity in bone marrow, urinary excretion, and accumulation in the liver. Elevated [^{18}F]-FLT uptake was observed in all rectal tumors, with SUV_{max} ranging from 5.03 to 9.62 (**Table 7.1, Fig. 7.2**). Given this elevated uptake compared to surrounding normal rectum, all rectal cancers in this study were easily visualized

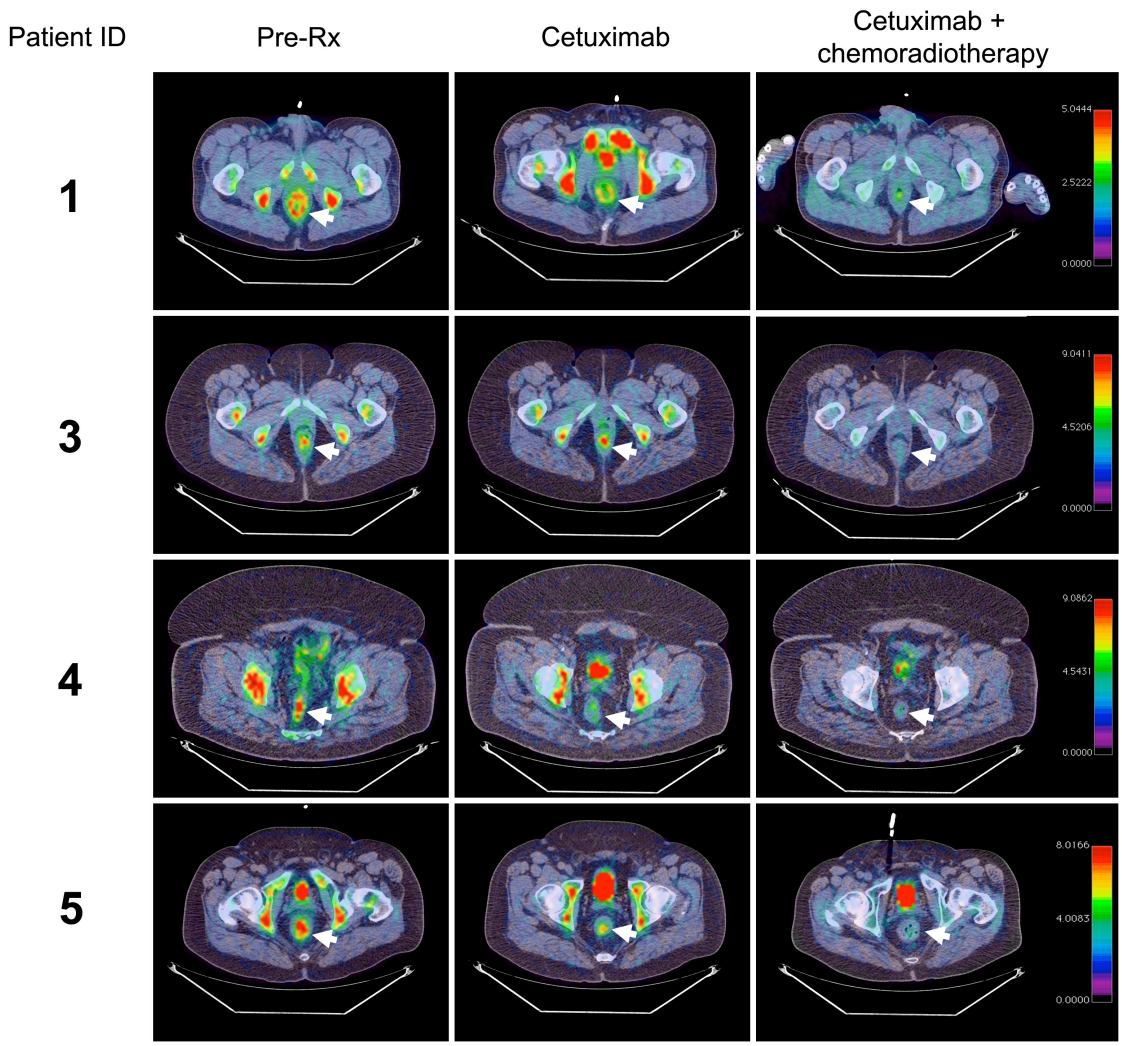

Fig. 7.2. [^{18}F]-FLT PET/CT imaging. Transverse, coregistered [^{18}F]-FLT PET/CT images for each patient completing the study are shown at pre-treatment, post-cetuximab therapy, and after combined cetuximab-chemoradiotherapy. Tumors are denoted by arrow. Images for each patient are windowed similarly.

with [^{18}F]-FLT PET. One patient completed baseline imaging and subsequently was withdrawn from the study following an anaphylactic response to cetuximab (118, 119). Following cetuximab-treatment, [^{18}F]-FLT biodistributions were similar to pre-treatment levels throughout normal tissue. [^{18}F]-FLT uptake in rectal tumors following cetuximab as monotherapy was reduced by 20%, 55%, and 25% in three patients, but was elevated by 45% in one patient relative to the pre-treatment scan (**Fig. 7.3**). After combined cetuximab and chemoradiotherapy,

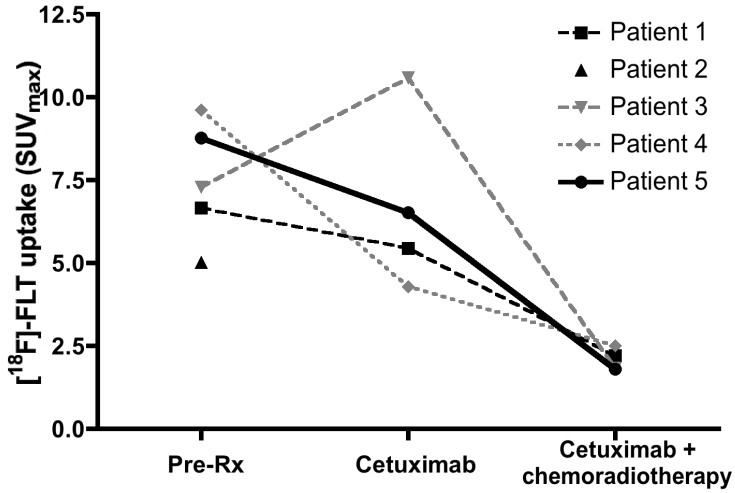

Fig. 7.3. Quantification of [^{18}F]-FLT PET imaging. [^{18}F]-FLT uptake in rectal cancer (SUV_{max}) at each imaging time point.

[^{18}F]-FLT uptake in rectal tumors was reduced by over 70% in all patients compared to the pre-treatment scans. Reduced [^{18}F]-FLT uptake was observed in the bone marrow in the final post-treatment scan consistent with radiotherapy (120).

Immunohistochemistry

Representative high-power fields of Ki67, p27, and TK1 IHC for tumor specimens evaluated in this study are shown in **Fig. 7.4** and **Fig. 7.5**. In all patients, prominent Ki67 IHC staining was observed in pre-treatment biopsies. Reduced Ki67, was observed in all patients following cetuximab, except in patient 3 who also did not exhibit reduced [^{18}F]-FLT PET at this time point. Prior to cetuximab treatment, weak p27 immunostaining was observed in all tumor samples. Cetuximab treatment resulted in elevated nuclear p27 in all patients that exhibited response by [^{18}F]-FLT PET, implying that [^{18}F]-FLT PET reflected

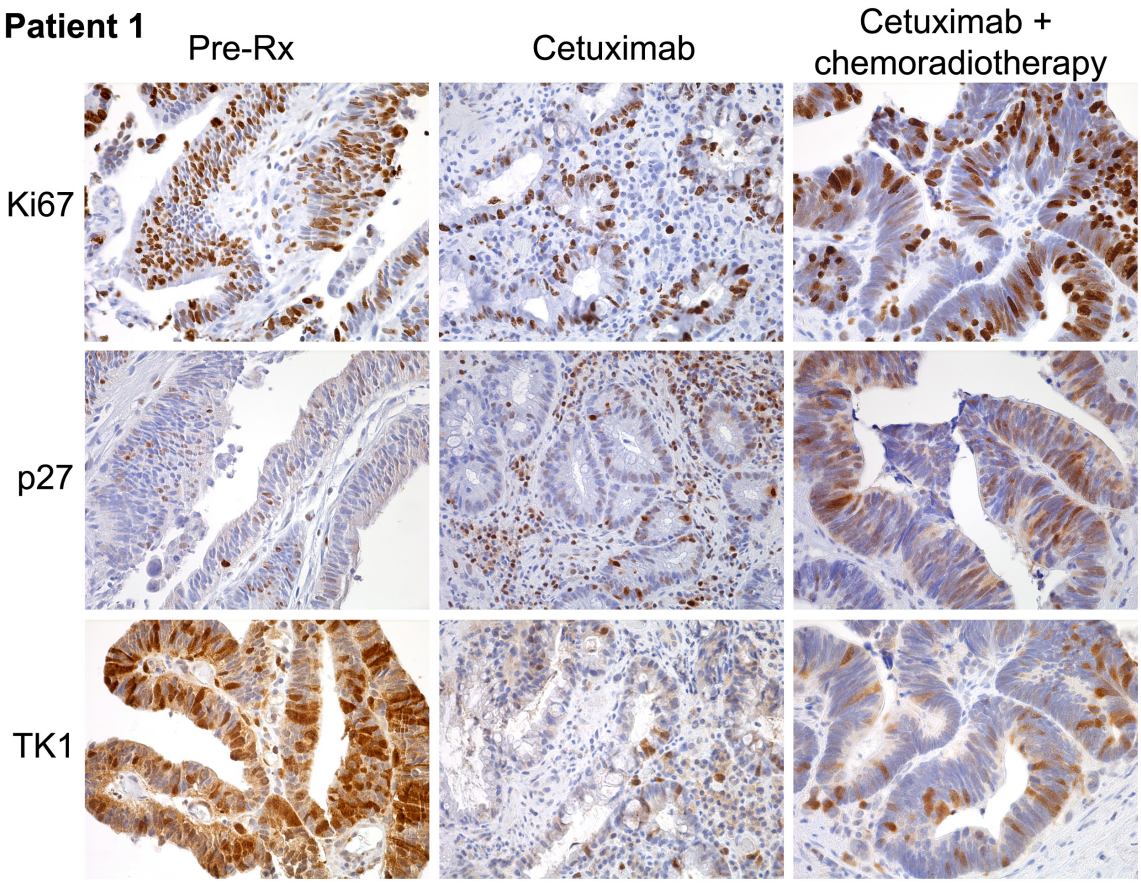

Fig 7.4. Ki67, p27, and TK1 immunohistochemistry in patient 1. Representative 40x fields are shown. Ki67 IHC staining was reduced from pre-treatment levels following both single and combined therapy. Increased p27 immunoreactivity was observed after cetuximab monotherapy compared to pre-treatment, and p27 was further increased after completion of cetuximab and chemoradiotherapy. TK1 staining was greatly reduced at both time points.

p27-dependent cell cycle inhibition. In patient 3, where [^{18}F]-FLT PET was not decreased following cetuximab, p27 levels were unchanged from baseline. In agreement with imaging, tumors exhibited robust TK1 immunoreactivity prior to treatment (**Fig. 7.4**). In agreement with [^{18}F]-FLT PET, fewer TK1-positive cells were observed in patients with decreased [^{18}F]-FLT tumor uptake. Reduced TK1 immunoreactivity was also observed following cetuximab and chemoradiotherapy.

Patient ID	KRAS p.G12C; c.34G>T	KRAS p.G12S; c.34G>A	KRAS p.G12R; c.34G>C	KRAS p.G12V; c.35G>T	KRAS p.G12A; c.35G>C	KRAS p.G12D; c.35G>A	KRAS p.G13C; c.37G>T	KRAS p.G13S; c.37G>A	KRAS p.G13R; c.37G>C	KRAS p.G13D; c.38G>A	KRAS p.G13A; c.38G>C	KRAS p.G13V; c.38G>T	KRAS p.Q61K; c.181C>A	KRAS p.Q61R; c.182A>G	KRAS p.Q61L; c.182A>T	KRAS p.Q61H; c.183A>T	KRAS p.Q61H; c.183A>C	KRAS p.A146T; c.436G>A	KRAS p.A146P; c.436G>C	KRAS p.A146V; c.437C>T	KRAS p.K117N; c.351A>C	KRAS p.K117N; c.351A>T	AKT1 p.E17K; c.49G>A
1	ND	ND	ND	ND	ND	ND	ND	ND	ND	ND	ND	ND	ND	ND	ND	ND	ND	ND	ND	ND	ND	ND	ND
2	ND	ND	ND	ND	ND	ND	ND	ND	ND	ND	ND	ND	ND	ND	ND	ND	ND	ND	ND	ND	■	■	ND
3	ND	ND	ND	ND	ND	ND	ND	ND	ND	ND	ND	ND	ND	ND	ND	ND	ND	ND	ND	ND	ND	ND	ND
4	ND	ND	ND	ND	ND	ND	ND	ND	ND	ND	ND	ND	ND	ND	ND	ND	ND	ND	ND	ND	ND	ND	ND
5	ND	ND	ND	ND	ND	ND	ND	ND	ND	ND	ND	ND	ND	ND	ND	ND	ND	ND	ND	ND	ND	ND	ND

Patient ID	BRAF p.G466V; c.1397G>T	BRAF p.G469E; c.1406G>A	BRAF p.G469A; c.1406G>C	BRAF p.G469V; c.1406G>T	BRAF p.D594G; c.1781A>G	BRAF p.D594V; c.1781A>T	BRAF p.G596R; c.1786G>C	BRAF p.V600E; c.1799T>A	PIK3CA p.H1047R; c.3140A>G	PIK3CA p.H1047L; c.3140A>T	PIK3CA p.E542K; c.1624G>A	PIK3CA p.E545K; c.1633G>A	PIK3CA p.E545Q; c.1633G>C	PIK3CA p.E545A; c.1634A>C	PIK3CA p.E545G; c.1634A>G	PIK3CA p.E545V; c.1634A>T	PIK3CA p.Q546K; c.1636C>A	PIK3CA p.Q546E; c.1636C>G	PIK3CA p.Q546P; c.1637A>C	PIK3CA p.Q546R; c.1637A>G	PIK3CA p.Q546L; c.1637A>T	PIK3CA p.D549N; c.1645G>A
1	ND	ND	ND	ND	ND	ND	ND	ND	ND	ND	ND	ND	ND	ND	ND	ND	ND	ND	ND	ND	ND	ND
2	ND	ND	ND	ND	ND	ND	ND	ND	ND	ND	ND	ND	ND	ND	ND	ND	ND	ND	ND	ND	ND	ND
3	ND	ND	ND	ND	ND	ND	ND	ND	ND	ND	ND	ND	ND	ND	ND	ND	ND	ND	ND	ND	ND	ND
4	ND	ND	ND	ND	ND	ND	ND	ND	ND	ND	ND	ND	ND	ND	ND	ND	ND	ND	ND	ND	ND	ND
5	ND	ND	ND	ND	ND	ND	ND	ND	ND	ND	ND	ND	ND	ND	ND	ND	ND	ND	ND	ND	ND	ND

Patient ID	SMAD4 p.E330A; c.989A>C	SMAD4 p.D351H; c.1051G>C	SMAD4 p.D351N; c.1051G>A	SMAD4 p.D355E; c.1065C>A	SMAD4 p.R361S; c.1081C>A	SMAD4 p.R361C; c.1081C>T	SMAD4 p.R361H; c.1082G>A	PTEN p.R233*; c.697C>T	PTEN p.R159S; c.477G>T	PTEN p.RR267fs*9; c.800delA	NRAS p.G12S; c.34G>A	NRAS p.G12A; c.34G>C	NRAS p.G12C; c.34G>T	NRAS p.G12D; c.35G>A	NRAS p.G12V; c.35G>T	NRAS p.Q61K; c.181C>A	NRAS p.Q61R; c.182A>G
1	ND	ND	ND	ND	ND	ND	ND	ND	ND	ND	ND	ND	ND	ND	ND	ND	ND
2	ND	ND	ND	ND	ND	ND	ND	ND	ND	ND	ND	ND	ND	ND	ND	ND	ND
3	ND	ND	ND	ND	ND	ND	ND	ND	ND	ND	ND	ND	ND	ND	ND	ND	ND
4	ND	ND	ND	ND	ND	ND	ND	ND	ND	ND	ND	ND	ND	ND	ND	ND	ND
5	ND	ND	ND	ND	ND	ND	ND	ND	ND	ND	ND	ND	ND	ND	ND	ND	ND

Table 7.3. Characterization of point mutations in *KRAS, BRAF, PIK3CA, SMAD4, PTEN,* and *NRAS* as measured by SNaPshot genotyping. ND, not detected

Tumor genotyping

No point mutations in *KRAS, BRAF, AKT, BRAF, PIK3CA, SMAD4, PTEN,* or *NRAS* were detected in any tumor sample evaluated in this study (**Table 7.3**).

5. Discussion

These studies mirror our previous clinical experience using [^{18}F]-FLT PET to predict pharmacodynamic response to cetuximab in Ménétrier's disease, a rare, premalignant, hyperproliferative disorder of the stomach (27). Like this study, in that trial we found that [^{18}F]-FLT PET was useful to visualize

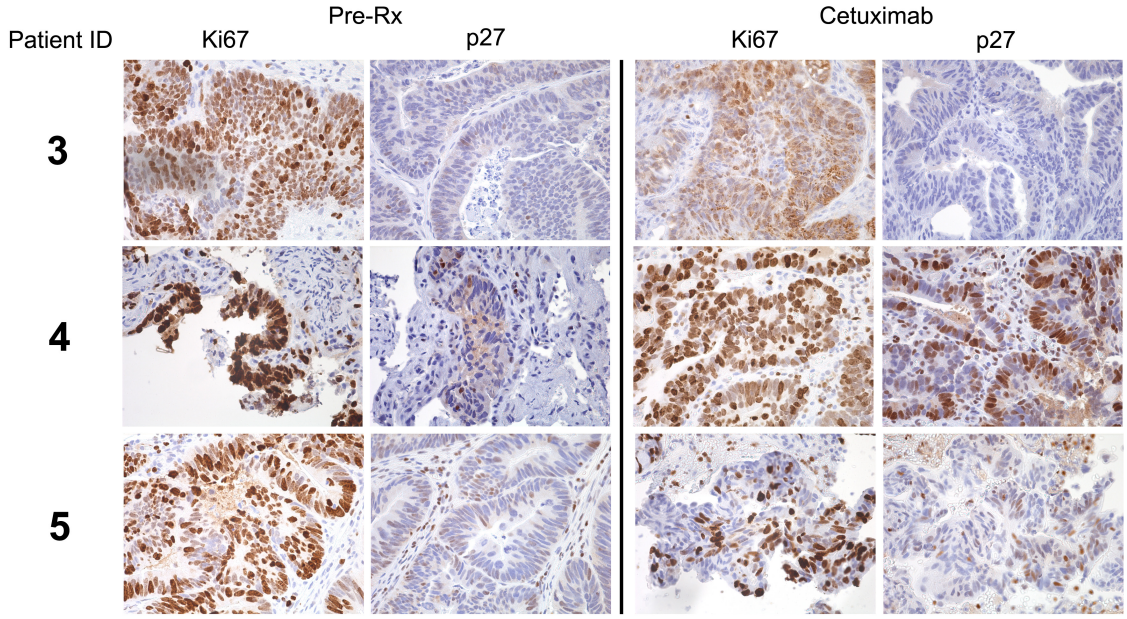

Fig. 7.5. Ki67 and p27 immunohistochemistry in patients 3-5. Representative 40x fields are shown. Prior to treatment Ki67 staining was observed in almost all tumor cells for all patients. Almost no p27 immunoreactivity was detected in any patient prior to treatment. After cetuximab, Ki67 staining was not changed in patient 3 or 4, however, was greatly reduced in patient 5. p27 staining was inversely related to ^{18}F-FLT PET. In patient 3 when ^{18}F-FLT PET was not reduced following cetuximab treatment, no p27 induction was observed. However, patients 4 and 5, where ^{18}F-FLT PET was reduced after treatment, increased p27 staining was seen compared to pre-treatment tissue. No tissue was available from these patients at surgery following cetuximab and chemoradiotherapy treatment.

hyperproliferative tissue, as well as to predict early response to cetuximab therapy.

This study represents the first clinical evaluation of [^{18}F]-FLT PET to predict response to neoadjuvant therapy in rectal cancer that includes EGFR blockade with cetuximab. Historically, a key issue raised against the use of [^{18}F]-FLT PET for tumor detection has been the modest uptake of the tracer in many tissues with respect to surrounding normal tissue. Interestingly, however, this phenomenon was not observed with the rectal cancers evaluated in this study, which exhibited excellent signal to noise ratios. Our findings are in agreement with those of others (121, 122), which confirm that [^{18}F]-FLT PET is well suited for imaging rectal cancer. All patients who completed the study demonstrated a clinical response to therapy. Interestingly, [^{18}F]-FLT PET was reduced in 3/4 patients following cetuximab monotherapy with one patient exhibiting elevated [^{18}F]-FLT uptake at this time point. We interpret these findings to suggest that [^{18}F]-FLT PET provided mechanistic insight into tumor response since imaging accurately reflected the induction of p27 or lack thereof. In fact, [^{18}F]-FLT PET results, supported by Ki67 and p27 immunoreactivity, appear to suggest that patient 3 did not experience an anti-proliferation benefit from the addition of cetuximab to the more conventional chemoradiotherapy regimen. In future studies that may employ similar regimens, post-cetuximab [^{18}F]-FLT PET could potentially be incorporated to predict those patients who are most likely to benefit from this drug.

At the conclusion of combination therapy, [^{18}F]-FLT uptake was reduced by at least 65% from baseline in all four patients. It is currently unclear what role cetuximab played in modulating [^{18}F]-FLT PET at this time point. Previously, [^{18}F]-FLT PET has been reduced following chemoradiotherapy in rectal tumors regardless of clinical outcome (121). Notably, in this study, reduced [^{18}F]-FLT PET following chemoradiotherapy correlated with complete response, but the limited number of patients evaluated here does not warrant a definitive conclusion.

6. Conclusion

To our knowledge, this study represents the first clinical evaluation of [^{18}F]-FLT PET to predict response to neoadjuvant therapy which included EGFR blockade with cetuximab in patients with rectal cancer. Our results suggest that [^{18}F]-FLT PET is a promising imaging biomarker of treatment response in this setting.

CHAPTER 8

DISCUSSION AND CONCLUSION

Studies presented in this dissertation elucidate a portion of the molecular determinants that affect [^{18}F]-FLT PET imaging as an imaging biomarker proliferation and response to targeted therapy in CRC. Using pre-clinical mouse models of human CRC, [^{18}F]-FLT PET was shown to measure TK1 protein levels in a tumor, was blind to utilization of the *de novo* pathway of thymidine synthesis, and did not always correlate with Ki67 IHC measures of cellular proliferation in treatment naive tumors. Preclinical mouse models of CRC were also employed to document that changes in [^{18}F]-FLT PET can be discordant with treatment response and, in some cases, may be affected by, and can be used to assess, pro-survival responses associated with resistance. In the clinical setting, [^{18}F]-FLT PET was shown to correlate with p27 induction in wild-type *KRAS* rectal cancers following EGFR blockade with cetuximab. Each of these components advance the understanding the strengths and weaknesses of [^{18}F]-FLT PET and how this biomarker can be utilized in clinical studies, as well as drug development.

Although [^{18}F]-FLT PET was developed in the mid-to-late 1990s (14) and has been subsequently studied rather extensively in pre-clinical and clinical studies, [^{18}F]-FLT PET is too often considered a simple marker of proliferation. [^{18}F]-FLT is phosphorylated by TK1 and trapped in the cell, and while TK1 is an

important protein enabling DNA synthesis, TK1 protein levels do not necessarily correlate with proliferation. Ki67 IHC staining has become the gold standard metric of cellular proliferation and frequently conflicts with [^{18}F]-FLT PET. The work presented in this dissertation elucidate mechanisms that decouple [^{18}F]-FLT PET from proliferation, such as utilization of the *de novo* pathway of thymidine synthesis and through pro-survival signaling following therapy. Better understanding of these effects in the imaging community will aid clinical use and interpretation of [^{18}F]-FLT PET. Clinicians interpreting [^{18}F]-FLT PET should be trained to be familiar with these issues.

This dissertation reports the sensitivity of [^{18}F]-FLT PET to report PI3K-mTOR signaling in response to targeted therapy. In a clinical setting where [^{18}F]-FLT PET is used to guide treatment regimens, the activity of pro-survival signaling, which results in bolstered [^{18}F]-FLT PET despite potential target inhibition, could result in patients being removed from an otherwise effective therapy, an obviously non-optimal outcome. However, for those familiar with TK1 regulatory machinery, the sensitivity of [^{18}F]-FLT PET to activation of pro-survival signaling may provide information about potential mechanisms of resistance. While great advances have been made in the treatment of cancer, most targeted therapies only increase survival by months, rather than years. Early measurement of pro-survival signaling activation using [^{18}F]-FLT may aid in the development of personalized treatment regimens. The results reported in this dissertation are a first step towards such an outcome.

Translating what was learned in pre-clinical studies, in the final aim of this dissertation reports the clinical use of [^{18}F]-FLT PET is reported in a focused cohort of rectal cancer patients. In 3/4 patients, biological response to single agent cetuximab was observed which included increased p27 and reduced Ki67, while one patient exhibited neither. In all four patients, [^{18}F]-FLT PET correctly predicted biological response to single agent cetuximab. As this was the first study to explore [^{18}F]-FLT PET as a marker of EGFR blockade with a monoclonal antibody in rectal cancer, further study is required using similar methods to better understand the effects of treatment in primary human tumors. However, these early results are encouraging that [^{18}F]-FLT PET may have an important clinical role in this setting.

In conclusion, this dissertation elucidates, in part, the molecular determinants of [^{18}F]-FLT PET during treatment response in pre-clinical mouse models of CRC as well as in human rectal cancer. Far from being a simple marker of cellular proliferation, [^{18}F]-FLT PET imaging is a measure of TK1 protein expression which can be a complex process affected by a number of signaling pathways that can decouple [^{18}F]-FLT PET from measures of cell proliferation. While [^{18}F]-FLT PET holds great promise for measuring treatment response, it may be helpful to have *a priori* knowledge of the basis of a patient's tumor to be most informed about the data [^{18}F]-FLT PET may provide. Future studies should continue to explore the molecular target of [^{18}F]-FLT, TK1, as a predictive measure of outcome and response to treatment in oncology.

REFERENCES

1. Eisenhauer EA, Therasse P, Bogaerts J, et al. New response evaluation criteria in solid tumours: revised RECIST guideline (version 1.1). Eur J Cancer 2009; 45: 228-47.
2. Röntgen W. On a new kind of rays. Nature 1896; 53: 274.
3. Mankoff DA. A definition of molecular imaging. J Nucl Med 2007; 48: 18N, 21N.
4. Peterson TE, Manning HC. Molecular imaging: 18F-FDG PET and a whole lot more. J Nucl Med Technol 2009; 37: 151-61.
5. Beckmann N. In Vivo magnetic resonance techniques and drug discovery. Brazilian Journal of Physics 2006; 36: 16-22.
6. Cherry S, Dahlbom M. PET: physics, instrumentation, and scanners. PET; 2006: Springer; 2006. p. 1-117.
7. Shields AF, Mankoff DA, Link JM, et al. Carbon-11-thymidine and FDG to measure therapy response. J Nucl Med 1998; 39: 1757-62.
8. Shields AF, Mankoff D, Graham MM, et al. Analysis of 2-carbon-11-thymidine blood metabolites in PET imaging. J Nucl Med 1996; 37: 290-6.
9. Reinhardt MJ, Kubota K, Yamada S, Iwata R, Yaegashi H. Assessment of cancer recurrence in residual tumors after fractionated radiotherapy: a comparison of fluorodeoxyglucose, L-methionine and thymidine. J Nucl Med 1997; 38: 280-7.
10. Barthel H, Cleij MC, Collingridge DR, et al. 3'-deoxy-3'-[18F] fluorothymidine as a new marker for monitoring tumor response to antiproliferative therapy in vivo with positron emission tomography. Cancer Res 2003; 63: 3791-8.
11. Chen W, Cloughesy T, Kamdar N, et al. Imaging proliferation in brain tumors with 18F-FLT PET: comparison with 18F-FDG. J Nucl Med 2005; 46: 945-52.
12. Choi SJ, Kim JS, Kim JH, et al. [18F]3'-deoxy-3'-fluorothymidine PET for the diagnosis and grading of brain tumors. Eur J Nucl Med Mol Imaging 2005; 32: 653-9.
13. Cobben DC, Elsinga PH, van Waarde A, Jager PL. Correspondence re: H. Barthel et al., 3'-deoxy-3'-[(18)F]fluorothymidine as a new marker for monitoring tumor response to antiproliferative therapy in vivo with positron emission tomography. Cancer Res., 63: 3791-3798, 2003. Cancer Res 2003; 63: 8558-9; author reply 60.
14. Shields AF, Grierson JR, Dohmen BM, et al. Imaging proliferation in vivo with [F-18]FLT and positron emission tomography. Nat Med 1998; 4: 1334-6.
15. Arner ES, Eriksson S. Mammalian deoxyribonucleoside kinases. Pharmacol Ther 1995; 67: 155-86.
16. Mankoff DA, Eary JF, Link JM, et al. Tumor-specific positron emission tomography imaging in patients: [18F] fluorodeoxyglucose and beyond. Clin Cancer Res 2007; 13: 3460-9.

17. Grierson JR, Schwartz JL, Muzi M, Jordan R, Krohn KA. Metabolism of 3'-deoxy-3'-[F-18]fluorothymidine in proliferating A549 cells: validations for positron emission tomography. Nucl Med Biol 2004; 31: 829-37.
18. Grierson JR, Shields AF. Radiosynthesis of 3'-deoxy-3'-[(18)F] fluorothymidine: [(18)F]FLT for imaging of cellular proliferation in vivo. Nucl Med Biol 2000; 27: 143-56.
19. Muzi M, Spence AM, O'Sullivan F, et al. Kinetic analysis of 3'-deoxy-3'-18F-fluorothymidine in patients with gliomas. J Nucl Med 2006; 47: 1612-21.
20. Schwartz JL, Tamura Y, Jordan R, Grierson JR, Krohn KA. Monitoring tumor cell proliferation by targeting DNA synthetic processes with thymidine and thymidine analogs. J Nucl Med 2003; 44: 2027-32.
21. Wagner M, Seitz U, Buck A, et al. 3'-[18F]fluoro-3'-deoxythymidine ([18F]-FLT) as positron emission tomography tracer for imaging proliferation in a murine B-Cell lymphoma model and in the human disease. Cancer Res 2003; 63: 2681-7.
22. Bradshaw HD, Jr. Molecular cloning and cell cycle-specific regulation of a functional human thymidine kinase gene. Proc Natl Acad Sci U S A 1983; 80: 5588-91.
23. Mikulits W, Hengstschlager M, Sauer T, Wintersberger E, Mullner EW. Overexpression of thymidine kinase mRNA eliminates cell cycle regulation of thymidine kinase enzyme activity. J Biol Chem 1996; 271: 853-60.
24. Schwartz JL, Tamura Y, Jordan R, Grierson JR, Krohn KA. Effect of p53 activation on cell growth, thymidine kinase-1 activity, and 3'-deoxy-3'fluorothymidine uptake. Nucl Med Biol 2004; 31: 419-23.
25. Manning HC, Merchant NB, Foutch AC, et al. Molecular imaging of therapeutic response to epidermal growth factor receptor blockade in colorectal cancer. Clin Cancer Res 2008; 14: 7413-22.
26. Shah C, Miller TW, Wyatt SK, et al. Imaging biomarkers predict response to anti-HER2 (ErbB2) therapy in preclinical models of breast cancer. Clin Cancer Res 2009; 15: 4712-21.
27. McKinley ET, Smith RA, Tanksley JP, et al. [18F]FLT-PET to predict pharmacodynamic and clinical response to cetuximab therapy in Menetrier's disease. Ann Nucl Med; 26: 757-63.
28. Chen W, Cloughesy T, Kamdar N, et al. Imaging proliferation in brain tumors with F-18-FLT PET: Comparison with F-18-FDG. Journal of Nuclear Medicine 2005; 46: 945-52.
29. Choi SJ, Kim JS, Kim JH, et al. [F-18]3 '-deoxy-3 '-fluorothymidine PET for the diagnosis and grading of brain tumors. European Journal of Nuclear Medicine and Molecular Imaging 2005; 32: 653-9.
30. Cobben DCP, Elsinga PH, van Waarde A, Jager PL. Correspondence re: H. Barthel et al., 3 '-deoxy-3 '-[F-18]fluorothymidine as a new marker for monitoring tumor response to antiproliferative therapy in vivo with positron emission tomography. Cancer Res., 63: 3791-3798,2003. Cancer Research 2003; 63: 8558-9.

31. Grierson JR, Schwartz JL, Muzi M, Jordan R, Krohn KA. Metabolism of 3 '-deoxy-3 '-[F-18]fluorothymidine in proliferating A549 cells: validations for positron emission tomography. Nuclear Medicine and Biology 2004; 31: 829-37.
32. Wagner M, Seitz U, Buck A, et al. 3 '-[F-18]fluoro-3 '-deoxythymidine ([F-18]-FLT) as positron emission tomography tracer for imaging proliferation in a murine B-cell lymphoma model and in the human disease. Cancer Research 2003; 63: 2681-7.
33. Brockenbrough JS, Souquet T, Morihara JK, et al. Tumor 3'-deoxy-3'-(18) F-fluorothymidine ((18)F-FLT) uptake by PET correlates with thymidine kinase 1 expression: static and kinetic analysis of (18)F-FLT PET studies in lung tumors. J Nucl Med; 52: 1181-8.
34. Olive M, Untawale S, Coffey RJ, et al. Characterization of the DiFi rectal carcinoma cell line derived from a familial adenomatous polyposis patient. In Vitro Cell Dev Biol 1993; 29A: 239-48.
35. Waldman T, Kinzler KW, Vogelstein B. p21 is necessary for the p53-mediated G1 arrest in human cancer cells. Cancer Res 1995; 55: 5187-90.
36. Bunz F, Dutriaux A, Lengauer C, et al. Requirement for p53 and p21 to sustain G2 arrest after DNA damage. Science 1998; 282: 1497-501.
37. Dy DY, Whitehead RH, Morris DL. SMS 201.995 inhibits in vitro and in vivo growth of human colon cancer. Cancer Res 1992; 52: 917-23.
38. Muzi M, Mankoff DA, Grierson JR, Wells JM, Vesselle H, Krohn KA. Kinetic modeling of 3'-deoxy-3'-fluorothymidine in somatic tumors: mathematical studies. J Nucl Med 2005; 46: 371-80.
39. Muzic RF, Jr., Cornelius S. COMKAT: compartment model kinetic analysis tool. J Nucl Med 2001; 42: 636-45.
40. Li W, Araya M, Elliott M, et al. Monitoring cellular accumulation of 3'-deoxy-3'-fluorothymidine (FLT) and its monophosphate metabolite (FLT-MP) by LC-MS/MS as a measure of cell proliferation in vitro. J Chromatogr B Analyt Technol Biomed Life Sci; 879: 2963-70.
41. Efron B, Tibshirani R. An Introduction to the Bootstrap. Washington, D.C.: CRC Press; 1993.
42. Zhang CC, Yan Z, Li W, et al. [18F]FLT-PET imaging does not always "light up" proliferating tumor cells. Clin Cancer Res.
43. Kim SJ, Lee JS, Im KC, et al. Kinetic modeling of 3'-deoxy-3'-18F-fluorothymidine for quantitative cell proliferation imaging in subcutaneous tumor models in mice. J Nucl Med 2008; 49: 2057-66.
44. Wang H, Zhang J, Tian J, et al. Using dual-tracer PET to predict the biologic behavior of human colorectal cancer. J Nucl Med 2009; 50: 1857-64.
45. Krieger-Hinck N, Gustke H, Valentiner U, et al. Visualisation of neuroblastoma growth in a Scid mouse model using [18F]FDG and [18F] FLT-PET. Anticancer Res 2006; 26: 3467-72.
46. Buck AK, Bommer M, Stilgenbauer S, et al. Molecular imaging of proliferation in malignant lymphoma. Cancer Res 2006; 66: 11055-61.

47. Yap CS, Czernin J, Fishbein MC, et al. Evaluation of thoracic tumors with 18F-fluorothymidine and 18F-fluorodeoxyglucose-positron emission tomography. Chest 2006; 129: 393-401.
48. Dittmann H, Dohmen BM, Paulsen F, et al. [18F]FLT PET for diagnosis and staging of thoracic tumours. Eur J Nucl Med Mol Imaging 2003; 30: 1407-12.
49. van Westreenen HL, Cobben DC, Jager PL, et al. Comparison of 18F-FLT PET and 18F-FDG PET in esophageal cancer. J Nucl Med 2005; 46: 400-4.
50. Buck AK, Schirrmeister H, Hetzel M, et al. 3-deoxy-3-[(18)F] fluorothymidine-positron emission tomography for noninvasive assessment of proliferation in pulmonary nodules. Cancer Res 2002; 62: 3331-4.
51. Yamamoto Y, Nishiyama Y, Ishikawa S, et al. Correlation of 18F-FLT and 18F-FDG uptake on PET with Ki-67 immunohistochemistry in non-small cell lung cancer. Eur J Nucl Med Mol Imaging 2007; 34: 1610-6.
52. Kenny LM, Vigushin DM, Al-Nahhas A, et al. Quantification of cellular proliferation in tumor and normal tissues of patients with breast cancer by [18F]fluorothymidine-positron emission tomography imaging: evaluation of analytical methods. Cancer Res 2005; 65: 10104-12.
53. Smyczek-Gargya B, Fersis N, Dittmann H, et al. PET with [18F] fluorothymidine for imaging of primary breast cancer: a pilot study. Eur J Nucl Med Mol Imaging 2004; 31: 720-4.
54. Yamamoto Y, Kameyama R, Izuishi K, et al. Detection of colorectal cancer using (1)F-FLT PET: comparison with (1)F-FDG PET. Nucl Med Commun 2009; 30: 841-5.
55. Francis DL, Freeman A, Visvikis D, et al. In vivo imaging of cellular proliferation in colorectal cancer using positron emission tomography. Gut 2003; 52: 1602-6.
56. McKinley ET, Smith RA, Tanksley JP, et al. [(18)F]FLT-PET to predict pharmacodynamic and clinical response to cetuximab therapy in Menetrier's disease. Ann Nucl Med.
57. Moroz MA, Kochetkov T, Cai S, et al. Imaging colon cancer response following treatment with AZD1152: a preclinical analysis of [18F]fluoro-2-deoxyglucose and 3'-deoxy-3'-[18F]fluorothymidine imaging. Clin Cancer Res; 17: 1099-110.
58. Greenman C, Stephens P, Smith R, et al. Patterns of somatic mutation in human cancer genomes. Nature 2007; 446: 153-8.
59. Davies H, Bignell GR, Cox C, et al. Mutations of the BRAF gene in human cancer. Nature 2002; 417: 949-54.
60. Satyamoorthy K, Li G, Gerrero MR, et al. Constitutive mitogen-activated protein kinase activation in melanoma is mediated by both BRAF mutations and autocrine growth factor stimulation. Cancer Res 2003; 63: 756-9.

61. Yokota T, Ura T, Shibata N, et al. BRAF mutation is a powerful prognostic factor in advanced and recurrent colorectal cancer. Br J Cancer; 104: 856-62.
62. Houben R, Becker JC, Kappel A, et al. Constitutive activation of the Ras-Raf signaling pathway in metastatic melanoma is associated with poor prognosis. J Carcinog 2004; 3: 6.
63. Sharma A, Trivedi NR, Zimmerman MA, Tuveson DA, Smith CD, Robertson GP. Mutant V599EB-Raf regulates growth and vascular development of malignant melanoma tumors. Cancer Res 2005; 65: 2412-21.
64. Brose MS, Volpe P, Feldman M, et al. BRAF and RAS mutations in human lung cancer and melanoma. Cancer Res 2002; 62: 6997-7000.
65. Xu X, Quiros RM, Gattuso P, Ain KB, Prinz RA. High prevalence of BRAF gene mutation in papillary thyroid carcinomas and thyroid tumor cell lines. Cancer Res 2003; 63: 4561-7.
66. Lubomierski N, Plotz G, Wormek M, et al. BRAF mutations in colorectal carcinoma suggest two entities of microsatellite-unstable tumors. Cancer 2005; 104: 952-61.
67. Bollag G, Hirth P, Tsai J, et al. Clinical efficacy of a RAF inhibitor needs broad target blockade in BRAF-mutant melanoma. Nature; 467: 596-9.
68. Tsai J, Lee JT, Wang W, et al. Discovery of a selective inhibitor of oncogenic B-Raf kinase with potent antimelanoma activity. Proc Natl Acad Sci U S A 2008; 105: 3041-6.
69. Chang F, Steelman LS, Shelton JG, et al. Regulation of cell cycle progression and apoptosis by the Ras/Raf/MEK/ERK pathway (Review). Int J Oncol 2003; 22: 469-80.
70. Chang F, Steelman LS, Lee JT, et al. Signal transduction mediated by the Ras/Raf/MEK/ERK pathway from cytokine receptors to transcription factors: potential targeting for therapeutic intervention. Leukemia 2003; 17: 1263-93.
71. Solit DB, Rosen N. Resistance to BRAF inhibition in melanomas. N Engl J Med; 364: 772-4.
72. Kopetz S, Desai J, Chan E, et al. PLX4032 in metastatic colorectal cancer patients with mutant BRAF tumors. J Clin Oncol 2010; 28: abstr 3534.
73. Corcoran RB, Ebi H, Turke AB, et al. EGFR-mediated re-activation of MAPK signaling contributes to insensitivity of BRAF mutant colorectal cancers to RAF inhibition with vemurafenib. Cancer Discov; 2: 227-35.
74. Strobel K, Skalsky J, Steinert HC, et al. S-100B and FDG-PET/CT in therapy response assessment of melanoma patients. Dermatology 2007; 215: 192-201.
75. Buck JR, Saleh S, Imam Uddin M, Manning HC. Rapid, microwave-assisted organic synthesis of selective V600EBRAF inhibitors for preclinical cancer research. Tetrahedron Letters; 53: 4161-5.
76. McKinley ET. First Person To Read This and Contact Me Gets a 6-Pack of Beer. J Will Anyone Read This 2013; 1: 1.

77. Oh SJ, Mosdzianowski C, Chi DY, et al. Fully automated synthesis system of 3'-deoxy-3'-[18F]fluorothymidine. Nucl Med Biol 2004; 31: 803-9.
78. Ayers GD, McKinley ET, Zhao P, et al. Volume of preclinical xenograft tumors is more accurately assessed by ultrasound imaging than manual caliper measurements. J Ultrasound Med; 29: 891-901.
79. McKinley ET, Bugaj JE, Zhao P, et al. 18FDG-PET predicts pharmacodynamic response to OSI-906, a dual IGF-1R/IR inhibitor, in preclinical mouse models of lung cancer. Clin Cancer Res; 17: 3332-40.
80. Reyzer ML, Chaurand P, Angel PM, Caprioli RM. Direct molecular analysis of whole-body animal tissue sections by MALDI imaging mass spectrometry. Methods Mol Biol; 656: 285-301.
81. Manier ML, Reyzer ML, Goh A, et al. Reagent precoated targets for rapid in-tissue derivatization of the anti-tuberculosis drug isoniazid followed by MALDI imaging mass spectrometry. J Am Soc Mass Spectrom; 22: 1409-19.
82. Wahl RL, Jacene H, Kasamon Y, Lodge MA. From RECIST to PERCIST: Evolving Considerations for PET response criteria in solid tumors. J Nucl Med 2009; 50 Suppl 1: 122S-50S.
83. Flaherty KT, Puzanov I, Kim KB, et al. Inhibition of mutated, activated BRAF in metastatic melanoma. N Engl J Med; 363: 809-19.
84. Shields AF. PET imaging with 18F-FLT and thymidine analogs: promise and pitfalls. J Nucl Med 2003; 44: 1432-4.
85. Mier W, Haberkorn U, Eisenhut M. [18F]FLT; portrait of a proliferation marker. Eur J Nucl Med Mol Imaging 2002; 29: 165-9.
86. Rasey JS, Grierson JR, Wiens LW, Kolb PD, Schwartz JL. Validation of FLT uptake as a measure of thymidine kinase-1 activity in A549 carcinoma cells. J Nucl Med 2002; 43: 1210-7.
87. Stevaux O, Dyson NJ. A revised picture of the E2F transcriptional network and RB function. Curr Opin Cell Biol 2002; 14: 684-91.
88. Solit DB, Santos E, Pratilas CA, et al. 3'-deoxy-3'-[18F]fluorothymidine positron emission tomography is a sensitive method for imaging the response of BRAF-dependent tumors to MEK inhibition. Cancer Res 2007; 67: 11463-9.
89. Vogel CL, Cobleigh MA, Tripathy D, et al. Efficacy and safety of trastuzumab as a single agent in first-line treatment of HER2-overexpressing metastatic breast cancer. J Clin Oncol 2002; 20: 719-26.
90. Talpaz M, Silver RT, Druker BJ, et al. Imatinib induces durable hematologic and cytogenetic responses in patients with accelerated phase chronic myeloid leukemia: results of a phase 2 study. Blood 2002; 99: 1928-37.
91. McKinley ET, Smith RA, Zhao P, et al. 3'-Deoxy-3'-18F-Fluorothymidine PET Predicts Response to V600EBRAF-Targeted Therapy in Preclinical Models of Colorectal Cancer. J Nucl Med; 54: 424-30.
92. Soloviev D, Lewis D, Honess D, Aboagye E. [(18)F]FLT: an imaging biomarker of tumour proliferation for assessment of tumour response to treatment. Eur J Cancer; 48: 416-24.

93. McKinley ET, Ayers GD, Smith RA, et al. Limits of [18F]-FLT PET as a Biomarker of Proliferation in Oncology. PLoS One 2013; 8.
94. Ogris E, Rotheneder H, Mudrak I, Pichler A, Wintersberger E. A binding site for transcription factor E2F is a target for trans activation of murine thymidine kinase by polyomavirus large T antigen and plays an important role in growth regulation of the gene. J Virol 1993; 67: 1765-71.
95. Liang J, Zubovitz J, Petrocelli T, et al. PKB/Akt phosphorylates p27, impairs nuclear import of p27 and opposes p27-mediated G1 arrest. Nat Med 2002; 8: 1153-60.
96. Pause A, Belsham GJ, Gingras AC, et al. Insulin-dependent stimulation of protein synthesis by phosphorylation of a regulator of 5'-cap function. Nature 1994; 371: 762-7.
97. Kim DH, Sarbassov DD, Ali SM, et al. mTOR interacts with raptor to form a nutrient-sensitive complex that signals to the cell growth machinery. Cell 2002; 110: 163-75.
98. Bermudez O, Marchetti S, Pages G, Gimond C. Post-translational regulation of the ERK phosphatase DUSP6/MKP3 by the mTOR pathway. Oncogene 2008; 27: 3685-91.
99. Feldman ME, Apsel B, Uotila A, et al. Active-site inhibitors of mTOR target rapamycin-resistant outputs of mTORC1 and mTORC2. PLoS Biol 2009; 7: e38.
100. Mao M, Tian F, Mariadason JM, et al. Resistance to BRAF Inhibition in BRAF-Mutant Colon Cancer Can Be Overcome with PI3K Inhibition or Demethylating Agents. Clin Cancer Res; 19: 657-67.
101. Villanueva J, Vultur A, Lee JT, et al. Acquired resistance to BRAF inhibitors mediated by a RAF kinase switch in melanoma can be overcome by cotargeting MEK and IGF-1R/PI3K. Cancer Cell; 18: 683-95.
102. Villanueva J, Vultur A, Herlyn M. Resistance to BRAF Inhibitors: Unraveling Mechanisms and Future Treatment Options. Cancer Res; 71: 7137-40.
103. Maira SM, Stauffer F, Brueggen J, et al. Identification and characterization of NVP-BEZ235, a new orally available dual phosphatidylinositol 3-kinase/ mammalian target of rapamycin inhibitor with potent in vivo antitumor activity. Mol Cancer Ther 2008; 7: 1851-63.
104. Katz SI, Zhou L, Ferrara TA, et al. FLT-PET may not be a reliable indicator of therapeutic response in p53-null malignancy. Int J Oncol; 39: 91-100.
105. Nazarian R, Shi H, Wang Q, et al. Melanomas acquire resistance to B-RAF(V600E) inhibition by RTK or N-RAS upregulation. Nature; 468: 973-7.
106. Wagle N, Emery C, Berger MF, et al. Dissecting therapeutic resistance to RAF inhibition in melanoma by tumor genomic profiling. J Clin Oncol; 29: 3085-96.
107. Schefe JH, Lehmann KE, Buschmann IR, Unger T, Funke-Kaiser H. Quantitative real-time RT-PCR data analysis: current concepts and the novel "gene expression's CT difference" formula. J Mol Med 2006; 84: 901-10.

108. Chen W, Delaloye S, Silverman DH, et al. Predicting treatment response of malignant gliomas to bevacizumab and irinotecan by imaging proliferation with [18F] fluorothymidine positron emission tomography: a pilot study. J Clin Oncol 2007; 25: 4714-21.
109. Zhu Z. Targeted cancer therapies based on antibodies directed against epidermal growth factor receptor: status and perspectives. Acta Pharmacol Sin 2007; 28: 1476-93.
110. Cappuzzo F, Ciuleanu T, Stelmakh L, et al. Erlotinib as maintenance treatment in advanced non-small-cell lung cancer: a multicentre, randomised, placebo-controlled phase 3 study. Lancet Oncol; 11: 521-9.
111. Rothenberg ML, LaFleur B, Levy DE, et al. Randomized phase II trial of the clinical and biological effects of two dose levels of gefitinib in patients with recurrent colorectal adenocarcinoma. J Clin Oncol 2005; 23: 9265-74.
112. Saltz LB, Meropol NJ, Loehrer PJ, Sr., Needle MN, Kopit J, Mayer RJ. Phase II trial of cetuximab in patients with refractory colorectal cancer that expresses the epidermal growth factor receptor. J Clin Oncol 2004; 22: 1201-8.
113. Lenz HJ, Van Cutsem E, Khambata-Ford S, et al. Multicenter phase II and translational study of cetuximab in metastatic colorectal carcinoma refractory to irinotecan, oxaliplatin, and fluoropyrimidines. J Clin Oncol 2006; 24: 4914-21.
114. Khambata-Ford S, Garrett CR, Meropol NJ, et al. Expression of epiregulin and amphiregulin and K-ras mutation status predict disease control in metastatic colorectal cancer patients treated with cetuximab. J Clin Oncol 2007; 25: 3230-7.
115. Dias-Santagata D, Akhavanfard S, David SS, et al. Rapid targeted mutational analysis of human tumours: a clinical platform to guide personalized cancer medicine. EMBO Mol Med; 2: 146-58.
116. Su Z, Dias-Santagata D, Duke M, et al. A platform for rapid detection of multiple oncogenic mutations with relevance to targeted therapy in non-small-cell lung cancer. J Mol Diagn; 13: 74-84.
117. Lovly CM, Dahlman KB, Fohn LE, et al. Routine multiplex mutational profiling of melanomas enables enrollment in genotype-driven therapeutic trials. PLoS One; 7: e35309.
118. O'Neil BH, Allen R, Spigel DR, et al. High incidence of cetuximab-related infusion reactions in Tennessee and North Carolina and the association with atopic history. J Clin Oncol 2007; 25: 3644-8.
119. Patel DD, Goldberg RM. Cetuximab-associated infusion reactions: pathology and management. Oncology (Williston Park) 2006; 20: 1373-82; discussion 82, 92-4, 97.
120. Agool A, Slart RH, Thorp KK, et al. Effect of radiotherapy and chemotherapy on bone marrow activity: a 18F-FLT-PET study. Nucl Med Commun; 32: 17-22.
121. Wieder HA, Geinitz H, Rosenberg R, et al. PET imaging with [18F]3'-deoxy-3'-fluorothymidine for prediction of response to neoadjuvant

treatment in patients with rectal cancer. Eur J Nucl Med Mol Imaging 2007; 34: 878-83.
122. Dehdashti F, Grigsby PW, Myerson RJ, Nalbantoglu I, Ma C, Siegel BA. Positron Emission Tomography with [(18)F]-3'-Deoxy-3'fluorothymidine (FLT) as a Predictor of Outcome in Patients with Locally Advanced Resectable Rectal Cancer: a Pilot Study. Mol Imaging Biol; 15: 106-13.